CHALMERS

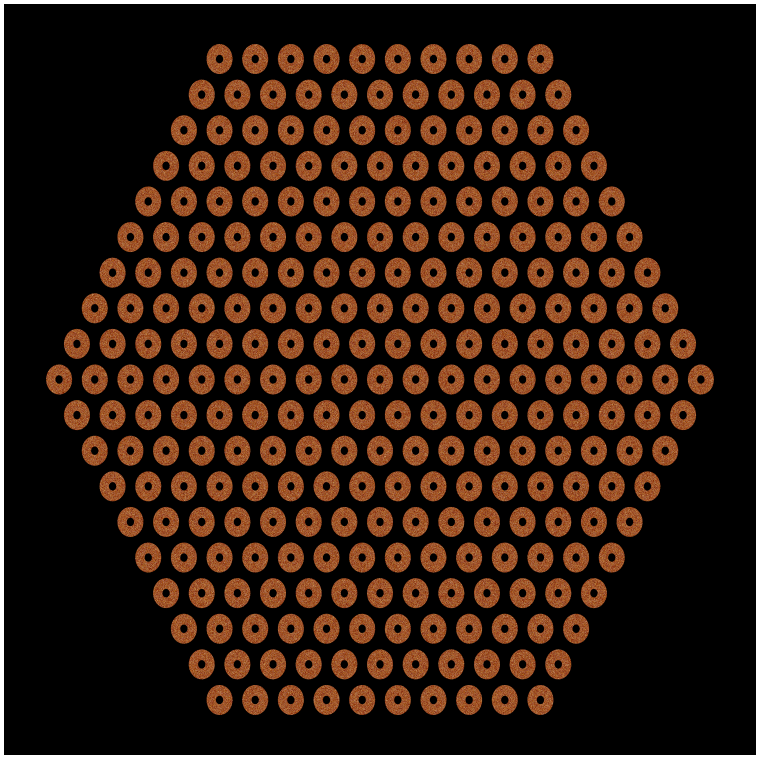

Study of the Effect of Impurities from Nuclear Fuel Reprocessing on the Neutronics of a Fast-Spectrum Generation IV Nuclear Reactor

HAZEL NDULUE

Master's Thesis in Innovative and Sustainable Chemical Engineering

DEPARTMENT OF PHYSICS

CHALMERS UNIVERSITY OF TECHNOLOGY
Gothenburg, Sweden 2026
www.chalmers.se

Master's Thesis 2026

Study of the Effect of Impurities on the Neutronics of a Fast-Spectrum Generation IV Nuclear Reactor

Hazel Ndulue

Computational Nuclear Reactor Physics Group (DREAM)
Division of Subatomic, High Energy and Plasma Physics
Department of Physics
Chalmers University of Technology

Nuclear Chemistry / Industrial Materials Recycling
Division of Energy and Materials
Department of Chemistry and Chemical Engineering
Chalmers University of Technology

CHALMERS

Study of the Effect of Impurities from Nuclear Fuel Reprocessing on the Neutronics of a Fast-Spectrum Generation IV Nuclear Reactor
Hazel Ndulue

Supervisor: Christophe Demazière, Department of Physics
Co-Supervisor : Christian Ekberg, Department of Chemistry and Chemical Engineering
Examiner: Christophe Demazière, Department of Physics

Master's Thesis 2026 Department of Physics
Division of Subatomic, High Energy and Plasma Physics
Computational Nuclear Reactor Physics Group (DREAM)
Chalmers University of Technology
SE-412 96 Gothenburg
Telephone +46 31 772 1000

Cover: Two-dimensional hexagonal lattice configuration of the SPX fast reactor fuel assembly at initial burnup, showing the geometric arrangement of fuel pins within the Monte Carlo computational mesh implemented in Serpent.
Typeset in LaTeX
Printed by Chalmers Reproservice
Gothenburg, Sweden 2026

Abstract

Green, sustainable, and clean are ubiquitous terms in modern energy discourse, yet their meaningful realization remains a profound challenge. Throughout history, electrification has been a catalyst for human progress—symbolizing not only access to dignity but also the foundation for economic and intellectual growth. While renewable energy sources dominate global decarbonization strategies, nuclear power currently offers the most reliable and scalable pathway to large-scale emissions reduction. However, its full sustainability is constrained by persistent concerns across the nuclear fuel cycle, particularly the long-term radiotoxicity and heat generation of spent nuclear fuel. Closing the fuel cycle is therefore central to aligning nuclear energy with the United Nations Sustainable Development Goal 7—"ensure access to affordable, reliable, sustainable, and modern energy for all"—by addressing both resource conservation and intergenerational equity.

This master's thesis investigates one crucial dimension of that challenge: the impact of reprocessing-induced impurities on the neutronic behavior of sodium-cooled fast reactor fuel assemblies, with a focus on the SPX Superphénix reference design. Building on the CHALMEX separation process and the internal gelation route for fuel fabrication, the work examines how residual actinides, fission products, and trace elements carried over from reprocessing alter the final fuel composition and performance. A literature review is combined with microscopic cross-section analysis of selected impurities using the OECD/NEA JANIS database. Lattice depletion and branch calculations are then performed with the Monte Carlo code Serpent 2 on SPX-type assemblies, with and without impurities, to quantify their effects on reactivity coefficients, neutron flux distributions, absorption behavior, and burnup characteristics.

By identifying tolerance thresholds and impurity-driven deviations in key neutronic parameters, this thesis assesses the operational viability of reprocessed fuels and proposes directions for optimizing separation and fabrication processes. The results support the safe, efficient, and genuinely sustainable deployment of Generation-IV fast reactors within a closed fuel cycle framework, contributing evidence-based insights for future reactor development and fuel cycle strategies.

For freedom,
in all its forms.

Acknowledgements

To my parents, who made this journey possible from the very beginning by giving me life, and who have always spoken beauty, strength, and purpose into it. Their relentless ambition to give me the best, and the values they instilled in me, shaped the foundation upon which this work stands.

To my brothers, Ark and Millenium, my backbone. Thank you for believing in me through every phase of growth. You have witnessed every version of me, and understood who I was becoming even before I did.

To my supervisor, Christophe, for the opportunity to undertake such a thoughtfully tailored project — one that challenged me deeply and allowed me to grow both scientifically and personally.

To the remarkable people I met along this journey in the Department of Subatomic Physics, whose presence made this experience intellectually and humanly enriching.

To the Department of Nuclear Chemistry, and especially Esraa, for her continuous support, attention, and for the beautiful scientific dialogues I had the privilege to share with her and with Letizia.

To Antonio, for the meaningful conversations that moved seamlessly from nuclear reactor physics to friendship.

To Professor Andrea d'Anna, my guide and mentor, who has been present since the very beginning of my engineering journey. Your guidance, vision, and trust have accompanied me far beyond this thesis.

To my friends who cherish me, thank you for your presence, strength, and joy.

Contents

List of Acronyms

Below is the list of acronyms used throughout this thesis, listed in alphabetical order.

ACSEPT Actinide Recycling by Separation and Transmutation (EU project)
AHA Acetohydroxamic Acid
Am Americium
ATLANTE CEA hot-test facility used for GANEX demonstration
BTBP Bis-Triazinyl-Bipyridine
BTBPs Bis-Triazinyl-Bipyridines
BTP Bis-Triazinyl-Pyridine
BOL Beginning of Life (start of irradiation)
CDTA trans-1,2-Cyclohexanediaminetetraacetic Acid
CEA Commissariat à l'énergie atomique et aux énergies alternatives (France)
CHALMEX Chalmers Grouped Actinide Extraction Process
CHON Carbon, Hydrogen, Oxygen, Nitrogen (extractant-design principle)
Cm Curium
COEX Co-extraction variant of PUREX (France)
CRAM Chebyshev Rational Approximation Method (depletion solver)
$CyMe_4$-BTBP 6,6'-Bis(5,5,8,8-tetramethyl-5,6,7,8-tetrahydro-benzo[1,2,4]triazin-3-yl)-[2,2']-bipyridine
DGR Deep Geological Repository
DEHiBA N,N-di(2-ethylhexyl)isobutyramide
DF Decontamination Factor
DIAMEX DIAMide Extraction (co-extraction of An(III)/Ln(III))
DMDBTDMA N,N'-Dimethyl-N,N'-Dibutyltetradecylmalonamide
DMDOHEMA N,N-Dimethyl-N,N-Dioctyl-2-(2-hexyloxyethyl)malonamide
EOL End of Life (end of irradiation)
EPR European Pressurised Reactor
EURO-GANEX European GANEX variant for grouped TRU extraction
FP Fission Products
FS-13 Phenyl Trifluoromethyl Sulfone (fluorinated diluent)
FCC Fully Closed Fuel Cycle (multi-recycling in fast reactors)
GANEX Grouped Actinide Extraction
Gen-IV Generation IV nuclear reactor systems
GWd/tHM Gigawatt days per tonne of heavy metal
HAC High Active Concentrate
HAR High Active Raffinate
HDI Human Development Index
HDEHP Di(2-ethylhexyl)phosphoric Acid
HFP Hot Full Power
HM Heavy Metal

HMTA Hexamethylenetetramine
HZP Hot Zero Power
ICP-MS Inductively Coupled Plasma Mass Spectrometry
i-SANEX Innovative SANEX Process
JANIS Java-based Nuclear Information Software
LWR Light Water Reactor
Ln(III) Trivalent Lanthanide
MA Minor Actinide
MATLAB Computing platform for post-processing
MOX Mixed Oxide Fuel
NIMBY "Not In My Backyard" siting effect
Np Neptunium
OTC Open / once-through fuel cycle
P&T Partitioning and Transmutation
pcm Per cent mille (10^{-5} change in k)
PUREX Plutonium Uranium Redox EXtraction
PWR Pressurised Water Reactor
SANEX Selective ActiNide EXtraction
SDG Sustainable Development Goals
SDG 7 SDG on Affordable and Clean Energy
Serpent 2 Monte Carlo reactor physics and depletion code
SFR Sodium-cooled Fast Reactor
SNF Spent Nuclear Fuel
SO_3-Ph-BTP Water-soluble Bis-Triazinyl-Pyridine for An(III) separation
SPX Superphénix sodium-cooled fast reactor
TBP Tri-*n*-Butyl Phosphate
TEDGA Tetraethyl Diglycolamide
TODGA Tetra-*n*-octyl Diglycolamide
TPH Hydrogenated Tetrapropylene (aliphatic diluent)
TRL Technology Readiness Level
TRU Transuranic Elements (Np, Pu, Am, Cm)
U Uranium
UO_2 Uranium Dioxide Fuel
UOX Uranium Oxide Fuel (standard LWR fuel)
UREX Uranium EXtraction process (Pu-avoidance PUREX variant)
Zr Zirconium

Nomenclature

Parameters and Variables

k Neutron multiplication factor between subsequent neutron generations
k_∞ Infinite neutron multiplication factor (lattice k_∞)
k_{eff} Effective neutron multiplication factor of the finite system
η Reproduction factor (neutrons produced per thermal absorption in fuel)
f Thermal utilization factor (fraction of absorptions in fuel)
p Resonance escape probability
ε Fast fission factor
P_{FNL} Fast non-leakage probability (six-factor formula)
P_{TNL} Thermal non-leakage probability (six-factor formula)
ρ Reactivity, usually expressed in pcm
$\Delta\rho$ Change in reactivity between two states
Δk Change in multiplication factor between two states
B Burnup (continuous variable)
BU Tabulated burnup value (MWd/kgU or MWd/kgHM)
T Characteristic fuel temperature used in transport model
T_{fuel} Fuel temperature (K)
T_{cool} Coolant temperature (K)
ρ_{cool} Coolant density
v Coolant void fraction
x Coolant void fraction used in void-coefficient definition
V_{void} Volume of voided coolant region
V_{coolant} Reference coolant volume (unvoided)
E Neutron energy (eV)
Σ_t Macroscopic total cross section (cm^{-1})
Σ_c Macroscopic capture cross section (cm^{-1})
Σ_f Macroscopic fission cross section (cm^{-1})
σ_t Microscopic total cross section (barn)
σ_c Microscopic capture cross section (barn)
σ_f Microscopic fission cross section (barn)
Σ_x^{U} Macroscopic cross section of uranium isotopes for reaction type x (total, capture, fission)
Σ_x^{Pu} Macroscopic cross section of plutonium isotopes for reaction type x
Σ_x^{MA} Macroscopic cross section of minor actinide isotopes for reaction type x
Σ_x^{FP} Macroscopic cross section of fission-product isotopes for reaction type x
$\Sigma_r(E)$ Energy-dependent macroscopic cross section for reaction r
$\Sigma_r^{\text{group}}(E)$ Grouped macroscopic cross section for reaction r (e.g. U, Pu, MA, FP)
$\langle\Sigma_r^{\text{group}}\rangle$ Energy-averaged macroscopic cross section over a given energy range
N_i Atomic number density of isotope i (atoms/cm^3)

$\mathbf{N}(t)$ Vector of nuclide number densities as a function of time
$\mathbf{A}$ Depletion matrix containing decay constants and reaction-rate coefficients
α_D Fuel Doppler reactivity coefficient (pcm/K)
D_C Doppler coefficient defined as $\Delta\rho/\Delta T$
α_{cool} Coolant temperature reactivity coefficient (pcm/K)
α_v Void reactivity coefficient (pcm per unit void fraction)
D Distribution ratio in solvent extraction ($D = C_{\text{org}}/C_{\text{aq}}$)

Units and Technical Terms

General reactor physics, energy and fuel-cycle context

---

barn Unit of microscopic cross section, 1 barn = $10^{-24}\,\text{cm}^2$
eV Electronvolt, unit of neutron energy
kWh Kilowatt-hour, unit of electrical energy consumption
MWd/kgU Megawatt days per kilogram of uranium
MWd/kgHM Megawatt days per kilogram of heavy metal
GWd/tHM Gigawatt days per tonne of heavy metal

Dry (pyrochemical) reprocessing and recycling strategies

Pyroprocessing Generic term for high-temperature / molten-salt electrochemical reprocessing
Molten-salt electrorefining Pyrochemical technique for separating actinides in molten salt
Homogeneous recycling Strategy where all recovered TRU (U, Pu, MAs) are uniformly mixed into one fuel type
Heterogeneous recycling Strategy where minor actinides are confined to dedicated pins / targets within the core

---

Internal gelation sol–gel and fuel fabrication

Sol–gel Wet-chemical route to produce gel microspheres from actinide nitrate solutions
Internal gelation Sol–gel variant where gelation chemistry occurs within each droplet
ADUN Acid-deficient uranyl nitrate solution used as precursor for internal gelation
Urea Stabiliser and complexant in internal gelation feed solution
Sphere-pac Fuel concept based on packed microspheres rather than pellets

---

Codes, libraries and modelling tools

`dep.m` Serpent depletion output file containing isotopic inventories
`res.m` Serpent results file containing integral neutronic quantities (e.g. k_{eff})
`.coe` Serpent branch-calculation output files with reactivity coefficients
`wrk` Serpent working files containing isotopic compositions for branch calculations

Chapter 1

Introduction

1.1 Background and Motivation

> "The world is very different now. For man holds in his mortal hands the power to abolish all forms of human poverty and all forms of human life."
> — President John F. Kennedy, *Inaugural Address*, 1961 [1].

Energy is the lifeblood of civilization. It defines the pace of human progress, underpins economic growth, and determines the quality of life across nations. As President Kennedy foresaw, humanity possesses both the power to transform and to destroy—and energy lies at the heart of this duality.

Access to electricity represents far more than technological advancement; it is a foundation for human dignity, development, and peace. Quantitative analysis have demonstrated this connection by correlating the United Nations Human Development Index (HDI) with per-capita electricity consumption for sixty countries representing ninety percent of the world's population [2]. His analysis showed that human well-being rises sharply with electricity use before stabilizing at around 4 000 kWh per person per year—the threshold at which electricity becomes sufficient to sustain high living standards. Importantly, the correlation between HDI and electricity use proved stronger than that with total primary energy, emphasizing that electricity is the most direct enabler of social and economic progress [2].

Profound inequities in global energy distribution further exacerbate disparities in human development. In the early 1990s, three-quarters of the world's population consumed only 30% of commercial energy, while the remaining quarter—residing in industrialized nations—used 70% [3],[2]. This imbalance perpetuates poverty, illiteracy, and political instability, as billions of people still lacked access to electricity. For developing nations, true progress requires meeting fundamental human needs—employment, health, education, housing, water, and sanitation—all of which depend directly on energy availability [3].

The historical role of energy in liberating humanity from physical constraint has been profound. From fire to steam, electricity, and eventually nuclear power, each energy revolution expanded the frontiers of knowledge, culture, and social evolution. Yet the challenge today is to sustain this progress without compromising environmental integrity or intergenerational equity.

In this context, nuclear energy emerges as a crucial component of sustainable development. It offers a dense, low-carbon, and reliable power source capable of supporting industrial growth while limiting greenhouse-gas emissions. As the world strives to achieve the United Nations' Sustainable Development Goal 7—"Ensure access to affordable, reliable, sustainable and modern energy for all"—nuclear power's potential contribution cannot be overlooked.

However, realizing this potential requires addressing persistent challenges associated with uranium mining, waste management, public acceptance, and the need to transition toward a closed and sustainable nuclear fuel cycle. The following sections explore these challenges and outline the motivation for the present study.

1.2 Current Status and Challenges of Nuclear Power

The first full-scale commercial nuclear power plant began operation at Calder Hall, Great Britain, on August 27, 1956, with a capacity of 50 MW. Shortly after, in December 1957, the Shippingport reactor in Pennsylvania (United States) started producing 60 MW, followed by France's 40 MW G2 reactor at Marcoule in April 1959 [4]. These developments marked the beginning of the nuclear power era, characterized by optimism and technological ambition [5, 6].

In recent decades, however, the nuclear industry—particularly in the United States and Europe—has experienced a decline due to economic constraints, public opposition, and long construction times. Despite this, many experts predict a renewed interest in nuclear energy driven by multiple global challenges. Several factors contribute to this so-called "nuclear renaissance" [5]:

- **Technological innovation:** The emergence of fourth-generation (Gen-IV) reactors promises enhanced safety, efficiency, and waste minimization.
- **Climate urgency:** Nuclear power is among the lowest carbon-emitting large-scale energy sources, offering a stable complement to intermittent renewables.
- **Energy security:** For many nations, nuclear technology reduces dependence on imported fossil fuels and stabilizes domestic energy production.
- **Sustainability goals:** Nuclear energy aligns with international commitments under the Kyoto Protocol and the Paris Agreement by providing reliable electricity with minimal greenhouse gas emissions.

As Dr. Patrick Moore, a former member of Greenpeace, stated, "Nuclear energy is the only large-scale, cost-effective energy source that can reduce carbon dioxide emissions while continuing to satisfy a growing demand for power" [7]. This statement encapsulates the central argument for nuclear power in the twenty-first century: it offers a viable pathway to decarbonization while maintaining energy security.

1.2.1 Front-End Challenges: Uranium Mining and Resource Use

Despite these advantages, nuclear energy faces significant challenges at both the front and back ends of the fuel cycle. At the front end, the mining and enrichment of uranium remain resource-intensive. Natural uranium consists primarily of ^{238}U (99.3%) and only 0.7% of the fissile isotope ^{235}U. To produce adequate quantities of ^{235}U, large volumes of ore must be mined and processed, resulting in environmental impacts such as land degradation, water consumption, and the accumulation of radioactive tailings [8].

Many uranium-producing nations—for example, Niger, Kazakhstan, and Namibia—do not directly benefit from the technology, raising ethical questions about environmental justice and equitable distribution of benefits. Thus, sustainability in nuclear energy must consider not only technical safety and emissions but also the socio-economic dimensions of the fuel cycle.

1.2.2 Back-End Challenges: Spent Nuclear Fuel and Waste Management

At the back end of the cycle lies one of the most complex and debated issues in nuclear power: the management of spent nuclear fuel (SNF). Once fuel is irradiated, it must be removed from the reactor core and stored in cooling pools for several years to allow for the decay of short-lived isotopes and the dissipation of residual heat.

SNF is among the most radiotoxic materials known, containing long-lived actinides and heat-generating fission products that remain hazardous for hundread of thousands of years [4, 9]. Current management strategies involve interim wet storage followed by dry cask storage, yet these are not permanent solutions. Long-term concepts propose *deep geological repositories* (DGRs), in which spent fuel is encapsulated (for instance, in copper canisters) and buried in stable geological formations [9, 10].

However, DGRs present scientific and societal challenges. These include the long-term stability of containment materials, potential radionuclide migration into groundwater, intergenerational responsibility, and the "Not In My Backyard" (NIMBY) phenomenon, which reflects public reluctance to host such facilities. Furthermore, many repository sites are located in regions that do not directly benefit from nuclear energy production, raising questions of fairness and environmental equity [4].

1.2.3 Open and Closed Fuel Cycles

The challenges described above stem largely from the choice of fuel cycle strategy. In the **open (once-through) fuel cycle**, spent fuel is considered waste after a single use and is stored pending disposal. This approach is technically straightforward but results in inefficient use of uranium resources and the accumulation of long-lived waste [10, 11].

In contrast, the **closed fuel cycle** aims to recover valuable materials—such as uranium, plutonium, and minor actinides—through reprocessing and recycling. By reusing fissile materials in new fuel, the closed cycle can enhance resource utilization and reduce the volume and radiotoxicity of high-level waste. However, the process introduces new challenges related to separation efficiency, impurity carryover, proliferation resistance, and cost.

The closed cycle is the foundation of Generation-IV reactor systems, which are designed to achieve sustainable nuclear power production through recycling and transmutation. Nevertheless, real-world implementation faces the practical limitation that no chemical separation process is 100% effective. As a result, trace impurities from reprocessing—such as lanthanides, platinum group metals, and transition elements—remain in the recycled fuel, potentially affecting its neutronic behavior.

1.3 Overview of Current Technologies

Globally, around half a million tonnes [11] of spent nuclear fuel (SNF) are expected to be in dry or wet storage by 2050. Continued storage without a long-term management strategy is not sustainable, and this SNF must eventually either be disposed of permanently—in what is known as the *open nuclear fuel cycle*—or recycled in the *closed fuel cycle* [11].

The nuclear fuel cycle encompasses all stages from uranium mining and fuel fabrication to reactor operation, spent fuel management, and final disposal or recycling. The choice of fuel cycle strategy fundamentally determines how efficiently nuclear resources are used, how much waste is produced, and how sustainable nuclear power can ultimately become [11].

The **open or once-through cycle (OTC)** refers to the approach where spent uranium oxide (UOX) fuel is stored and eventually disposed of in deep geological repositories without being reprocessed. This is the most straightforward approach, but it results in inefficient use of uranium resources and large accumulations of long-lived radioactive waste [11].

The **partially closed or thermal recycle cycle (TTC)** involves reprocessing spent fuel to recover fissile materials such as uranium and plutonium, which are then recycled as mixed oxide (MOX) fuel. This approach, sometimes referred to as *plutonium mono-recycling*, improves uranium utilization by approximately 15–25% compared to the open cycle and allows the reuse of valuable nuclear materials that would otherwise be discarded [11, 12].

The **fully closed cycle (FCC)** takes this concept further, reprocessing and recycling fissile materials multiple times—typically in fast reactors—to maximize the energy extracted from uranium resources and to minimize the generation of high-level waste. This cycle effectively closes the loop of nuclear fuel use, enabling long-term sustainability of nuclear energy by significantly reducing both waste volumes and the need for fresh uranium mining [10, 11, 13].

The **partitioning and transmutation (P&T)** scenario represents an even more advanced concept, in which minor actinides (MAs) such as neptunium, americium, and curium are separated and transmuted in fast reactors or accelerator-driven systems. This approach is not primarily aimed at energy production but at reducing the heat generation and radiotoxicity of long-lived waste, thereby lowering the long-term environmental burden on geological repositories [11].

Among these strategies, the transition toward a closed or partially closed fuel cycle represents a critical step toward achieving sustainable nuclear power. Reprocessing and recycling enable the recovery of valuable fissile materials, extend uranium resource lifetimes, and reduce the volume and toxicity of nuclear waste that must be isolated from the environment for millennia. However, these approaches also introduce new challenges related to chemical separation efficiency, impurity management, proliferation risk, and cost—all of which must be addressed to realize the promise of a truly sustainable nuclear future [11].

1.3.1 Toward Sustainable Nuclear Energy

The future of nuclear power depends on addressing these front-end and back-end challenges simultaneously. A sustainable nuclear energy system must achieve low environmental impact, high safety standards, economic feasibility, and social acceptance. Central to this vision is the closure of the fuel cycle through advanced reprocessing and recycling technologies, coupled with reactor designs capable of tolerating and efficiently burning recycled fuels.

The present work contributes to this broader objective by examining how impurities originating from reprocessing (specifically from the CHALMEX process) influence the neutronic properties of fast-spectrum Gen-IV fuel. Understanding these effects is essential for assessing the viability and safety of recycled fuels and, ultimately, for realizing a secure and sustainable nuclear future.

1.4 Why Reprocessing Matters

1.4.1 Sustainability, Intergenerational Justice, and the Role of Advanced Reprocessing

As the global population continues to grow, the demand for energy will inevitably increase. Providing clean, reliable, and sustainable energy sources is therefore essential for ensuring future stability and prosperity. In line with the principle of sustainable development—meeting the needs of the present without compromising the ability of future generations to meet their own needs—it becomes necessary to consider the three main pillars of sustainability: environmental, social, and economic.

The concept of *intergenerational justice* is increasingly significant in the context of climate change, where future generations will bear the consequences of our continued dependence on fossil fuels. This principle also applies to nuclear energy, particularly with respect to waste generation and the absence of definitive long-term disposal solutions. Thus, the moral responsibility to minimize the burden imposed on future generations is evident [10, 14, 15].

Putting this principle into practice means that existing reprocessing technologies—which currently allow the recycling of uranium and plutonium—must be further developed and extended. All possible options to recycle long-lived radioactive waste constituents should be thoroughly explored. One of the most promising approaches for achieving this is the *Partitioning and Transmutation (P&T)* strategy, which aims to separate and convert long-lived isotopes into shorter-lived or stable nuclides through neutron irradiation. In this context, *minor actinides (MAs)* such as neptunium, americium, and curium play a central role. Their recycling, however, involves more complex and highly remote fuel cycle operations, including fabrication, irradiation, and transport [10, 16, 17].

The *closed fuel cycle* has been demonstrated to be a key pathway toward achieving these sustainability goals. By closing the fuel cycle, it becomes possible to reduce waste volumes, recover valuable materials such as uranium and plutonium, and, in more advanced cases, recycle minor actinides and even selected fission products. Such strategies not only reduce the long-term radiotoxicity of nuclear waste but also optimize resource utilization and align with the objectives of the United Nations Sustainable Development Goals (SDGs), particularly SDG 7, which calls for access to affordable, reliable, sustainable, and modern energy for all.

Currently, the most widely deployed process for uranium and plutonium recycling is the *PUREX (Plutonium Uranium Redox Extraction)* process. Building upon this, advanced technologies such as *GANEX (Group Actinide Extraction)* have been developed to recover not only uranium and plutonium but also the minor actinides collectively. These innovations represent an important step toward closing the nuclear fuel cycle entirely, minimizing the environmental footprint of nuclear energy, and fulfilling the ethical obligation of ensuring sustainability across generations.

1.4.2 Overview of Reprocessing Concepts and Techniques

Before examining the details of reprocessing technologies, it is essential to introduce key concepts such as homogeneous and heterogeneous recycling as well as the distinction between aqueous and dry (pyrochemical) systems.

Reprocessing can occur through either aqueous or dry methods. In the aqueous route, the technology begins with the dissolution of UO2 in concentrated nitric acid solutions, followed by solvent extraction processes designed to selectively separate metallic species, mainly actinides.

As presently configured, used fuel reprocessing is carried out using the **Plutonium Uranium Redox Extraction (PUREX)** process, which is the only technology currently implemented at an industrial scale [14, 18, 19].

In the PUREX process, uranium (about 95% of the heavy metal content) and plutonium (approximately 1%) are recovered, while fission products and minor actinides are treated as high-level radioactive waste (HLW). These wastes are subsequently immobilized in solid matrices such as glass or ceramic for long-term disposal.

The reprocessing of spent uranium fuels has been studied since the 1950s. The most common approach involves dissolving the irradiated fuel in concentrated nitric acid, followed by solvent–solvent extraction of actinides using an organic extractant such as tributyl phosphate (TBP) [18, 19]. The **PUREX** process, based on this principle, allows the recovery of uranium and plutonium for reuse as **mixed oxide (MOX)** fuel, composed of UO2 and PuO2. MOX fuel is commonly used in thermal reactors, representing a partially closed fuel cycle [15, 18, 19].

However, the separation of pure plutonium introduces a proliferation concern, as it can potentially be diverted for non-peaceful uses. To mitigate this risk, several modified processes have been developed that co-extract uranium and plutonium rather than separating them completely. Examples include the **COEX** process in France, the **Advanced PUREX** process in Japan, and the **UREX** process in the United States [14, 19].

In parallel, more advanced reprocessing technologies such as **GANEX (Group Actinide Extraction)** have been developed to recover uranium, plutonium, and minor actinides together. GANEX represents a significant advancement in achieving a fully closed fuel cycle, enabling collective actinide recovery while reducing proliferation risks [14, 15].

Beyond aqueous methods, **dry (pyrochemical)** reprocessing techniques are also being actively investigated. These involve electrochemical separation of actinides in molten salts and are more compatible with metallic or fast reactor fuels. Pyroprocessing offers advantages such as compact plant designs, higher proliferation resistance, and better suitability for high burnup or fast-spectrum fuels [14].

The separation processes described above play a crucial role in the development of advanced nuclear fuel cycles. Their purpose is to enable the repeated recycling of fissile materials—particularly uranium and plutonium—into new fuels for next-generation reactors, thereby maximizing resource efficiency and minimizing long-term waste [14].

1.4.3 Homogeneous and Heterogeneous Recycling Strategies

Before exploring specific reprocessing techniques, it is useful to distinguish between the **homogeneous** and **heterogeneous** recycling approaches, which determine how transuranic elements are reintroduced into nuclear fuel.

In the **homogeneous recycling** strategy, all recovered transuranic elements—including uranium, plutonium, and minor actinides—are uniformly mixed and fabricated into a single fuel type. This fuel is then reloaded into the reactor core, allowing for continuous recycling of all actinides and the stabilization or reduction of the overall actinide inventory in the system [17]. However, the inclusion of minor actinides makes fuel fabrication and handling significantly more complex due to their intense heat generation and radioactivity, which require remote and shielded operations.

By contrast, the **heterogeneous recycling** approach confines minor actinides to specific fuel pins or target assemblies that are strategically positioned within the reactor core. This method allows for more flexible control of transmutation rates and limits the handling of highly radioactive materials to a smaller fraction of the nuclear infrastructure. It is particularly advantageous when the main objective is to reduce existing minor actinide inventories rather than to achieve continuous recycling [16, 17].

The choice between homogeneous and heterogeneous recycling strategies depends on the goals of the nuclear system [17]. Homogeneous recycling prioritizes resource utilization and self-sufficiency, whereas heterogeneous recycling focuses on waste minimization and operational safety.

Both strategies are being explored within the framework of **Generation IV fast reactors**, which aim to achieve sustainable nuclear power through the multi-recycling of transuranic elements. The successful implementation of either strategy would represent a major step toward a fully closed, low-waste nuclear fuel cycle capable of meeting long-term energy and environmental goals [15, 17].

1.5 The Challenge of Impurities

One of the principal challenges in achieving a truly closed nuclear fuel cycle lies in the presence of impurities that accumulate during fuel reprocessing and recycling [15]. These impurities, originating from incomplete separations in chemical processes such as PUREX or pyroprocessing, include fission products, corrosion-derived elements, and residual minor actinides. Even trace concentrations of these species can influence the physical, chemical, and neutronic properties of the recycled fuel, potentially compromising reactor performance and safety margins.

Recent studies have highlighted that reprocessing-induced impurities—particularly lanthanides, transition metals, and platinum group elements—can act as strong neutron absorbers, thereby reducing reactivity and altering flux spectra in fast-spectrum systems [15, 20]. Furthermore, impurities may affect thermal conductivity, melting behavior, and fuel–cladding chemical interactions, which in turn impact the overall efficiency and reliability of reactor operations [20]. In the context of Generation-IV and fast breeder reactors, these effects become more pronounced due to the tighter neutronic balance and higher operating temperatures typical of such systems [21].

Addressing the impurity challenge requires not only the optimization of chemical separation processes but also an integrated understanding of how impurity elements behave within the fuel matrix under irradiation. For example, elements such as molybdenum, ruthenium, and palladium can form secondary phases or metallic inclusions that modify the local power distribution and thermal behavior of the fuel [21]. Hence, the development of impurity-tolerant fuel forms and advanced separation techniques is essential for realizing sustainable and safe closed fuel cycles.

The present work contributes to this ongoing research effort by investigating how impurities originating from the CHALMEX reprocessing process influence the neutronic characteristics of a fast-spectrum reactor (Superphénix benchmark). By quantifying the neutronic impact of these impurity elements, this study provides insight into the feasibility of impurity-tolerant fuel recycling strategies, thereby supporting the long-term goal of a sustainable nuclear energy system.

1.6 Aim and Scope of the Thesis

This thesis aims to quantify the effect of reprocessing-induced impurities, originating from the CHALMEX aqueous separation process, on the neutronic performance of a sodium-cooled fast reactor benchmark based on the Superphénix (SPX) inner fissile configuration.

The work establishes a reactor-physics modelling framework that links actinide separation chemistry to fast-spectrum core behaviour. Starting from a representative depleted LWR fuel inventory, mixed-oxide (MOX) compositions with varying U/Pu mass ratios are constructed. These compositions are analysed both in their ideal recycled form and with the impurity vectors expected from CHALMEX processing.

Using Serpent 2—a continuous-energy Monte Carlo neutron transport and burnup code developed at VTT Technical Research Centre of Finland [22]—the study evaluates the evolution of the infinite-medium multiplication factor k_∞ over burnup, reactivity feedback coefficients, and neutron flux spectra.

By developing and applying this simulation environment, the thesis provides a quantitative assessment of whether CHALMEX-derived recycled fuel—containing realistic impurity carry-over—remains neutronically feasible within a fast-spectrum Generation IV system. In this way, the work acts as a bridge between CHALMEX aqueous reprocessing research and reactor deployment considerations, enabling chemistry-driven fuel concepts to be evaluated within a consistent neutronic framework.

1.7 Thesis Structure

The thesis is organised to progressively connect nuclear fuel-cycle considerations with detailed neutronic modelling in a fast-spectrum Generation IV reactor framework.

Chapter 1 introduces the broader context of sustainable nuclear energy and the transition from an open to a closed fuel cycle. The motivation for advanced reprocessing technologies is presented, with particular emphasis on reducing long-term radiotoxicity, heat generation and improving resource utilisation. The research objectives and scope of the study are defined, focusing on assessing the neutronic feasibility of CHALMEX-derived recycled fuel in a fast reactor environment.

Chapter 2 provides the scientific and technological background of the work. It reviews conventional aqueous reprocessing (PUREX) and advanced partitioning strategies, culminating in the introduction of the CHALMEX process. The chemical principles of the solvent system, the expected impurity vector, and the associated fuel fabrication assumptions are described. The SPX fast-reactor benchmark configuration adopted as the neutronic reference model is also introduced.

Chapter 3 describes the computational methodology and modelling strategy implemented in Serpent 2. The geometrical representation of the fuel assembly, material compositions, burnup strategy, and branch calculation setup are detailed. The treatment of temperature-dependent cross sections, Doppler broadening, unresolved resonance sampling, and coolant-density variations is specified. The different fuel configurations analysed in this work—reference SPX fuel, MOX fuels with varying plutonium enrichment, TRU-loaded fuels, and impurity-bearing fuel—are defined and justified.

Chapter 4 presents the results and discussion. The analysis begins with validation of the reference SPX configuration and the evaluation of the burnup-dependent multiplication factor. A systematic screening of plutonium enrichment levels is performed to identify a suitable host fuel. The effects of minor actinide loading and CHALMEX-derived impurities on reactivity evolution are quantified. A detailed macroscopic and microscopic cross-section analysis is conducted to physically interpret the observed reactivity trends. Reactivity feedback coefficients—including fuel-temperature (Doppler), coolant temperature, and void reactivity effects—are evaluated and compared between the reference and impurity-loaded configurations.

Chapter 5 summarises the principal findings of the study. The feasibility of implementing CHALMEX-derived recycled fuel in a fast-spectrum reactor is assessed from a neutronic standpoint. The limitations and directions for future research, are outlined.

Chapter 2

Background

2.1 Aqueous reprocessing and advanced partitioning systems

2.1.1 The PUREX Process

The PUREX process (Plutonium Uranium Redox EXtraction), developed in the United States in the late 1940s, remains the foundation of modern aqueous reprocessing technology. It replaced earlier precipitation and solvent-extraction systems such as the bismuth phosphate, Redox, and Butex processes, offering greater chemical efficiency and continuous operation [23].

In the PUREX process, spent oxide fuel is dissolved in concentrated nitric acid, and uranium and plutonium nitrates are selectively extracted into an organic phase containing tri-*n*-butyl phosphate (TBP) diluted in a paraffinic hydrocarbon. The separation is achieved through the extraction of U(VI) and Pu(IV) nitrate complexes followed by the reductive back-extraction of plutonium to the aqueous phase, leaving uranium in the organic phase. The key extraction equilibria are represented as:

$$\mathrm{Pu^{4+}} + 4\mathrm{NO_3^-} + 2\mathrm{TBP} \leftrightarrow \mathrm{Pu(NO_3)_4 \cdot 2TBP} \tag{2.1}$$

$$\mathrm{UO_2^{2+}} + 2\mathrm{NO_3^-} + 2\mathrm{TBP} \leftrightarrow \mathrm{UO_2(NO_3)_2 \cdot 2TBP} \tag{2.2}$$

Following extraction, plutonium is separated from uranium by **reductive stripping**, where tetravalent Pu is reduced to the non-extractable trivalent state using uranous nitrate ($\mathrm{U^{4+}}$) as a reductant:

$$2\mathrm{Pu^{4+}} + \mathrm{U^{4+}} + 2\mathrm{H_2O} \rightarrow 2\mathrm{Pu^{3+}} + \mathrm{UO_2^{2+}} + 4\mathrm{H^+} \tag{2.3}$$

However, Pu(III) can be re-oxidized by nitric acid, a process autocatalyzed by nitrous acid ($\mathrm{HNO_2}$), as shown below:

$$\mathrm{Pu^{3+}} + \mathrm{HNO_2} + \mathrm{H^+} \rightarrow \mathrm{Pu^{4+}} + \mathrm{NO} + \mathrm{H_2O} \tag{2.4}$$

$$2NO + HNO_3 + H_2O \rightarrow 3HNO_2 \tag{2.5}$$

To suppress this back-oxidation and stabilize Pu(III), hydrazine (N_2H_4) is used as a nitrous-acid scavenger:

$$N_2H_4 + HNO_2 \rightarrow HN_3 + 2H_2O \tag{2.6}$$

Typical reductants therefore include uranous nitrate (U^{4+}), while hydrazine ensures the redox stability of the Pu(III) state during separation [23].

Industrially, large-scale PUREX plants operate at Sellafield (UK), La Hague (France), and Rokkasho (Japan), exemplifying decades of operational maturity. Continuous improvements—such as early U/Pu partitioning, salt-free reagents, and intensified equipment (e.g., pulsed columns)—have enhanced both efficiency and environmental performance [23].

Despite its success, PUREX technology remains limited to uranium and plutonium recovery. The separation of trivalent minor actinides (Am, Cm) from lanthanides is chemically challenging due to their similar ionic behavior. Consequently, research has shifted toward advanced aqueous partitioning processes, such as GANEX and CHALMEX, that enable comprehensive transuranic recycling within Generation IV fuel-cycle strategies [23].

2.1.2 Beyond PUREX: the DIAMEX–SANEX strategy for minor actinide separation

The industrial PUREX (Plutonium Uranium Redox EXtraction) process efficiently separates U and Pu from spent nuclear fuel, but leaves the trivalent minor actinides americium (Am) and curium (Cm) in the high active raffinate (HAR), together with lanthanides and most fission and activation products [24]. These trivalent actinides cannot be extracted by tributyl phosphate (TBP) under PUREX conditions and are therefore vitrified with the waste, where they dominate the long-term radiotoxicity and heat load of the final repository [24] .This limitation has motivated the development of advanced partitioning schemes that build directly on PUREX chemistry but extend its separation capability to Am(III) and Cm(III).

A key constraint is the chemical similarity of trivalent actinides (An(III)) and lanthanides (Ln(III)). Their comparable ionic radii and coordination chemistry, combined with the unfavourable An/Ln mass ratio in the raffinate, make the actinide–lanthanide separation both demanding and highly process-intensive [24]. At the same time, effective transmutation of minor actinides requires that lanthanides be removed because their large neutron-capture cross sections would otherwise strongly poison the transmutation target [24]. As a result, the strategy that has emerged over the last decades is a two-step solvent-extraction sequence—DIAMEX followed by SANEX—that can be viewed as a logical extension of PUREX toward full minor-actinide recycling [24].

2.1.2.1 DIAMEX as a PUREX-derived co-extraction step

DIAMEX (DIAMide EXtraction) is designed to treat the PUREX raffinate (or its concentrated high active concentrate, HAC) and to co-extract An(III) and Ln(III) from the highly acidic nitric medium using malonamide-based solvents [24]. In contrast to TBP in PUREX, the malonamide extractants (e.g. DMDBTDMA and the later reference molecule DMDOHEMA)

fulfil the CHON principle (C, H, O, N only), improving combustibility and reducing the potential for phosphorus-containing secondary wastes [24].

In the optimized DIAMEX flowsheets developed within the NEWPART and PARTNEW projects, 1 mol/L DMDOHEMA in an aliphatic diluent (TPH) is used to co-extract Am(III), Cm(III) and lanthanides from the concentrated raffinate [24]. Oxalic acid and HEDTA are added as masking agents to suppress the co-extraction of troublesome transition metals such as Zr, Mo and Pd, which would otherwise promote third-phase formation and compromise phase stability [24]. Both cold tests with simulated raffinate and hot tests with genuine fuel solutions have shown that more than 99.9% of Am(III) and Cm(III) can be recovered with high decontamination factors from most fission products, confirming that DIAMEX effectively extends PUREX to include trivalent minor actinides while keeping the overall process in a familiar liquid–liquid extraction framework [24].

However, DIAMEX deliberately co-extracts An(III) and Ln(III). From the viewpoint of transmutation, this is not sufficient: the presence of lanthanides in the actinide product stream would severely reduce neutron economy and transmutation efficiency [24]. Therefore, DIAMEX must be followed by a second highly selective step capable of separating Am and Cm from the lanthanide fraction.

2.1.2.2 SANEX as the selective actinide–lanthanide separation step

The SANEX (Selective ActiNide EXtraction) process was developed precisely to resolve the actinide–lanthanide separation problem that PUREX and DIAMEX cannot address alone [24]. After co-extraction in DIAMEX, the mixed An(III) + Ln(III) stream is subjected to a second solvent-extraction cycle in which soft donor ligands containing N or S atoms preferentially complex trivalent actinides over lanthanides [24]. Early breakthrough ligands were the bis-triazinyl-pyridines (BTPs), followed by the more robust bis-triazinyl-bipyridines (BTBPs), with $CyMe_4$BTBP becoming the reference SANEX extractant due to its combination of hydrolytic stability and high selectivity [24].

In typical SANEX flowsheets, $CyMe_4$BTBP is dissolved in an organic diluent together with a phase-transfer reagent such as DMDOHEMA or TODGA to overcome the intrinsically slow extraction kinetics of BTBP ligands [24]. Hot counter-current tests in centrifugal contactors using genuine high-level solutions have demonstrated that SANEX can achieve decontamination factors of the order of 10^3–10^4 for Am and Cm relative to lanthanides, with recovery yields above 99.9% [24]. In this way, the DIAMEX–SANEX sequence transforms the PUREX high-level raffinate into separate streams: a purified minor-actinide fraction suitable for transmutation and a lanthanide-rich fraction alongside the remaining fission products.

2.1.2.3 Limitations of DIAMEX–SANEX

Although DIAMEX–SANEX clearly represents a major conceptual and technological extension of PUREX, several limitations remain before such schemes can be considered industrially mature [24]. First, the overall process is intrinsically complex: it requires multiple extraction, scrubbing and stripping sections, sophisticated solvent formulations, and careful control of masking agents to avoid third-phase formation and precipitation. This multi-cycle architecture increases plant footprint, solvent inventory and operational costs compared to a single-cycle separation [24].

Second, the SANEX step suffers from kinetic and loading constraints. The slow mass-transfer kinetics of BTBP-based systems limits throughput and necessitates either increased contact time or larger contactor cascades, both of which are unfavourable for industrial deployment [24].

In addition, the organic phase has limited metal loading capacity, which can become critical when treating highly concentrated HAC feeds or scenarios with elevated minor-actinide content [24].

Third, long-term solvent stability under combined radiolytic and hydrolytic stress remains a key issue. While ligands such as $CyMe_4BTBP$ and DMDOHEMA have been optimized for improved resistance, their performance over prolonged operation and repeated regeneration cycles must still be demonstrated at larger scale [24]. Finally, the generation and management of secondary liquid and solid wastes (e.g. from masking agents, buffer salts and solvent-cleaning operations) must be addressed to preserve the overall environmental benefit of partitioning and transmutation [24].

These limitations have motivated the development of simplified flowsheets such as the innovative-SANEX (i-SANEX) and 1-cycle SANEX concepts, which aim to combine co-extraction and selective stripping into a single process and thereby reduce the number of cycles compared with the classical DIAMEX–SANEX route [24]. Nevertheless, DIAMEX–SANEX remains the most extensively demonstrated framework for minor-actinide recovery from PUREX raffinate and is a crucial stepping stone in the evolution from conventional PUREX reprocessing toward fully closed, transmutation-oriented fuel cycles [24].

2.1.3 The GANEX and EURO-GANEX processes: grouped actinide recovery for homogeneous recycling

The so-called GANEX (Grouped ActiNide EXtraction) process was originally developed at the CEA (Commissariat à l'énergie atomique et aux énergies alternatives) in France to enable the homogeneous recycling of all transuranium (TRU) elements in future closed nuclear fuel cycles [25]. Unlike the DIAMEX–SANEX system, which separates americium and curium individually from lanthanides, GANEX aims to recover all actinides—uranium (U), neptunium (Np), plutonium (Pu), americium (Am), and curium (Cm)—into a single product stream while fission products and lanthanides are rejected to the waste fraction. This grouped actinide recovery strategy reduces the number of separation stages and simplifies subsequent fuel fabrication for Generation IV fast reactors [25].

The GANEX process consists of two solvent-extraction cycles [25]. In the **first cycle**, uranium(VI) is selectively extracted from a highly acidic aqueous phase (approximately 5 mol/L HNO_3) into an organic phase containing **DEHiBA** (N,N-di(2-ethylhexyl)isobutyramide) dissolved in TPH, an industrial aliphatic diluent. Co-extracted technetium and neptunium are reduced and scrubbed with hydrazine in a scrubbing section operated at 1.5 mol/L HNO_3. These elements are then routed with the transuranium and fission products to the aqueous raffinate. Uranium is efficiently stripped from the loaded organic phase using a dilute nitric acid solution (0.01 mol/L). The first GANEX cycle was successfully demonstrated in the ATLANTE facility at CEA using genuine irradiated fast-reactor fuel, confirming that nearly all uranium can be removed while retaining more than 99.9% of the transuranium elements in the raffinate [25].

The raffinate from this first cycle serves as the feed for the **second GANEX cycle**, designed for the selective recovery of transuranium elements [25]. In this step, TRU, lanthanides, yttrium, molybdenum, technetium, zirconium, and iron are co-extracted into a solvent containing **DMDOHEMA** (N,N-dimethyl-N,N-dioctyl-2-(2-hexyloxyethyl)malonamide) and **HDEHP** (di(2-ethylhexyl)phosphoric acid) in TPH. The loaded solvent undergoes a sequence of selective stripping stages: molybdenum, ruthenium, and technetium are first stripped with 0.4 mol/L citric acid at pH 2.7; transuranium elements are then stripped using a solution containing 0.5 mol/L **HEDTA** (N-(2-hydroxyethyl)ethylenediaminetriacetic acid), 0.5 mol/L citric acid at pH 3, and 0.1 mol/L

hydroxyurea to reduce neptunium(VI); finally, lanthanides, zirconium, and iron are stripped using 0.5 mol/L oxalic acid and 0.2 mol/L **TEDGA** (tetraethyl diglycolamide). Although this process achieved excellent separation performance, its complex and pH-sensitive stripping sequence highlighted the need for simplification and improved robustness [25] .

Within the EURATOM project **ACSEPT**, an alternative second-cycle concept was developed—the **EURO-GANEX process**. The innovation of EURO-GANEX lies in its use of the water-soluble complexant **SO_3-Ph-BTP** (2,6-bis(5,6-di(3-sulphophenyl)-1,2,4-triazin-3-yl)pyridine), which selectively complexes trivalent actinides over lanthanides and allows stripping at higher acidities, eliminating the need for tight pH control [25]. The EURO-GANEX solvent consists of 0.2 mol/L **TODGA** (N,N,N,N-tetra-n-octyl diglycolamide) and 0.5 mol/L DMDOHEMA in Exxsol D80, a kerosene diluent. This mixture co-extracts Np(VI), Pu(IV), Am(III), Cm(III), and Ln(III) with a high plutonium loading capacity (up to 40 g/L, depending on acidity). DMDOHEMA acts primarily as a phase modifier, enhancing solvent stability and metal loading capacity [25]. Zr(IV) and Pd(II) are masked using **CDTA** (trans-1,2-cyclohexanediaminetetraacetic acid), while co-extracted Sr(II) and Fe(III) are scrubbed with 0.5 mol/L HNO_3. The transuranium elements are then stripped from the loaded solvent using a mixture of SO_3-Ph-BTP and **AHA** (acetohydroxamic acid), while the lanthanides remain in the solvent due to the higher nitric acid concentration in the stripping phase [25].

The EURO-GANEX process has been successfully demonstrated with genuine dissolved fast-reactor fuel using centrifugal contactors [25]. The first cycle achieved nearly complete uranium removal, and the second cycle recovered 99.9% of the transuranium elements, with only 0.06% of the lanthanide inventory routed to the TRU product. The overall decontamination factors were $DF_{Np} = 30$, $DF_{Pu} = 380$, and $DF_{Am} = 910$, while those for uranium and lanthanides were $DF_U = 3300$ and $DF_{Ln} = 1700$, respectively.

Despite these excellent results, research continues to optimize the process. Current efforts aim to simplify the solvent formulation by replacing DMDOHEMA with malonamide derivatives that exhibit lower fission-product extraction and by substituting SO_3-Ph-BTP with fully CHON-compliant hydrophilic ligands such as bis-triazolyl-pyridines [25]. Overall, the GANEX and EURO-GANEX systems represent a major advancement beyond DIAMEX–SANEX by enabling grouped actinide recovery compatible with fast-reactor fuel cycles. However, their chemical complexity, multi-component solvent formulations, and sensitive operating conditions have led to the exploration of more robust and simplified approaches—among them, the CHALMEX process developed at Chalmers University of Technology, which aims to preserve the grouped-actinide concept of EURO-GANEX while improving process sustainability and industrial feasibility [25].

2.2 The CHALMEX Process

The Chalmers GANEX (CHALMEX) process is a modified version of the second-cycle Group Actinide Extraction (GANEX) process, developed at Chalmers University of Technology in collaboration with Forschungszentrum Jülich. It was designed to achieve direct separation of transuranic elements (TRU: Np, Pu, Am, Cm) from fission products without requiring any redox control or chemical modification of the feed solution [26].

The CHALMEX solvent consists of 6,6-bis-(5,5,8,8-tetramethyl-5,6,7,8-tetrahydro-benzene-[1,2,4]-triazin-3-yl)-[2,2]-bipyridine ($CyMe_4$-BTBP) and tri-*n*-butyl phosphate (TBP) dissolved in the fluorinated diluent phenyl trifluoromethyl sulfone (FS-13). The combination leverages the strong affinity of $CyMe_4$-BTBP toward trivalent actinides due to the higher covalency in An(III)–N bonds

compared to Ln(III)–N bonds, resulting in efficient actinide–lanthanide separation [26, 27].

2.2.1 Experimental Flowsheet and Operating Conditions

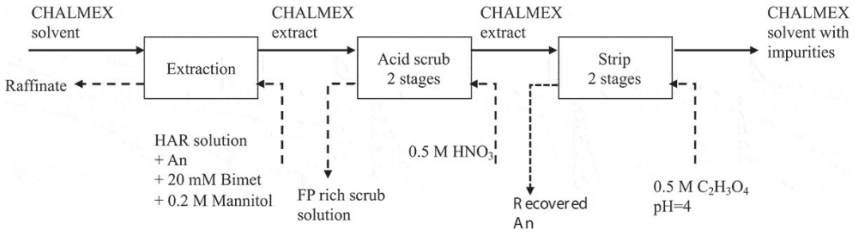

Figure 2.1: Suggested flowsheet for the CHALMEX FS-13 process

The process was experimentally tested through batch flowsheet experiments representing each stage of a counter-current extraction cascade (Figure 2.1). The organic phase consisted of 25 mM $CyMe_4$-BTBP in 30% v/v TBP and 70% v/v FS-13, pre-equilibrated in 4 M HNO_3. The aqueous phase simulated a PUREX raffinate based on a 3.2 M HNO_3 solution corresponding to 5000 $L{\cdot}t^{-1}$ dissolved UO_2 fuel (3.5% ^{235}U enrichment, 33 $GWd{\cdot}tHM^{-1}$ burnup, and 3 years cooling).

To minimize co-extraction of certain fission products (Mo, Zr, Pd), 0.2 M D-mannitol and 20 mM bimet were added to the raffinate as masking agents. The process sequence included:

1. Extraction from the simulated raffinate,

2. Two scrubbing stages using 0.5 M HNO_3 to remove co-extracted fission products and residual acidity,

3. Two stripping stages using 0.5 M glycolic acid adjusted to pH 4 with NaOH for TRU back-extraction.

Each contact stage was performed for 90 minutes at ambient temperature, followed by centrifugation to ensure phase separation. The concentrations of actinides and fission products were determined by alpha and gamma spectrometry and ICP-MS [26].

2.2.2 Distribution Behaviour and Number of Ideal Stages

The distribution ratios (D-values) observed in the extraction step were sufficiently high to achieve efficient recovery of the target actinides. Reported values include D(Am) ≈ 32, D(Cm) ≈ 13, D(Pu) ≈ 21, and D(Np) ≈ 10, confirming effective TRU extraction under the optimized solvent composition.

Ideal stage calculations indicated that three extraction stages are sufficient to recover 99.99% of americium, while four stages are needed for curium and neptunium. For plutonium, 99% recovery can be achieved within three stages. Under ideal conditions, a complete process using three extraction, three scrubbing, and two stripping stages results in recoveries of approximately 99.9% Am, 99% Cm, 94% Pu, and 61% Np [26].

These results highlight the simplified flowsheet of CHALMEX compared with other GANEX variants. Whereas the CEA-GANEX and EURO-GANEX flowsheets require 57 and 32 stages

respectively, the CHALMEX concept could theoretically achieve equivalent actinide recovery with only eight ideal stages [26, 28].

2.2.3 Fission Product Behaviour and Impurity Management

Fission products exhibiting significant extraction into the organic phase include Ni, Cd, Mo, Fe, Cu, Ag, and Sn. Among these, Ni and Cd show particularly high distribution ratios ($D > 40–100$), while Mo has $D \approx 2$ and is efficiently removed during the scrubbing stages with 0.5 M HNO_3. Fe, though present at high concentration in the raffinate ($\sim$1545 mg·L^{-1}), shows limited extraction ($D \approx 0.1$) but is not easily back-extracted, potentially leading to solvent loading.

Residual Ni, Cd, and Ag largely remain in the organic phase even after stripping, indicating a need for solvent clean-up to prevent metal build-up. This finding is crucial for future closed-cycle fuel designs since trace carryover of these impurities into recycled fuel could affect neutronic properties and material integrity [26].

2.2.4 Process Readiness and Implications

The CHALMEX process has currently achieved a Technology Readiness Level (TRL) of 2–3, reflecting successful cold tests under simulated conditions but lacking computer simulations and hot tests with genuine spent fuel. Advancing the TRL will require detailed process modeling and dynamic simulation to quantify mass-transfer efficiency and optimize stage configurations—an aspect directly relevant to the present thesis.

Overall, the CHALMEX process represents a simplified and potentially more economical alternative to existing GANEX processes, offering high actinide recovery with minimized fission product contamination. Its ongoing optimization is key to achieving sustainable nuclear fuel recycling with reduced waste volumes and improved resource utilization.

2.3 Fuel Fabrication Pathways

2.3.1 Fuel Fabrication by Internal Gelation Sol–Gel

Sol–gel routes are widely used in nuclear fuel technology to convert actinide nitrate solutions directly into microspheres, thereby avoiding the handling of highly radiotoxic powders. This is especially attractive for plutonium-bearing or minor-actinide-bearing fuels and for advanced fuel concepts such as fast-reactor sphere-pac fuel or coated-particle fuel for high-temperature gas-cooled reactors. In these systems, fuel is required in the form of dense, mechanically robust microspheres with a narrow size distribution, which can be achieved efficiently by sol–gel techniques [29].

Among the different sol–gel approaches, the *internal gelation process* is particularly relevant for advanced oxides, carbides, and nitrides. In internal gelation, the gelation chemistry is built into the droplet itself: a cold aqueous feed solution containing actinide nitrates, a "gelation pair" (hexamethylenetetramine, HMTA, and urea), and, when required, carbonaceous additives, is dispersed as droplets into a hot, immiscible organic liquid. Heating triggers in-situ hydrolysis and precipitation of the actinide species so that each droplet solidifies into a spherical gel particle. These gel microspheres can then be washed, calcined, and, if desired, converted by carbothermal reduction into carbide or nitride fuel kernels [29, 30].

2.3.2 Principle of Internal Gelation

The internal gelation process was originally developed at KEMA in the Netherlands for UO_2 kernel production and has since been extended to mixed (U,Pu) fuels and minor-actinide-bearing

compositions [29, 30]. The starting point is typically an acid-deficient uranyl nitrate (ADUN) solution, where the nitrate-to-uranium ratio is below the stoichiometric value of two (approximately 1.5–2). Using ADUN reduces the amount of gelation chemicals required and improves the stability of the feed.

To this cold metal nitrate solution, two key organic additives are introduced:

- **HMTA (hexamethylenetetramine)**, which, upon heating, decomposes and releases ammonia, and
- **Urea**, which forms transient complexes with uranyl ions and helps prevent premature hydrolysis and gelation at low temperature.

The feed "broth" is prepared at low temperature (around 0–5 °C) to keep HMTA and urea stable and to suppress early hydrolysis. At this stage, partial hydrolysis of the uranyl ion already occurs in the ADUN solution, forming small hydrolysed and oligomeric species, but the system remains fluid enough to be dripped.

Gelation is initiated when this cold broth is broken into small droplets and introduced into a hot organic medium, typically silicone oil. The droplets are formed using a nozzle, often with vibration to control size. As each droplet enters the hot oil, several coupled processes occur:

- the uranyl–urea complexes decompose,
- HMTA becomes protonated and subsequently decomposes, consuming protons and releasing ammonia, and
- the local pH inside the droplet rises.

This pH increase drives further hydrolysis and condensation of the actinide species, leading to the formation of a continuous hydrated oxide network. The droplet thus transforms into a rigid gel microsphere within a few seconds. For uranium systems, this gel consists of hydrated uranium oxides and ammonium-containing phases; for mixtures including zirconium or plutonium, analogous hydrated hydroxide or oxide gels are formed [30].

2.3.3 Post-Gelation Treatment

After gelation, the microspheres undergo post-treatment steps that ensure chemical stability and mechanical integrity before entering the fuel fabrication stage. These include washing and ageing in ammoniacal solution to remove residual gelation agents, followed by drying and calcination to yield oxide microspheres. Depending on the intended fuel type, the calcined oxides can be reduced to UO_2 or converted through carbothermal reduction into carbides or nitrides. This post-processing stage determines the final chemical composition of the fuel and ensures that impurities introduced during reprocessing or gelation are either removed or incorporated in stable forms [29, 30].

2.3.3.1 Advantages and Relevance for This Thesis

Internal gelation offers several advantages that make it particularly attractive in the context of closed fuel cycles and advanced actinide management [29, 30]:

- It avoids extensive powder handling of Pu- and MA-bearing materials, which is beneficial

for radiological safety and remote operation.

- It allows direct processing of actinide nitrate solutions, which are the natural products of aqueous reprocessing schemes such as PUREX or CHALMEX-derived flowsheets.

- It produces microspheres with controlled size and good mechanical properties, suitable for fast-reactor fuels and for concepts where microstructural control is important (e.g., high burnup, high thermal conductivity, or coated particles).

- It is compatible with the fabrication of oxide, carbide, and nitride fuels by appropriate choice of carbon additives and heat treatment.

In the framework of the present thesis, the internal gelation sol–gel route is not simulated in chemical detail. Instead, it provides the conceptual link between:

1. the actinide product stream emerging from the CHALMEX FS-13 process (containing uranium, plutonium, and selected fission product impurities), and

2. the final fuel form that is loaded into the fast reactor core.

The key assumption is that actinide nitrate solutions, with their associated impurity vectors defined by CHALMEX, are converted by internal gelation into oxide (or nitride) microspheres that are then used as fuel material. The neutronic impact of the impurities—rather than the detailed chemistry of droplet gelation—is the focus of this work. Nevertheless, the internal gelation process is essential background, because it justifies:

- the use of an actinide-nitrate-based feed,

- the presence of certain metallic and lanthanide impurities carried over from the aqueous phase, and

- the realistic fabrication of fast-reactor fuel from CHALMEX-derived actinide solutions.

2.4 Benchmark Context: Superphénix (SPX)

Superphénix (SPX) was a 3000 MW_{th} sodium-cooled fast reactor (SFR) constructed at the Creys-Malville site along the Rhône River in France. With an electrical output of 1240 MWe, it remains the most powerful SFR ever built and represents the culmination of the French fast reactor programme following Rapsodie and Phénix. Designed and operated jointly by the French Atomic Energy Commission (CEA) and Électricité de France (EDF), its purpose was to demonstrate large-scale plutonium recycling, validate fast-spectrum neutronics, and assess the technical and economic feasibility of breeder reactors for a closed nuclear fuel cycle [31].

Superphénix adopted a pool-type configuration, in which the entire primary circuit—including the reactor core, primary sodium pumps, and intermediate heat exchangers—is contained within a single large vessel filled with liquid sodium. Four independent secondary sodium loops transfer heat from the primary system to four steam generators located in adjoining buildings, which in turn feed two 620 MWe steam turbines. This design provided both high power density and inherent safety features, such as low operating pressure and the large thermal inertia of the sodium coolant [31].

The reactor core itself was a heterogeneous system consisting of inner and outer fissile zones surrounded by a fertile radial blanket, steel reflector subassemblies, and a peripheral shielding region. The fissile region contained mixed oxide (MOX) fuel composed of UO2-PuO2 with two plutonium enrichments: approximately 15% in the inner zone and 19% in the outer zone. This enrichment zoning was adopted to flatten the neutron flux distribution and ensure more uniform power generation across the core [31]. Each fissile subassembly contained 271 fuel pins arranged in a triangular lattice within a hexagonal wrapper (hexcan). Fertile breeder subassemblies, made of uranium oxide, contained 91 thicker pins and formed the outer radial blanket that served to capture escaping neutrons for plutonium breeding.

Control and shutdown rod assemblies were located within and between the fissile zones. Each control assembly contained a bundle of 31 boron carbide (B_4C) pins enriched to 90% in ^{10}B, housed in a hexagonal sheath. Three diverse shutdown rods (DSD) provided an additional layer of safety redundancy. Surrounding the active core, steel diluent and reflector subassemblies attenuated neutron leakage and limited sodium activation in external structures [32].

The Superphénix benchmark core model used in this thesis is derived from the start-up configuration defined by Ponomarev *et al.* [32] and later validated by Litaize *et al.* [33]. The benchmark provides a detailed heterogeneous description of the fuel pins, cladding, subassembly wrappers, and coolant regions, representing nearly all structural elements of the reactor core. Radially, the model comprises 190 inner-core (IC) subassemblies, 168 outer-core (OC) subassemblies, 225 radial breeder blankets (RB), 18 steel diluent assemblies, 21 control and shutdown rods (CSD), 3 diverse shutdown rods (DSD), and 294 steel reflectors. Axially, each subassembly includes lower and upper fertile blankets, a fissile column approximately 1 m high, and gas plenums for fuel expansion and sodium flow management.

Four thermal states are defined in the benchmark to represent material expansion and density variations: (1) As-Fabricated (20 °C), (2) Cold (180 °C), (3) Hot Zero Power (400 °C), and (4) Hot Full Power (HFP) conditions corresponding to nominal operation. Thermal expansion of steel, MOX fuel, and B4C absorber materials is calculated using temperature-dependent coefficients for 316Ti and 304L stainless steels. These parameters ensure accurate density corrections and geometry consistency across thermal states [32].

In the context of the present work, simulations are limited to the inner fissile assembly region, which represents the most neutronically active zone of Superphénix. This region exhibits the hardest neutron spectrum and the strongest sensitivity to material composition changes, making it suitable for assessing the impact of CHALMEX-derived impurities on reactivity, flux spectra, and transmutation behaviour. By focusing on this segment while maintaining benchmark consistency, the study ensures both computational efficiency and high physical relevance to fast-spectrum reactor performance.

Chapter 3

Methodology

The methodology here after integrates depletion physics, actinide separation chemistry, and fast reactor modelling in order to evaluate the feasibility of recycled CHALMEX-derived fuels in a Gen IV fast-spectrum environment. The workflow ensures that each stage—from LWR spent-fuel irradiation to to ideal re-fabrication of the recovered isotopic vector and SPX-core simulation—is physically consistent and representative of realistic fuel cycle conditions.

3.1 Reference LWR Depletion and Spent Fuel Inventory

The starting point of this work was the selection of a representative light water reactor (LWR) system and the generation of a realistic spent nuclear fuel (SNF) inventory to be used as feed for the CHALMEX process. A pressurised water reactor (PWR) fuel assembly, based on the simple 2D EPR assembly geometry from the Serpent tutorial [34], was modelled and depleted using the Monte Carlo neutron transport and burnup code Serpent 2 [22].

The reference fuel was irradiated to a discharge burnup of 35 GWd/tHM with a U-235 5% enrichment and subsequently cooled for three years. After this cooling time, the isotopic composition of the SNF was extracted from the Serpent depletion output and used as the starting inventory for the separation studies. The depletion calculation included normal UO_2 fuel pins, gadolinium-bearing fuel pins and Zircaloy-4 cladding, arranged in a 17×17 lattice with light water coolant and soluble boron. The assembly linear power was set to 420 kW, reflective boundary conditions were applied in the radial directions, and burnup points were defined between 0.1 and 35 GWd/tHM to resolve the evolution of the fuel composition during irradiation.

3.2 CHALMEX Process and Refabrication of Recycled Fuel

The SNF composition obtained from the LWR depletion calculation was then used as the basis for the Chalmers Grouped Actinide Extraction (CHALMEX) process, which was evaluated in the Department of Nuclear Chemistry. After a consistency check of the calculated isotopic inventory to ensure that it was representative of the expected composition at 35 GWd/tHM and three years of cooling, the simulated fuel was conceptually subjected to the steps of the CHALMEX flowsheet.

In the CHALMEX process, the dissolved spent fuel undergoes a sequence of extraction, scrubbing and stripping stages designed to co-extract and recover the actinides of interest while rejecting

fission products. In this work, ideal behaviour was assumed and no process losses of actinides were considered, so that the entire amount of recovered actinides was available for fabrication of new fuel.

The recycled fuel was then refabricated via the sol–gel technique, specifically using an internal gelation process. This refabrication route, including the practical implementation and process optimisation, was carried out by the Department of Nuclear Chemistry. A detailed description of the sol–gel internal gelation methodology lies outside the scope of this thesis and the reader is referred to their work for further information [30]. In the present work, the outcome of the CHALMEX process and subsequent sol–gel refabrication is treated as an idealised recycled fuel vector, which is then used as input for the fast reactor calculations described in Chapters 3 and analysed in Chapter 4.

3.3 Core Model and Geometry

The SPX benchmark core is arranged in a hexagonal lattice with a nominal pitch of 17.9 cm and comprises different types of subassemblies, including fissile fuel, fertile blanket, control, and shielding assemblies. Illustrations of both the general, radial and axial configurations of the SPX model core are shown in Figure 3.1 and Figure 3.2 to provide a visual reference of the model.

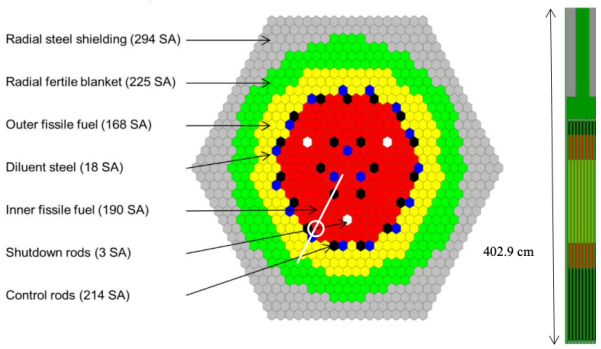

Figure 3.1: Radial and axial layout of the SPX benchmark core [35].

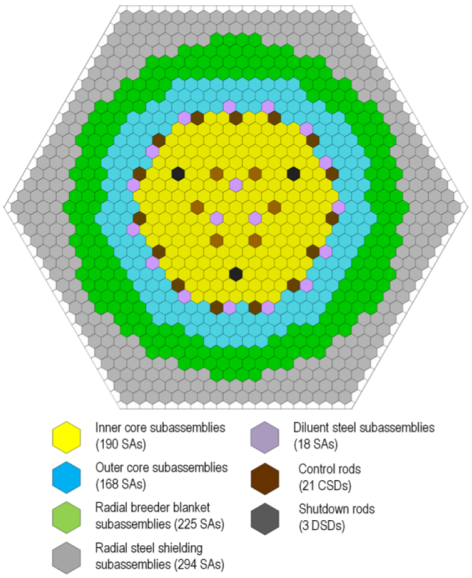

Figure 3.2: General layout of the SPX benchmark core [32].

In the present study, the analysis is restricted to the inner fissile fuel region. This region is modeled as a 2D infinite hexagonal lattice based on the fissile fuel subassembly geometry, providing a representative description of the fissile fuel environment. The fissile fuel subassembly consists of 271 fuel pins arranged in a hexagonal bundle and separated by a spacer wire wrap. The radial cross section of the pin bundle at the level of the fissile fuel pellet is shown in Figure 3.3.

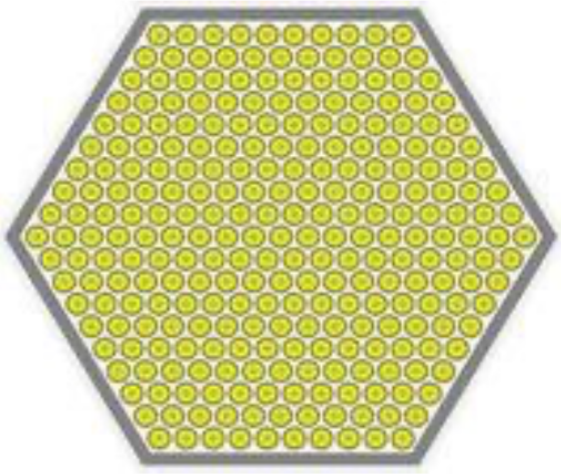

Figure 3.3: Fissile subassembly cross section of the Superphénix (SPX) benchmark core, illustrating the pin arrangement and subassembly layout as defined in the SPX benchmark specification [32].

3.3.1 Operational Parameters

The Superphénix (SPX) fast reactor operates at a nominal thermal power of 2990 MW_{th}. A reference power map of the full SPX benchmark core, obtained from published Serpent-based benchmark calculations, is shown in Figure 3.3 and is included to illustrate the radial distribution of power across the different core regions and to identify the inner fissile fuel zone [32, 33]. No full-core neutronic calculations were performed in the present work.

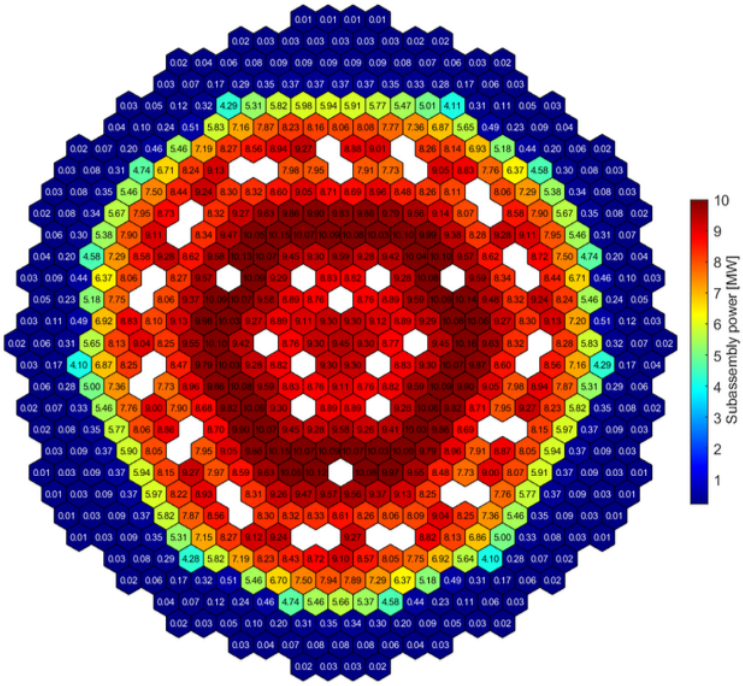

Figure 3.4: Subassembly power distribution in the SPX benchmark core, obtained from reference Serpent calculations reported by Ponomarev et al. [32]. The figure is shown for illustration of the different core regions and is not the result of calculations performed in this work.

As discussed in Section 3.3, the scope of this study is restricted to the inner fissile fuel region of the SPX core. This region is characterised by the highest neutron flux and power density and is therefore representative of the local neutronic environment relevant for fuel composition and impurity studies. Consequently, only fissile fuel is explicitly modelled, and all operational parameters are defined to be representative of the inner fissile region.

The computational model adopts a two-dimensional infinite hexagonal lattice geometry based on the fissile fuel subassembly design of the SPX benchmark. The lattice represents a repeating arrangement of identical fissile subassemblies and is intended to reproduce the local operating conditions of the inner fissile zone while neglecting global core heterogeneities, non-fissile assemblies, and control components. This approach is commonly employed in lattice-level neutronic analyses to isolate intrinsic fuel behaviour without the influence of full-core effects [32].

The power level associated with the inner fissile region, as reported in the SPX benchmark literature, is used exclusively as a reference for normalisation. This reference power is rescaled to the reduced lattice geometry employed in this work. The resulting normalisation ensures consistency between the local power density imposed in the simulations and the operating conditions of the inner fissile region.

Monte Carlo simulations were normalised using the `set powdens` card in Serpent 2, prescribing a fuel power density of 0.08748 $\mathrm{kW\,g^{-1}}$ of heavy metal. This value was derived by scaling the benchmark power attributed to the inner fissile zone by the total fuel mass represented in the lattice model, ensuring that the imposed power density is consistent with the local operating conditions reported for the SPX inner fuel assembly [22, 32].

With the computational domain normalised to a power of 0.08748 $\mathrm{kW\,g^{-1}}$ of heavy metal, the fuel temperature was fixed at 1500.15 K, consistent with SPX benchmark operating conditions. The coolant temperature was set to an average value of 743.15 K, corresponding to the mean of the primary sodium inlet and outlet temperatures reported for the reactor [32]. The sodium coolant density adopted in the model was 0.8416 $\mathrm{g\,cm^{-3}}$, consistent with this operating temperature.

The fissile fuel was modelled as mixed oxide $(\mathrm{U,Pu})\mathrm{O_2}$, including a trace amount of $^{241}\mathrm{Am}$ originating from the plutonium vector, using the isotopic composition specified for the SPX inner fissile fuel in the benchmark definition. The complete isotopic vector implemented in Serpent is reported in Table 3.1.

The corresponding theoretical fuel density adopted in the Serpent input was 11.0584 $\mathrm{g\,cm^{-3}}$, in agreement with the SPX benchmark fuel specifications [32]. These material parameters were applied consistently in all Serpent 2 simulations presented in this work.

For clarity and ease of interpretation, the uranium-only and plutonium-only isotopic vectors used to construct the mixed oxide fuel are listed separately in Tables 3.2 and 3.3, respectively.

Table 3.1: Isotopic vector of the (U,Pu)O_2 fuel used in the Serpent 2 simulations.

Isotope	**Atomic number densities ($\times 10^{24}$ cm^{-3})**
^{235}U	1.01274×10^{-4}
^{238}U	1.98991×10^{-4}
^{238}Pu	1.78335×10^{-5}
^{239}Pu	2.45976×10^{-4}
^{240}Pu	7.33391×10^{-4}
^{241}Pu	1.97174×10^{-4}
^{242}Pu	6.84331×10^{-4}
^{241}Am	4.822584×10^{-4}
O	4.65798×10^{-4}

The uranium isotopic vector used in the fissile fuel was ^{238}U = 0.995 and ^{235}U = 0.005 (mass fractions). The inner fuel assembly fissile inventory was defined with a plutonium mass share of 16%, leaving 84% uranium; the overall fuel density was then calculated from this 84/16 split.

Table 3.2: Isotopic vector of uranium used in the fissile fuel.

Isotope	**Mass fraction**
^{238}U	0.995
^{235}U	0.005

Table 3.3: Plutonium isotopic vector used in the benchmark .

Isotope	**Pu mixture used in benchmark (% mass)**
Pu-238	0.50
Pu-239	69.67
Pu-240	20.86
Pu-241	5.63
Pu-242	1.96
Am-241	1.38

3.3.2 Geometry Parameters

The geometry of the model was constructed to represent the inner fissile subassembly region of the SPX reactor. The configuration follows a hexagonal lattice arrangement consistent with the reference benchmark specifications [35, 36]. Each fuel pin consists of concentric cylindrical regions corresponding to the MOX fuel, the stainless steel cladding, and the sodium coolant channel. The pins are arranged in a hexagonal lattice to reproduce the assembly-level geometry of the inner fissile zone.

The model adopts a simplified representation of the configuration at midplane, assuming radial

symmetry and applying reflective boundary conditions in the x and y directions, while a vacuum (black) boundary condition is applied along the z axis (boundary condition **3 3 1**). This configuration effectively eliminates radial neutron leakage, reproducing the behaviour of an infinite two-dimensional lattice in the radial plane, while allowing axial neutron leakage.

This approach is commonly used in lattice physics calculations to study the intrinsic neutronic behaviour of a fuel region without the distortions associated with full-core geometry. The reflective boundaries in the radial directions ensure that neutrons encountering the boundary are mirrored back into the system, emulating an infinitely repeating lattice. The axial vacuum boundary condition prevents non-physical neutron accumulation and keeps the model computationally efficient, making it suitable for midplane 2D simulations.

All major structural components, including the fuel, cladding, and coolant, were assigned to separate `cell` definitions within distinct `universes` in the Serpent input file. The universe hierarchy was constructed so that the basic fuel pin forms the lowest-level universe, which is then repeated within the fuel assembly lattice.

This hierarchical structure enables efficient geometry repetition and consistent treatment of material compositions across the model. The lattice pitch, pin diameters, and cladding thickness were based on the SPX benchmark data, adjusted to maintain geometrical fidelity within the restricted inner fissile region domain.The geometric parameters used in the model—including subassembly dimensions, pin pitch, cladding thickness, and fuel pellet geometry—are taken directly from the SPX benchmark definition. These parameters are summarised in Table 3.4 and correspond to the reference inner fissile subassemblies of the SPX reactor [32]. The geometry is therefore representative of the benchmark inner fissile region and provides a consistent basis for subsequent fuel composition and impurity analyses.

With the modelling framework established, a depletion simulation of the unperturbed SPX benchmark was executed to obtain a consistent reference evolution of isotopic inventories and reactivity. This reference case forms the basis for comparison with the various material configurations derived from the CHALMEX process and supplied by the Department of Nuclear Chemistry.

Table 3.4: Geometric parameters of the inner-core fissile subassemblies in the SPX benchmark.

Parameter	**Value**	**Unit**
Hexcan outer flat-to-flat size	173.0	mm
Hexcan wall thickness	4.5	mm
Subassembly pitch in the diagrid	179.0	mm
Number of fuel pins per subassembly	271	–
Pin pitch	9.8	mm
Spacer-wire diameter	1.2	mm
Pin cladding outer diameter	8.50	mm
Pin cladding thickness	0.565	mm
Fissile fuel pellet diameter	7.14	mm
Fissile fuel pellet inner hole diameter	2.0	mm
Fertile (axial blanket) pellet diameter	7.07	mm
Height of fissile pellet stack	1.00	m
Equivalent diameter of fissile core	3.70	m
Volume of fissile core	10.75	m^3

3.4 Materials and Cases

This section presents an in-detail description of the fuel compositions defined in collaboration with the Department of Nuclear Chemistry at Chalmers University of Technology. The goal was to establish recycled fuels that closely mirror the fissile material specifications of the Superphénix (SPX) benchmark. To that end, four different MOX fuel scenarios based on continuous evaluation and recalibrations from simulative feedbacks were prepared by means of the CHALMEX separation flowsheet followed by an idealized refabrication step conceptually based on the internal gelation sol–gel process.

All recycled fuels were built on a uranium matrix originating from depleted LWR (EPR) spent fuel (without considering the fuel with gadolinium): the uranium matrix (U-matrix) was taken from the Serpent 2 depletion output of the reference EPR assembly and then blended with plutonium to produce MOX compositions that could reach criticality under fast-spectrum SPX-like conditions. For each case, the uranium-to-plutonium mass ratio was varied in order to identify practical compositions that are both physically meaningful and neutronically compatible with the specified domain.

Based on the SPX reference MOX fuel composition, a set of uranium–plutonium ratio variations was defined to investigate the sensitivity of neutronic behaviour to plutonium content. Four primary MOX compositions were selected for this screening analysis, spanning a representative range of plutonium fractions around the benchmark value. The investigated MOX cases are summarised in Table 3.5.

- **MOX-90/10:** U/Pu = 90/10 (mass %)
- **MOX-85/15:** U/Pu = 85/15 (mass %)

- **MOX-80/20:** U/Pu = 80/20 (mass %)
- **MOX-75/25:** U/Pu = 75/25 (mass %)

Table 3.5: Summary of MOX cases considered in this study.

Case name	**U : Pu (mass %)**
MOX-90/10	90 : 10
MOX-85/15	85 : 15
MOX-80/20	80 : 20
MOX-75/25	75 : 25

All four fuel mixtures were tested in Serpent 2 to evaluate their criticality behaviour under the reference SPX fast-spectrum conditions. Although every mixture reached or approached criticality, the MOX-90/10 case exhibited an unstable behaviour, transitioning from subcritical to strongly supercritical under the chosen model conditions, which is believed to be due to the breeding nature of the reactor due to the production of Pu-239. Consequently, compositions in the range of 85/15 and 80/20 were investigated more closely because their reactivity behaviour was more moderate and representative of realistic operating cases.

Following this initial screening, a second set of calculations added a representative fraction of minor actinides (MAs) to each MOX mixture to assess the sensitivity of reactivity and spectral features to MA content. The minor actinide fractions introduced in each case, used to assess sensitivity to TRU content, are summarised in Table 3.6. Again, all cases approached criticality; however, MOX-80/20 (with added minor actinides) displayed the most realistic and stable neutronic behaviour for the objectives of this thesis. Therefore, the final case selected for the impurity and transmutation studies corresponds to the MOX-80/20 composition (U : Pu = 80 : 20 mass%), including the CHALMEX-derived impurity vector introduced during the refabrication step.

Table 3.6: Summary of MOX+TRU fuel cases considered in this study.

Case name	**U : Pu (mass %)**	**Added TRU (mass %)**
MOX+TRU-90/10	90 : 10	0.21
MOX+TRU-85/15	85 : 15	0.31
MOX+TRU-80/20	80 : 20	0.42
MOX+TRU-75/25	75 : 25	0.52

The MOX-80/20 case thus serves as the reference recycled fuel in subsequent analyses, while the other mixtures are retained for sensitivity comparisons.

3.5 Metrics of Evaluation

3.5.1 Multiplication Factor and the Fission Chain Reaction

An essential principle of nuclear reactor physics is that the neutrons released in one fission event can induce additional fissions. To sustain a stable fission chain reaction—and thus maintain a constant production of fission energy—the reactor must be designed so that the rate of neutron production balances the losses due to absorption and leakage [37].

If this balance is achieved, the chain reaction propagates in a steady-state manner, with neutrons acting as the "carriers" of the chain. To maintain such a steady-state reaction, the reactor must be configured such that, on average, *exactly one* neutron from each fission induces a subsequent fission. The remaining neutrons are either absorbed without causing fission or leak from the system. This delicate balance is the central requirement of reactor criticality. This fundamental mechanism is schematically illustrated in Figure 3.5.

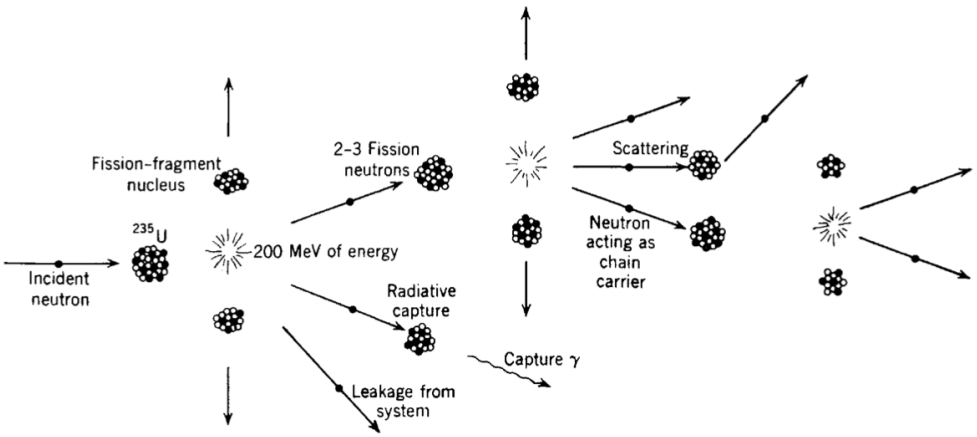

Figure 3.5: Schematic representation of a neutron-induced fission chain reaction [37].

This requirement can be expressed quantitatively. Let the number of neutrons in two successive fission-generations be compared. The ratio of these populations defines the *multiplication factor*,

$$k = \frac{\text{number of neutrons in generation } i+1}{\text{number of neutrons in generation } i}. \tag{3.1}$$

This quantity determines the state of the chain reaction:

- $k = 1$: the neutron population is constant — the system is *critical*;
- $k < 1$: the neutron population decreases — the system is *subcritical*;
- $k > 1$: the neutron population increases — the system is *supercritical*.

The objective of reactor design is therefore to achieve $k = 1$, ensuring a stable power level.

3.5.1.1 The Four-Factor Formula

Every neutron born from fission has two fundamental possible outcomes: it may leak out of the reactor, or, if it remains within the system, it must eventually be absorbed. Absorptions may be nonproductive (radiative capture) or may induce fission, producing a new generation of neutrons [37]. A schematic representation of these neutron pathways is shown in Figure 3.6.

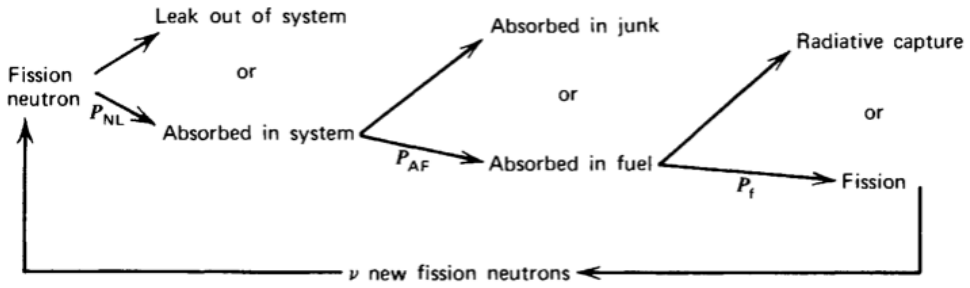

Figure 3.6: Schematic representation of neutron destinies: leakage, capture, or fission [37].

In an *infinite* homogeneous system—where leakage is absent—the neutron balance may be expressed through the four-factor formula, which defines the infinite-medium multiplication factor:

$$k_\infty = \eta\, f\, p\, \varepsilon. \tag{3.2}$$

Here:

- η: reproduction factor (neutrons produced per thermal absorption in fuel);
- f: thermal utilization factor (fraction of absorptions occurring in fuel);
- p: resonance escape probability;
- ε: fast fission factor.

This expression characterizes the ability of the fuel material and moderator to sustain a chain reaction independent of geometry or leakage effects.

3.5.1.2 Finite vs. Infinite Systems: Distinguishing k_∞ and k_{eff}

In real reactor systems, which are finite in extent, and neutron leakage therefore reduces the effective multiplication factor [37]. Accordingly, for a finite system the multiplication factor becomes:

$$k_{\text{eff}} = k_\infty\, P_{FNL}\, P_{TNL}, \tag{3.3}$$

where P_{FNL} and P_{TNL} are the fast and thermal non-leakage probabilities, respectively [37]. This expression is known as the six-factor formula.

Thus:

- k_∞ is a *material property*, representing the multiplication factor in an infinite homogeneous medium with no leakage;
- k_{eff} characterizes the behaviour of a real, finite reactor including geometric leakage.

3.5.1.3 Relevance to This Work

In the Serpent 2 simulations performed in this thesis, the geometry represents a two-dimensional infinite lattice by applying reflective boundary conditions in the radial directions and vacuum in

the axial direction:

```
set bc 3 3 1
```

These reflective boundaries eliminate radial neutron leakage, thereby enforcing infinite-lattice behaviour in 2D. As a consequence:

$$k_{\text{eff}} = k_{\infty} \tag{3.4}$$

for the simulated 2D system. Therefore, all reactivity analyses in this work are based on the quantity `inf_kinf` extracted from the Serpent output, which corresponds to the theoretical infinite-medium multiplication factor.

This approach is appropriate for isolating the effect of material composition—specifically the addition of recycled actinides and impurities—on the neutronic performance of the SPX fast reactor fuel.

3.5.2 Depletion and Isotopic Evolution

Fuel irradiation in a reactor leads to continuous changes in isotopic composition due to fission, neutron capture, and radioactive decay. This time-dependent evolution affects the neutron spectrum, reactivity, and the buildup of minor actinides and fission products, and must therefore be included in any realistic neutronic analysis.

3.5.2.1 Physical Basis of Fuel Depletion

The time evolution of nuclide densities is governed by the Bateman equations, which couple radioactive decay, neutron-induced reactions, and formation terms from parent nuclides. In matrix form, the depletion system is written as:

$$\frac{d\mathbf{N}(t)}{dt} = \mathbf{A}\,\mathbf{N}(t), \tag{3.5}$$

where $\mathbf{N}(t)$ is the vector of nuclide densities and $\mathbf{A}$ is the depletion matrix containing decay constants and reaction rates. As discussed in standard reactor physics literature [37], solving this system requires simultaneous treatment of transmutation chains involving U, Pu, minor actinides, and fission products.

3.5.2.2 Numerical Depletion in Serpent 2

Serpent 2 solves the depletion equations using the Chebyshev Rational Approximation Method (CRAM), combined with a predictor–corrector iteration for improved stability and accuracy. Reaction rates are obtained from continuous-energy Monte Carlo transport at each burnup step, and the nuclide vector is subsequently updated. This tightly coupled transport–depletion scheme ensures that spectral changes caused by evolving fuel composition are treated self-consistently.

3.5.2.3 Depletion Setup for the Reference Lattice Model

Depletion calculations were performed for a representative two-dimensional hexagonal lattice model corresponding to a repeating fissile fuel pin array defined according to the SPX benchmark geometry described in Section 3.3 and summarised in Table 3.4. The Monte Carlo depletion simulations were normalised to a specific power of 0.08748 $\mathrm{kW\,g^{-1}}$, corresponding to the fuel mass contained within the modeled lattice domain. This power level was obtained by rescaling the reference operating conditions of the SPX benchmark to the reduced lattice geometry, ensuring

consistency with the local power density applied in the simulations. All relevant nuclides present in the fissile (U,Pu)O_2 fuel were included in the depletion chain, including uranium and plutonium isotopes, minor actinides, and selected fission products. The depletion analysis therefore captures the time-dependent isotopic evolution of the fuel under irradiation conditions characteristic of fast-spectrum sodium-cooled reactor operation.

Burnup was simulated using 20 non-uniformly spaced steps covering the range from 0.1 MWd/kgHM to 65 MWd/kgHM. At each burnup step, full neutron transport calculations were performed to update reaction rates and the neutron spectrum.

All four baseline MOX fuel compositions (90/10, 85/15, 80/20, and 75/25) were initially irradiated up to a burnup of 90 MWd/kgHM. This extended irradiation range was selected because the 90/10 mixture exhibited a behaviour that diverged from the expected trend of the SPX benchmark. Specifically, for the 90/10 case, the infinite-medium multiplication factor k_∞ was observed to increase with burnup instead of decreasing. In order to determine whether this behaviour would stabilise or reverse at higher irradiations, the same burnup interval was consistently applied to all MOX cases.

The increasing trend of k_∞ in the 90/10 fuel persisted across the entire 90 MWd/kgHM range. This behaviour is physically consistent with fast-spectrum breeder conditions. In the 90/10 fuel composition, the high ^{238}U content enhances neutron capture reactions leading to the breeding of ^{239}Pu. As burnup progresses, the accumulation of newly formed fissile ^{239}Pu can compensate for, and in this case outweigh, the depletion of initial fissile material, resulting in an overall increase in reactivity.

In contrast, the remaining MOX compositions (85/15, 80/20, and 75/25) displayed a decrease in k_∞ with burnup, in agreement with the SPX benchmark behaviour. This distinction played an important role in shaping the methodological workflow of this study. When transitioning from pure MOX fuels to MOX+TRU mixtures, and subsequently to the final fuel configuration used for the impurity analysis, attention was focused on those compositions whose reactivity evolution matched the SPX reference trends.

For the MOX+TRU cases, as well as for the final selected fuel into which impurities were introduced, the depletion calculations were instead limited to 65 MWd/kgHM. This burnup range was sufficient to capture the relevant neutronic trends for these compositions while remaining consistent with their benchmark-like behaviour.

Although a detailed discussion of the anomalous 90/10 trend is deferred to the results chapter, it is essential to introduce it in this methodological section, as it directly motivated the transition from the initial MOX screening to the selection of the final recycled fuel composition used for the impurity studies.

In all depletion and branch calculations, Serpent 2 produced a consistent set of neutronic and isotopic outputs for each burnup step and for every branch condition investigated. These outputs represent the core quantities required to analyse the behaviour of the SPX inner-subcore fuel under irradiation. Specifically, the results included the isotopic composition of the depleted fuel, showing the evolution of uranium, plutonium, minor actinides, and relevant impurities as a function of burnup.

In addition, Serpent provided the infinite-medium multiplication factor k_∞, which was used throughout this work to quantify reactivity changes in the 2D infinite-lattice model.

3.6 Doppler Reactivity Feedback Coefficient

In order to evaluate the neutronic performance of a Generation IV system, it is essential to assess how the reactor responds to increases or decreases in fuel temperature, and whether it can remain efficient from both an operational and a safety point of view. To carry out such an evaluation, it is necessary to perform calculations that quantify how far the reactor departs from its intended operating state under conditions that affect the fuel temperature. It is important to note that, in the design phase, nuclear power systems are configured so that, under nominal conditions, the reactor achieves a value of $k_{\text{eff}} \approx 1$, meaning a balance between the number of neutrons produced and those lost by leakage or absorption. Within this context, the Doppler reactivity feedback coefficient plays a role of fundamental importance, as it determines how changes in fuel temperature perturb this balance and thus directly influence both the stability and safety of reactor operation. In the following, the Doppler reactivity feedback coefficient is defined and the methodology adopted for its evaluation in this work is presented.

The change in fuel temperature has a direct impact on the neutron interaction cross sections of the fuel. As reported by Thilagam et al. [38], an increase in fuel temperature causes a broadening of the resonances in the microscopic cross sections, accompanied by a reduction in their peak magnitude. This phenomenon, known as *Doppler broadening*, affects the probability that neutrons are captured rather than inducing fission, thereby altering the effective multiplication factor of the system.

Because of this sensitivity, the evaluation of the Doppler fuel temperature coefficient requires isolating the temperature effect by varying the fuel temperature while keeping all other parameters fixed—including moderator temperature, moderator density, boron concentration, xenon poisoning, and burnup conditions [38]. This ensures that the calculated reactivity variation is attributable solely to fuel temperature changes.

3.6.1 Definition of the Doppler Coefficient

Fiorito et al. [39] define the Doppler fuel temperature coefficient of reactivity as

$$\alpha_D(T) = \frac{\mathrm{d}k}{\mathrm{d}T}, \tag{3.6}$$

where k is the effective neutron multiplication factor and T is a characteristic fuel temperature adopted in the transport model. In practical Monte Carlo calculations, the coefficient is typically obtained by evaluating the system at two different fuel temperatures, T_1 and T_2, and computing the corresponding change in the multiplication factor:

$$\Delta k = k_2 - k_1. \tag{3.7}$$

In this work, this finite-difference evaluation of the Doppler coefficient was implemented by means of branch calculations in Serpent 2. Branch calculations in Serpent 2 are both computationally and time intensive, because they require first performing a reference burnup calculation covering all relevant fuel assembly types and burnup steps, and then carrying out a series of restart calculations at selected burnup points, in which the local operating conditions are systematically varied. In practice, a base burnup calculation is executed once, after which the code is restarted for chosen burnup points; for each restart, Serpent 2 activates a set of user-defined branches to different state points via the `branch` card. The combinations of variations are specified by a coefficient matrix (the `coef` card), which was adopted in this work. With coefficient matrices, the automated burnup sequence is restricted to performing branch variations, and any variations in the number of particle histories must be handled by preparing separate input files. Since the

scope of this study was limited to branch calculations, only the coefficient-matrix approach was employed.

In the present model, branch calculations were defined to modify the fuel temperature, coolant temperature and density using the `stp` option in SERPENT 2. For a specified temperature, the code selects the closest available cross-section data set below the target value and applies the built-in Doppler-broadening pre-processor to generate cross sections at the exact user-defined temperature. This procedure follows the standard temperature treatment implemented in SERPENT 2 [40] .

.

3.6.2 Reactivity-Based Formulation

Following the reactivity-based formulation proposed by Thilagam et al. [38], the Doppler effect is quantified by evaluating the change in reactivity between two reactor states differing only in fuel temperature.

The reactivity change is defined as

$$\Delta\rho = \frac{k_{\text{eff}}^{(T_2)} - k_{\text{eff}}^{(T_1)}}{k_{\text{eff}}^{(T_2)}\, k_{\text{eff}}^{(T_1)}}, \tag{3.8}$$

where $k_{\text{eff}}^{(T_1)}$ and $k_{\text{eff}}^{(T_2)}$ are the effective multiplication factors obtained at two different fuel temperatures T_1 and T_2, respectively.

The Doppler reactivity coefficient is then obtained by normalizing the reactivity change to the corresponding temperature difference:

$$D_C = \frac{\Delta\rho}{\Delta T}, \tag{3.9}$$

where $\Delta T = T_2 - T_1$ is the imposed fuel temperature variation.

3.6.3 Physical Interpretation

The combined observations of Thilagam et al. [38] and Fiorito et al.[39]

indicate that:

- increasing fuel temperature broadens the resonances of the microscopic cross sections;
- this modifies the absorption and fission probabilities for neutrons in the fuel;
- the resulting variation in the effective multiplication factor is captured by the Doppler coefficient.

The Doppler coefficient thus quantifies the strength of this intrinsic and prompt negative feedback mechanism, which is a fundamental aspect of reactor physics and safety analysis.

3.7 Void Reactivity Coefficient

Besides fuel temperature effects, another key intrinsic feedback mechanism in fast reactors is associated with changes in coolant density, commonly expressed through the void reactivity

coefficient. Reactivity variations in a nuclear reactor originate not only from operator-controlled actions (such as changes in control rod position or the insertion of absorbers), but also from inherent physical effects that arise even when the system operates at constant power. These inherent effects include variations in core temperature and the formation of voids in the coolant, both of which can modify the neutron multiplication factor and disturb the neutron balance [41].

Liquid-metal fast reactors commonly employ sodium as coolant because of its favourable heat transfer characteristics. Although sodium has a high boiling point of approximately 800°C at ambient pressure, typical operating temperatures for fast reactors are around 350°C - 400°C. Under accident or abnormal conditions, however, overheating of the coolant may lead to the formation of vapour bubbles (voids). These voids modify moderation, absorption, and neutron leakage, and therefore the *void reactivity coefficient* must be evaluated with accuracy during reactor design, as it has direct implications for inherent safety [41].

3.7.1 Definition

According to the expression given in [41], the void coefficient of reactivity is defined as the reactivity introduced by replacing a fraction of the coolant volume by voids. It is expressed as:

$$\alpha_v = \frac{\Delta\rho}{x}, \tag{3.10}$$

where the void fraction is given by:

$$x = \frac{V_{\text{void}}}{V_{\text{coolant}}}. \tag{3.11}$$

where V represents the volume.

In this work, reactivity coefficients are defined in terms of reactivity ρ, while the Monte Carlo simulations provide estimates of the effective multiplication factor k_{eff}. Reactivity is therefore obtained from k_{eff} using the standard definition

$$\rho = \frac{k_{\text{eff}} - 1}{k_{\text{eff}}}. \tag{3.12}$$

All reactivity changes reported in this section are derived from the corresponding changes in k_{eff} between perturbed and reference states.

The corresponding reactivity change is:

$$\Delta\rho = \rho_{\text{void}} - \rho_0, \tag{3.13}$$

where ρ_0 is the reactivity of the unvoided system and ρ_{void} is the reactivity of the system with a void fraction x.

These equations are taken directly from the formulation presented in the INAC 2017 study [41].

3.7.2 Behaviour of the Void Coefficient in Fast Reactors

The void coefficient in a fast-spectrum reactor is strongly space-dependent [41]. Voids formed in different regions of the core may produce either a positive or a negative reactivity effect.

- **Central voids:** generally yield a *positive* reactivity effect, since neutrons retain higher energies and are more likely to cause fission.

- **Peripheral voids:** typically result in a *negative* reactivity effect, because the presence of voids in these regions increases neutron leakage from the core.

Two competing mechanisms determine the magnitude and sign of the void coefficient:

(1) Spectrum Effect Removing sodium modifies the neutron energy spectrum. The absence of coolant may:

- harden the spectrum, possibly increasing reactivity; or
- reduce moderation, lowering the reproduction factor η and contributing negatively.

(2) Leakage Effect In voided regions, neutrons do not lose energy and therefore traverse these regions more easily. This results in:

- **central voids:** increased neutron availability within the active core, producing a positive contribution to reactivity;
- **peripheral voids:** enhanced neutron escape from the core, yielding a negative contribution.

Because of these competing effects, the void coefficient in fast reactors may be positive or negative depending on the spatial distribution and magnitude of the void fraction.

3.7.3 Safety Considerations

For liquid-metal fast reactors, safety considerations require that the void reactivity coefficient be carefully assessed. Although operational systems such as control rod SCRAM are designed to shut down the reactor rapidly, safety should not rely solely on external mechanisms. Instead, the reactor should exhibit inherent stabilising feedbacks that reduce reactivity during abnormal conditions [41].

Accurate modelling of coolant void effects is therefore essential to ensure that inherent mechanisms alone can maintain the reactor in a safe state under emergency scenarios.

3.7.3.1 Branch Calculations Coupled with Depletion

The Doppler, coolant temperature, and void reactivity coefficients were evaluated using branch calculations performed in conjunction with depletion simulations. Branch calculations coupled with depletion were used to quantify the sensitivity of the system to changes in key operating and compositional parameters. At each burnup step of the reference depletion calculation, additional branch cases were executed in which selected state variables were perturbed with respect to the nominal condition. In particular, branches were defined to:

- vary the fuel temperature in order to evaluate the Doppler reactivity feedback;
- modify the coolant density to evaluate the coolant reactivity coefficient;
- introduce coolant voiding in order to evaluate the void reactivity coefficient;

For each of these branch state points, a separate criticality calculation was performed and the corresponding values of k_{eff} were obtained. The associated changes in reactivity with respect to

the nominal case were then evaluated, providing a consistent basis for analysing the impact of fuel temperature, coolant density, and coolant voiding on the reactor's neutronic behaviour.

3.8 Coupling Serpent Depletion with JANIS Cross-Section Data

To perform a rough assessment of the impact of fuel impurities on the neutronic behaviour of the selected fuel assembly, microscopic cross-section data from the OECD/NEA JANIS database were combined with the isotopic inventories obtained from the Serpent 2 depletion calculations.

JANIS (Java-based Nuclear Information Software) is a display and analysis program designed to facilitate the visualisation and manipulation of evaluated nuclear data [42]. It has been developed by the OECD Nuclear Energy Agency in collaboration with Aquitaine Electronique Informatique, as the successor of the JEF-PC software originally produced in the 1990s. Building on feedback from a large user community in the nuclear data field, JANIS provides a flexible environment for comparing different nuclear data evaluations and for extracting specific nuclear interaction data. In the present work, JANIS was used to access and process microscopic cross-section data (total, capture and fission) for the nuclides appearing in the fuel compositions and in the depleted fuel inventories.

For all nuclides present in the fresh fuel and in the depleted fuel, JANIS was used to extract energy-dependent microscopic total, capture and fission cross sections, $\sigma_{\mathrm{tot}}(E)$, $\sigma_{\gamma}(E)$ and $\sigma_{\mathrm{f}}(E)$. The data were interpolated onto a common logarithmic energy grid spanning from 10^{-1} eV to 10^{7} eV, ensuring a consistent energy discretisation for all isotopes and reaction channels. Isotope labels in the depletion output and in the JANIS datasets were brought to a common format so that, for each nuclide, the corresponding microscopic cross section could be unambiguously matched to its number density in the fuel.

From the Serpent depletion calculations, the isotope-wise atomic number densities were extracted at all burnup steps, and in particular at beginning of life (BOL) and end of life (EOL), defining the isotopic vectors of the fresh and spent fuel. By combining the number densities N_i with the microscopic cross sections from JANIS, energy-dependent macroscopic cross sections were evaluated for each reaction type r and burnup point as

$$\Sigma_r(E) = \sum_i N_i \, \sigma_{r,i}(E), \tag{3.14}$$

where $\sigma_{r,i}(E)$ denotes the microscopic cross section of isotope i for reaction r. For each isotope, macroscopic contributions were then evaluated at BOL and EOL, providing a measure of how the importance of that nuclide to the total, capture and fission cross sections evolves over the burnup cycle.

To aid interpretation, isotopes were subsequently grouped into physically meaningful families: uranium isotopes, plutonium isotopes, minor actinides (Np, Am, Cm), and all remaining nuclides. Within this last category, a distinction was made between nuclides already present at BOL (treated as impurities initially present in the fuel) and nuclides that appear only at EOL (treated as fission products generated during irradiation). For each reaction type and isotope group, the corresponding macroscopic cross section at EOL was first built as

$$\Sigma_r^{\mathrm{group}}(E) = \sum_{i \in \mathrm{group}} N_i^{\mathrm{EOL}} \, \sigma_{r,i}(E), \tag{3.15}$$

and then reduced to a single representative value by computing an energy-averaged macroscopic

cross section,

$$\left\langle \Sigma_r^{\text{group}} \right\rangle = \frac{1}{E_{\max} - E_{\min}} \int_{E_{\min}}^{E_{\max}} \Sigma_r^{\text{group}}(E)\, \mathrm{d}E, \tag{3.16}$$

with $E_{\min} = 10^{-1}\,\text{eV}$ and $E_{\max} = 10^{7}\,\text{eV}$. Although this averaging procedure does not include a neutron-flux weighting, it provides a suitable basis for a rough, comparative estimate of the relative magnitude of the contributions from uranium, plutonium, minor actinides, impurities and generated fission products to the fuel-assembly-averaged macroscopic cross sections.

The above procedure was applied to all the fuel configurations considered in this study. However, in line with the scope of the thesis, the detailed analysis and discussion in the main text are restricted to three representative cases: the MOX 80:20 fuel, the MOX+TRU 80:20 fuel, and the dedicated "fuel with impurities" case. The considerations developed for the MOX 80:20 and MOX+TRU 80:20 setups guided the structuring of this "fuel with impurities" configuration, which was defined so as to accommodate the impurity vector expected from the chemical processes discussed in this work.

Chapter 4

Results and Discussion

This chapter presents the numerical results obtained in this work and illustrates how they support the overall aim of the thesis, namely to assess the feasibility of using fuel fabricated from recycled actinides and to quantify the effect of its impurities on the neutronics of a Generation IV fast reactor system. The results are organised to provide a clear and progressive characterisation of the fuel assembly behaviour, from the reference cases to the perturbed configurations including impurities.

The figures and tables reported in this chapter are selected for their relevance in constructing a coherent and transparent argument. They document the main steps followed in assessing the impact of impurity-bearing fuel compositions derived from the CHALMEX process when implemented in a fast reactor model. In particular, the presented results highlight how the presence and composition of impurities influence key neutronic parameters and provide the basis for evaluating the behaviour of the proposed fuel compositions under fast-spectrum conditions.

All results presented in this chapter are obtained from Serpent 2 Monte Carlo depletion simulations. The numerical values and trends shown in the figures and tables were extracted from the standard Serpent output files, namely `dep.m` (post-depletion isotopic inventories), `res.m` (integral neutronic results), the `.coe` files (branch calculation results) and the `wrk` files containing the isotopic compositions used for the branch calculations. These datasets were subsequently post-processed in MATLAB to derive the burnup-dependent quantities and graphical representations discussed in the following sections.

4.1 Reference Case Results

At this stage, the geometrical configuration of interest is fixed to the fuel assembly lattice. As a first indicator of the quality of this set-up, the infinite multiplication factor k_∞ of the lattice is evaluated. The corresponding burnup-dependent results are summarised in Table 4.1.

Table 4.1: Burnup dependence of k_{eff} with Monte Carlo statistical uncertainties (1σ) for the reference case.

BU [MWd/kgHM]	$\mathbf{k}_{\text{eff}}$	$\boldsymbol{\sigma}_{\boldsymbol{k}_{\text{eff}}}$
0.00	1.20236	0.00106
0.10	1.20088	0.00049
0.50	1.19919	0.00070
1.00	1.19862	0.00109
2.00	1.19778	0.00100
3.00	1.19792	0.00070
5.00	1.19505	0.00061
7.00	1.19417	0.00114
10.00	1.19276	0.00071
15.00	1.18787	0.00053
20.00	1.18483	0.00061
25.00	1.18041	0.00125
30.00	1.17650	0.00045
35.00	1.17167	0.00084
40.00	1.16965	0.00076
45.00	1.16401	0.00098
50.00	1.16141	0.00055
55.00	1.15703	0.00067
60.00	1.15293	0.00076
65.00	1.14867	0.00068

The irradiation of the reference SPX fuel up to 65 MWd/kgU in the benchmark configuration provides an initial validation step: it shows the expected behaviour of a functioning system, reaching a criticality level clearly above unity. This demonstrates that the geometrical description, material compositions and operating conditions adopted in the model are consistent with the benchmark and that the reference configuration is well defined and unambiguous. In other words, with its own fuel the SPX set-up behaves as intended and meets the design targets.

Once the correctness of the lattice model has been established through k_∞, the global neutronic behaviour of the reference SPX configuration is analysed in terms of the effective multiplication factor k_{eff} as a function of burnup, as shown in Figure 4.1.

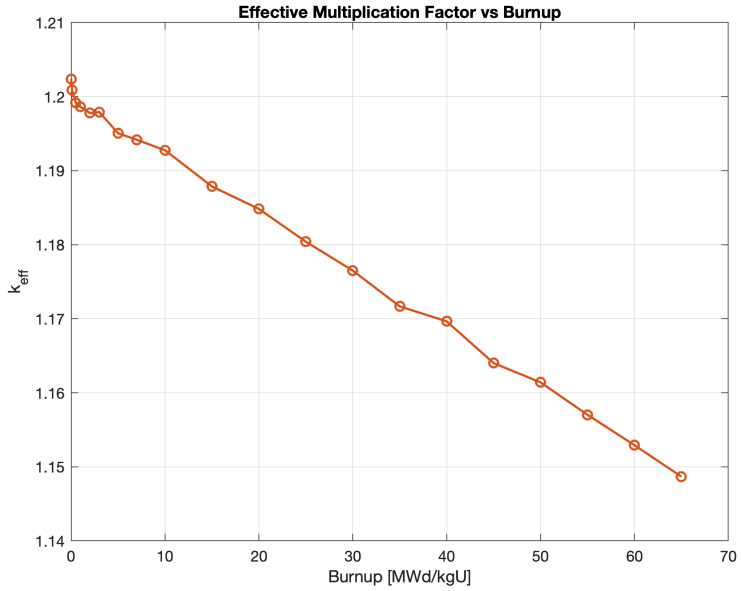

Figure 4.1: Effective Multiplication factor vs Burnup for Reference fuel

The reference model shows the expected decrease in k_{eff} with increasing burnup. At beginning of life (BU = 0 MWd/kgU) the system has a significant excess reactivity, with k_{eff} slightly above 1.20. As burnup increases up to about 65 MWd/kgU, k_{eff} gradually decreases to roughly 1.15, corresponding to a reactivity loss of about 0.055 in k_{eff}, which is relatively moderate over the investigated burnup range. The trend is almost linear, indicating a smooth and predictable reactivity evolution with no abrupt changes in neutronic behaviour, as expected for a fast reactor operating at constant power when only fuel depletion and isotopic build-up are considered, without additional control-rod or detailed thermal-hydraulic feedbacks.

From a physical point of view, the reduction in k_{eff} is mainly driven by the consumption of fissile nuclides (such as ^{239}Pu), the accumulation of fission products that act as neutron poisons, and the formation of higher actinides with less favourable fission properties. In a fast spectrum, breeding partially compensates these effects, which explains why the reactivity swing remains limited and k_{eff} stays clearly above 1.0 throughout the cycle. This behaviour confirms that the reference SPX configuration can sustain critical operation over the considered burnup range with an acceptable reactivity margin. In the rest of the chapter, this reference behaviour is used as a baseline to compare the cases using CHALMEX-derived fuel and to quantify how the presence of impurities modifies the neutronic performance of the system.

4.2 Pu-Ratio Screening and Primary fuel assessment based on kinf

As reported in Table 4.2 and shown in Figure 4.2 (left), the primary fuel composition provided by the Department of Nuclear Chemistry corresponds to a configuration that is clearly subcritical at the beginning of life and that, as irradiation progresses, exhibits an increase in k_{eff} while remaining subcritical throughout the burnup range.

This apparently counter-intuitive behaviour is explained by the fact that the SPX benchmark is a breeding fast reactor: as burnup increases, the ^{238}U in the matrix progressively transmutes into ^{239}Pu and other fissile isotopes. However, this breeding is not sufficient to raise k_{eff} to unity, and therefore the fuel never reaches a level of criticality that would make it fully performant in this setting. The main reason is that this fuel relies primarily on uranium from depleted or spent nuclear fuel, with a plutonium content of only 10%, which does not meet the SPX benchmark specifications (requiring about 16% Pu enrichment). As a consequence, this composition cannot satisfy the neutronic requirements for proper operation and had to be discarded, as the initial fissile inventory is simply too low for operation under high-flux, high-power conditions where a clearly supercritical state is expected. As reported in Table 4.3 and shown in Figure 4.2 (right), instead, we consider a fuel with 85% uranium content derived from reprocessed spent LWR fuel and an initial plutonium enrichment of 15%. At BOL this configuration exhibits a behaviour closer to that of the SPX benchmark, although its initial criticality is slightly below $k_{\text{eff}} = 1.11$. This indicates that there is enough fissile material to make the fuel operational; however, as burnup progresses, fissile isotopes are consumed while fission products and minor actinides are produced. Many of these nuclides have large neutron-absorption cross sections and either do not fission efficiently or lead to further non-fissile isotopes, effectively acting as strong neutron poisons. As a result, the evolution of k_{eff} does not fully reproduce the behaviour of the reference benchmark, even though the value at the end of the cycle remains slightly above unity. Since the aim is to design a configuration that can subsequently accommodate an additional loading of minor actinides and residual fission products—which will further reduce reactivity through additional neutron-capture reactions—this case still does not provide the reactivity margin that would be required. The results therefore indicate that, while the 85% U/15% Pu fuel is closer to feasibility than the 90% U/10% Pu case, it is not yet fully adequate as a robust reference fuel for the inner region fuel assembly in the presence of extra absorbers.

Table 4.2: Burnup dependence of k_{eff} with Monte Carlo statistical uncertainties (1σ) for the MOX fuel 90/10.

BU [MWd/kgU]	$\mathbf{k}_{\text{eff}}$	$\boldsymbol{\sigma}_{\boldsymbol{k}_{\text{eff}}}$
0.00	0.89055	0.00096
0.10	0.89010	0.00031
0.50	0.88996	0.00102
1.00	0.88977	0.00077
2.00	0.89129	0.00087
3.00	0.89427	0.00061
5.00	0.89823	0.00091
7.00	0.90164	0.00049
10.00	0.90585	0.00138
15.00	0.91446	0.00102
20.00	0.92275	0.00107
25.00	0.92832	0.00029
30.00	0.93428	0.00087
35.00	0.93948	0.00091
40.00	0.94481	0.00089
45.00	0.94893	0.00060
50.00	0.95207	0.00067
55.00	0.95491	0.00047
60.00	0.95908	0.00076
65.00	0.96089	0.00091
70.00	0.96317	0.00133
75.00	0.96287	0.00097
80.00	0.96564	0.00074
85.00	0.96696	0.00136
90.00	0.96718	0.00047

Table 4.3: Burnup dependence of k_{eff} with Monte Carlo statistical uncertainties (1σ) for the MOX fuel 85/15.

BU [MWd/kgU]	$\mathbf{k}_{\text{eff}}$	$\boldsymbol{\sigma}_{\boldsymbol{k}_{\text{eff}}}$
0.00	1.11388	0.00059
0.10	1.11108	0.00087
0.50	1.10978	0.00078
1.00	1.10929	0.00020
2.00	1.10978	0.00081
3.00	1.10926	0.00058
5.00	1.10415	0.00085
7.00	1.10263	0.00069
10.00	1.09871	0.00046
15.00	1.09284	0.00035
20.00	1.08551	0.00082
25.00	1.08212	0.00070
30.00	1.07824	0.00086
35.00	1.07408	0.00059
40.00	1.06936	0.00112
45.00	1.06461	0.00103
50.00	1.06165	0.00046
55.00	1.05755	0.00056
60.00	1.05390	0.00097
65.00	1.05042	0.00021
70.00	1.04650	0.00084
75.00	1.04269	0.00066
80.00	1.03988	0.00030
85.00	1.03574	0.00101
90.00	1.03311	0.00053

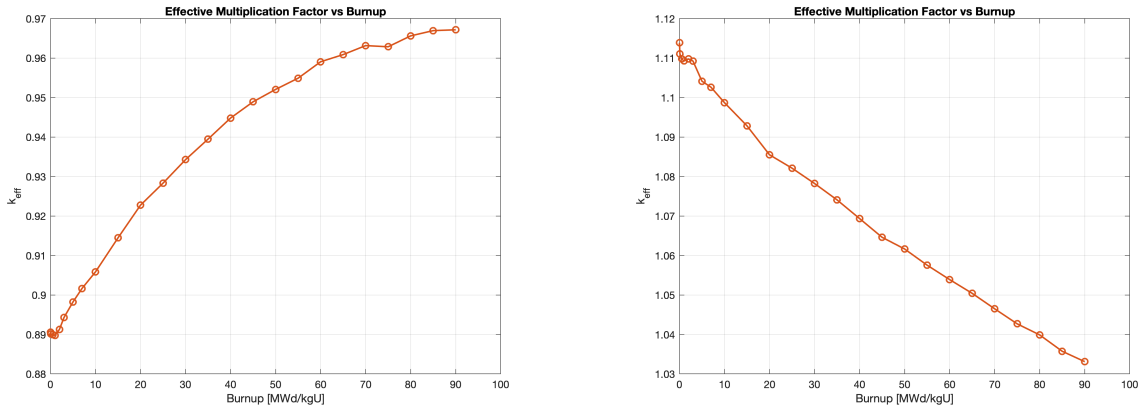

Figure 4.2: Effective Multiplication factor vs Burnup for the MOX fuel 90% Uranium 10%Plutonium (left) and 85% Uranium 15% Plutonium (right)

The burnup-dependent evolution of the effective multiplication factor for MOX fuels with increased plutonium content is reported in Tables 4.4 and 4.5 for the 80% U / 20% Pu and 75% U / 25% Pu compositions, respectively, and illustrated in Figure 4.3. For the MOX fuel with 80% uranium and 20% plutonium, the results display a behaviour that closely mirrors that of the SPX benchmark, although with a systematically higher level of criticality. The fuel configuartion starts the cycle with a high excess reactivity: at BOL k_{eff} is about 1.29 and then decreases monotonically to roughly 1.12 at 90 MWd/kgU. The almost linear trend suggests that the dynamics are mainly governed by the progressive consumption of the initial Pu inventory and by the build-up of fission products and higher actinides. From a nuclear-chemistry point of view, this evolution reflects successive neutron captures and β^- decays within the plutonium vector and the formation of americium and curium isotopes, which act as additional absorbers. Nevertheless, in this configuration the net neutron balance remains clearly favourable: from a neutronic point of view the fuel provides more than enough fissile material for the inner fuel assembly and therefore can sustain the desired fission chain while further minor actinides and fission products are introduced as impurities.

The MOX fuel with 75% uranium and 25% plutonium further amplifies this behaviour. In this case the initial value of k_{eff} is significantly larger than that of the SPX reference case, indicating a very high fissile loading. Such a composition would, in principle, be able to accommodate the full sequence of fuel transformations considered in this work: the introduction of minor actinides and pre-existing fission products, together with the additional fission products generated during irradiation. From a purely neutronic perspective, the large reactivity margin would ensure that the system remains comfortably supercritical even in the presence of strong absorbers, and the fast spectrum would promote transmutation of several minor actinides.

However, when the results are examined from a safety and reactor-physics standpoint, important drawbacks emerge. The high Pu content in the 75% U/25% Pu MOX leads to a very large excess of reactivity at BOL and a strong reactivity loss with burnup. This would require substantial control action (e.g. deep control-rod insertion and/or strong burnable poisons) to keep the reactor close to criticality and within acceptable safety margins. The combination of very high initial k_{eff}, pronounced burnup reactivity swing, and deviation from the original SPX design specifications makes this composition unfavourable from the viewpoints of control, operational flexibility and safety, even though it is neutronically feasible.

In summary, increasing the Pu content from 15% to 20% and 25% does provide a large reactivity margin that is, in principle, sufficient to host additional absorbers such as impurities, minor actinides and residual fission products while maintaining a behaviour broadly consistent with that of the SPX inner zone studied in the simulations. Nonetheless, the 80% U/20% Pu fuel offers a more balanced compromise between reactivity margin and controllability.

Table 4.4: Burnup dependence of k_{eff} with Monte Carlo statistical uncertainties (1σ) for MOX fuel 80/20.

BU [MWd/kgU]	$\mathbf{k}_{\text{eff}}$	$\boldsymbol{\sigma}_{\boldsymbol{k}_{\text{eff}}}$
0.00	1.29444	0.00078
0.10	1.29408	0.00028
0.50	1.29150	0.00031
1.00	1.29011	0.00078
2.00	1.28669	0.00078
3.00	1.28484	0.00056
5.00	1.28083	0.00128
7.00	1.27644	0.00100
10.00	1.26793	0.00050
15.00	1.25689	0.00092
20.00	1.24471	0.00017
25.00	1.23317	0.00089
30.00	1.22483	0.00114
35.00	1.21502	0.00085
40.00	1.20363	0.00039
45.00	1.19384	0.00036
50.00	1.18481	0.00073
55.00	1.17700	0.00144
60.00	1.16903	0.00099
65.00	1.16057	0.00038
70.00	1.15249	0.00075
75.00	1.14221	0.00070
80.00	1.13631	0.00034
85.00	1.12734	0.00126
90.00	1.12019	0.00121

Table 4.5: Burnup dependence of k_{eff} with Monte Carlo statistical uncertainties (1σ) for MOX fuel 75/25.

BU [MWd/kgU]	$\mathbf{k}_{\text{eff}}$	$\boldsymbol{\sigma}_{\boldsymbol{k}_{\text{eff}}}$
0.00	1.45028	0.00061
0.10	1.44968	0.00133
0.50	1.44620	0.00036
1.00	1.44715	0.00057
2.00	1.44290	0.00070
3.00	1.43958	0.00114
5.00	1.43590	0.00061
7.00	1.42823	0.00087
10.00	1.42071	0.00085
15.00	1.40813	0.00057
20.00	1.39408	0.00127
25.00	1.37884	0.00074
30.00	1.36577	0.00066
35.00	1.35349	0.00083
40.00	1.34042	0.00100
45.00	1.32768	0.00137
50.00	1.31538	0.00062
55.00	1.30360	0.00081
60.00	1.29068	0.00099
65.00	1.28221	0.00076
70.00	1.26783	0.00066
75.00	1.25517	0.00051
80.00	1.24583	0.00060
85.00	1.23472	0.00062
90.00	1.22301	0.00110

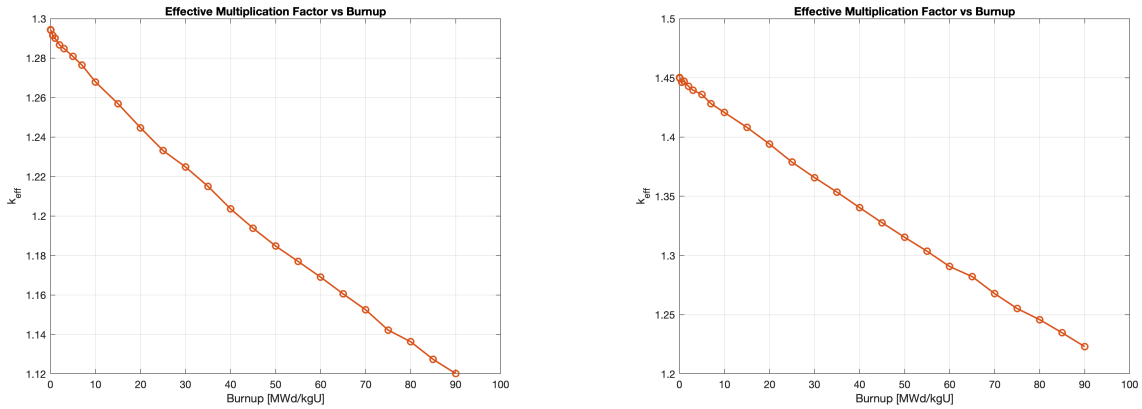

Figure 4.3: Effective Multiplication factor vs Burnup for the fabbricated MOX fuel 80% Uranium 20%Plutonium (left) and 75% Uranium 25% Plutonium (right)

4.3 Effect of TRU Loading

The effect of introducing minor actinides into the MOX fuel compositions on the burnup-dependent evolution of the effective multiplication factor is summarised in Tables 4.6 and 4.7 and illustrated in Figures 4.4 and 4.5. These results allow a direct comparison between the reference MOX fuels and their corresponding TRU-bearing configurations across the full burnup range. The results obtained after the introduction of minor actinides into the fuel composition show, for all four fuel configurations, a behaviour that is very similar to that of the corresponding MOX fuels without minor actinides in terms of k_{eff}. The k_{eff} curves with minor actinides are slightly lower than their reference MOX counterparts, with differences on the order of a few hundred pcm over the whole burnup range. The overall evolution of criticality is therefore preserved, and the analysis confirms the previous conclusions: MOX 80/20 and MOX 85/15 remain the most suitable candidates for hosting additional absorbers, as they provide an adequate reactivity margin while maintaining a behaviour close to that of the SPX benchmark.

The observed downward shift of the curves can be interpreted in light of the neutronic role of the loaded minor actinides. The introduction of minor actinides at BOL mainly acts as an additional absorption term, since nuclides such as ^{237}Np, ^{241}Am and ^{244}Cm exhibit large capture cross sections and comparatively unfavourable fission probabilities. As irradiation proceeds in a fast spectrum, part of this inventory is burned by fission and part is transformed through successive neutron captures and β^- decays into heavier isotopes with a more favourable fission-to-capture ratio. Consequently, while minor actinides still introduce a reactivity penalty, their impact on k_{eff} over the cycle remains moderate rather than dominant [43–45]. On the basis of these results, the fuel configuration selected to host the impurities, due to its close mirroring of the SPX benchmark behaviour, is the MOX 80/20 composition and, in the subsequent step, the corresponding MOX with TRU 80/20 fuel.

Table 4.6: Burnup dependence of k_{eff} with Monte Carlo statistical uncertainties (1σ) for the MOX with TRU fuel 90/10.

BU [MWd/kgU]	$\mathbf{k}_{\text{eff}}$	$\boldsymbol{\sigma}_{\boldsymbol{k}_{\text{eff}}}$
0.00	0.88636	0.00027
0.10	0.88578	0.00023
0.50	0.88659	0.00030
1.00	0.88679	0.00030
2.00	0.88878	0.00009
3.00	0.89129	0.00019
5.00	0.89565	0.00041
7.00	0.89950	0.00038
10.00	0.90501	0.00017
15.00	0.91411	0.00041
20.00	0.92144	0.00018
25.00	0.92843	0.00030
30.00	0.93397	0.00049
35.00	0.93960	0.00030
40.00	0.94491	0.00045
45.00	0.94932	0.00015
50.00	0.95312	0.00012
55.00	0.95639	0.00009
60.00	0.95952	0.00025
65.00	0.96243	0.00019
70.00	0.96412	0.00028
75.00	0.96598	0.00033
80.00	0.96809	0.00048
85.00	0.96969	0.00017
90.00	0.97042	0.00043

Table 4.7: Burnup dependence of k_{eff} with Monte Carlo statistical uncertainties (1σ) for the MOX with TRU fuel 85/15.

BU [MWd/kgU]	$\mathbf{k}_{\text{eff}}$	$\boldsymbol{\sigma}_{\boldsymbol{k}_{\text{eff}}}$
0.00	1.10960	0.00021
0.10	1.10916	0.00024
0.50	1.10931	0.00036
1.00	1.10799	0.00040
2.00	1.10746	0.00021
3.00	1.10577	0.00032
5.00	1.10361	0.00048
7.00	1.10095	0.00017
10.00	1.09809	0.00034
15.00	1.09299	0.00013
20.00	1.08754	0.00021
25.00	1.08329	0.00008
30.00	1.07880	0.00034
35.00	1.07467	0.00017
40.00	1.07045	0.00015
45.00	1.06637	0.00031
50.00	1.06268	0.00025
55.00	1.05926	0.00033
60.00	1.05537	0.00021
65.00	1.05185	0.00038
70.00	1.04903	0.00016
75.00	1.04602	0.00041
80.00	1.04208	0.00022
85.00	1.03958	0.00018
90.00	1.03690	0.00020

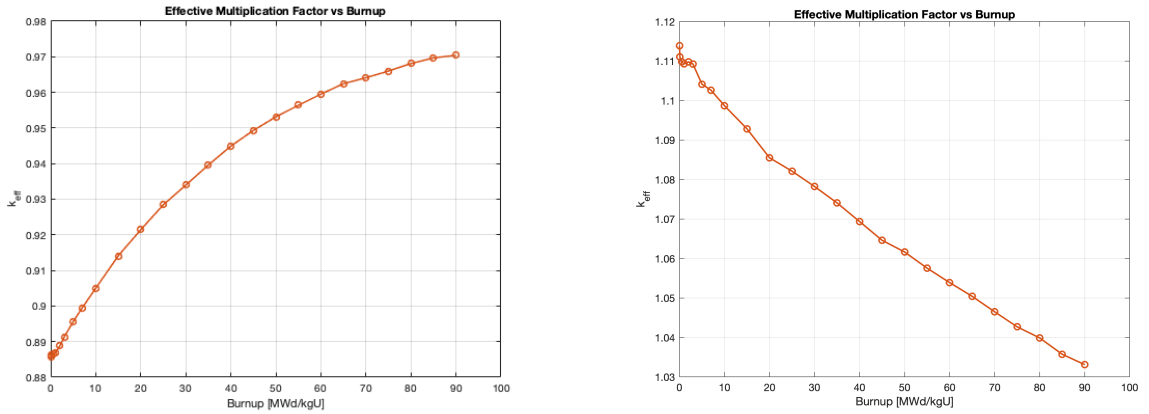

Figure 4.4: Effective Multiplication factor vs Burnup for the MOX with TRU fuel 90% Uranium 10% Plutonium (left) and 85% Uranium 15% Plutonium (right)

Table 4.8: Burnup dependence of k_{eff} with Monte Carlo statistical uncertainties (1σ) for the MOX with TRU fuel 80/20.

BU [MWd/kgU]	$\mathbf{k}_{\text{eff}}$	$\boldsymbol{\sigma}_{\boldsymbol{k}_{\text{eff}}}$
0.00	1.28932	0.00015
0.10	1.29001	0.00021
0.50	1.28991	0.00026
1.00	1.28825	0.00035
2.00	1.28490	0.00030
3.00	1.28293	0.00027
5.00	1.27826	0.00021
7.00	1.27428	0.00030
10.00	1.26791	0.00035
15.00	1.25591	0.00022
20.00	1.24571	0.00014
25.00	1.23542	0.00027
30.00	1.22478	0.00032
35.00	1.21484	0.00019
40.00	1.20589	0.000033
45.00	1.19592	0.000035
50.00	1.18631	0.00022
55.00	1.17861	0.00023
60.00	1.16983	0.00016
65.00	1.16218	0.00025
70.00	1.15421	0.00010
75.00	1.14675	0.00012
80.00	1.13895	0.00024
85.00	1.13168	0.00037
90.00	1.12450	0.00017

Table 4.9: Burnup dependence of k_{eff} with Monte Carlo statistical uncertainties (1σ) for the MOX with TRU fuel 75/25.

BU [MWd/kgU]	$\mathbf{k}_{\text{eff}}$	$\boldsymbol{\sigma}_{\boldsymbol{k}_{\text{eff}}}$
0.00	1.44474	0.00024
0.10	1.44483	0.00034
0.50	1.44423	0.00010
1.00	1.44261	0.00025
2.00	1.44018	0.00030
3.00	1.43756	0.00038
5.00	1.43210	0.00040
7.00	1.42622	0.00022
10.00	1.41900	0.00017
15.00	1.40504	0.00032
20.00	1.39212	0.00030
25.00	1.37859	0.00024
30.00	1.36638	0.00023
35.00	1.35361	0.00045
40.00	1.34055	0.00026
45.00	1.32834	0.00025
50.00	1.31698	0.00009
55.00	1.30472	0.00033
60.00	1.29359	0.00022
65.00	1.28243	0.00052
70.00	1.27065	0.00012
75.00	1.26025	0.00026
80.00	1.25008	0.00035
85.00	1.23920	0.00028
90.00	1.22845	0.00020

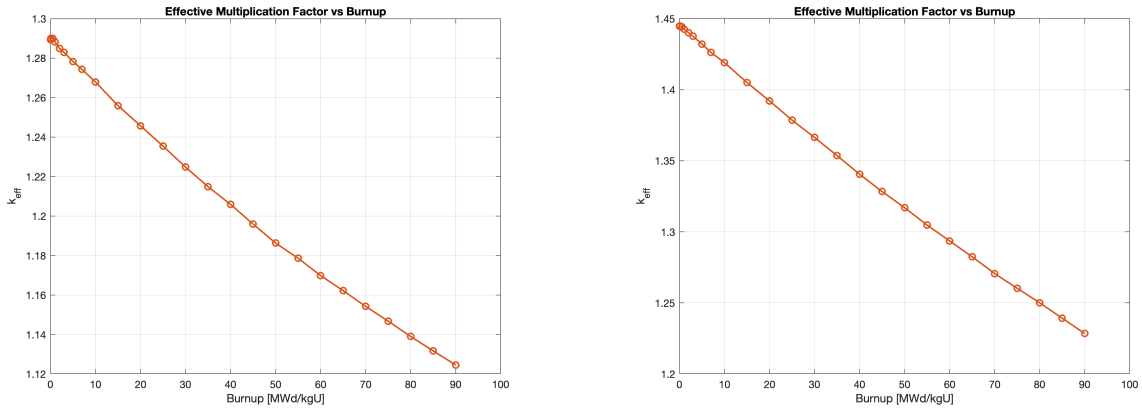

Figure 4.5: Effective Multiplication factor vs Burnup for the MOX with TRU fuel 80% Uranium 20% Plutonium (left) and 75% Uranium 25% Plutonium (right)

4.4 Impurity Effects

The impact of introducing impurities into the MOX 80/20 fuel on the burnup-dependent evolution of the effective multiplication factor is reported in Table 4.10 and illustrated in Figure 4.6. The introduction of impurities into the MOX 80/20 fuel leads to a clear decrease in the k_{eff} value compared to the corresponding MOX 80/20 case without impurities. At BOL, k_{eff} is reduced from 1.28932 to 1.21116, corresponding to $\Delta k \approx 0.078$ (about 7800 pcm). From the point of view of criticality, however, the overall behaviour remains very close to that of the SPX reference benchmark: the system starts in a clearly supercritical state and then gradually approaches unity as burnup increases, which is the expected trend for the reference SPX configuration under investigation. These results support the modelling assumptions adopted for the "fuel with impurities" configuration and indicate that the fuel still achieves proper neutronic performance in the given geometry. The overall shape of the k_{eff} curve is essentially unchanged, showing that the fundamental burnup behaviour of the fuel is preserved.

The observed reactivity loss is consistent with the neutronic role of the impurities, which mainly consist of residual fission-product elements (such as rare earths) and neutron absorbers inherited from the CHALMEX separation process. At BOL these nuclides act predominantly as parasitic absorbers: they capture neutrons without contributing significantly to fission, thereby lowering the multiplication factor. As irradiation proceeds, their relative importance is partially mitigated by further transmutation and by the increasing total fission-product inventory, so that the additional penalty on k_{eff} remains moderate rather than dominant. From a design perspective, the "fuel with impurities" configuration still satisfies the basic neutronic feasibility criteria: the system remains supercritical over the whole burnup range, while the initial excess reactivity and the reactivity swing move closer to those of the SPX benchmark fuel. This confirms that the MOX 80/20–based TRU fuel can act as a realistic host matrix for both minor actinides and the expected impurity vector from the CHALMEX process, without compromising the overall neutronic behaviour, in agreement with the general understanding that residual fission-product and rare-earth impurities introduce a measurable but manageable negative reactivity effect through their strong neutron-absorption cross sections [46–48].

Table 4.10: Burnup dependence of k_{eff} with Monte Carlo statistical uncertainties (1σ) for the fuel with impurities.

BU [MWd/kgU]	$\mathbf{k}_{\text{eff}}$	$\boldsymbol{\sigma}_{\boldsymbol{k}_{\text{eff}}}$
0.00	1.21116	0.00035
0.10	1.21075	0.00039
0.50	1.21073	0.00029
1.00	1.20964	0.00031
2.00	1.20790	0.00032
3.00	1.20551	0.00046
5.00	1.20126	0.00026
7.00	1.19771	0.00059
10.00	1.19128	0.00045
15.00	1.18111	0.00029
20.00	1.17206	0.00042
25.00	1.16386	0.00024
30.00	1.15535	0.00029
35.00	1.14693	0.00051
40.00	1.13840	0.00024
45.00	1.13157	0.00023
50.00	1.12307	0.00023
55.00	1.11601	0.00036
60.00	1.10935	0.00024
65.00	1.10246	0.00032

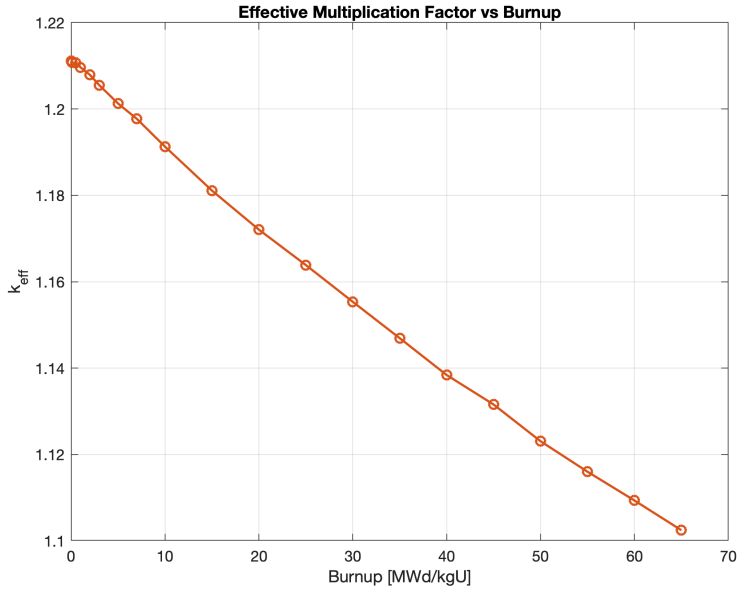

Figure 4.6: Effective Multiplication factor vs Burnup for the fuel with impurities

4.5 Cross-Section Perspective (JANIS)

4.5.1 Grouped-averaged Total macroscopic cross sections

The group-averaged total macroscopic cross sections for the different fuel configurations are reported in Tables 4.11 and 4.12 at beginning of life (BOL) and end of life (EOL), respectively. These data allow a systematic comparison of the relative contributions of uranium, plutonium, minor actinides, and fission products, and provide a macroscopic interpretation of the reactivity trends observed in the preceding sections.

Table 4.11: Group-averaged macroscopic total cross section at BOL (BU ≈ 0 MWd/kgHM).

Case	Σ_U	Σ_{Pu}	Σ_{MA}	Σ_{FP}
		[1/cm]		
REFERENCE CASE	1.5191e-01	2.6405e-02	3.6564e-04	0.0000e+00
MOX FUEL-80_20	1.1733e-01	2.9056e-02	0.0000e+00	0.0000e+00
MOX/TRU-80_20	1.1733e-01	2.9056e-02	7.4617e-04	0.0000e+00
FUEL WITH IMPURITIES	1.1784e-01	2.6089e-02	7.5637e-04	5.2089e-05

Table 4.12: Group-averaged macroscopic total cross section at EOL (BU ≈ 65 MWd/kgHM).

Case	Σ_U	Σ_{Pu}	Σ_{MA}	Σ_{FP}
		[1/cm]		
REFERENCE CASE	1.3900e-01	2.7259e-02	5.1169e-04	3.5847e-03
MOX FUEL-80_20	1.0862e-01	2.7569e-02	4.5436e-04	2.9390e-03
MOX/TRU-80_20	1.0868e-01	2.7688e-02	9.7429e-04	2.9559e-03
FUEL WITH IMPURITIES	1.0855e-01	2.5580e-02	9.2785e-04	2.9603e-03

The analysis of the group-averaged total macroscopic cross sections at BOL and EOL highlights the different roles of the various nuclide families in each fuel configuration. At BOL, the reference SPX fuel is dominated by the uranium and plutonium contributions, while the minor-actinide term Σ_{MA} is very small. This non-zero Σ_{MA} originates from the presence of ^{241}Am in the benchmark composition, which is classified here as a minor actinide. In the MOX-80/20 fuel, the plutonium contribution Σ_{Pu} is larger than in the reference case, reflecting the higher Pu content (20% instead of the benchmark value), whereas Σ_{MA} and Σ_{FP} are zero by construction. In the MOX/TRU-80/20 and "fuel with impurities" cases, Σ_{MA} becomes non-zero due to the explicit loading of minor actinides, and in the impurities case a small but finite Σ_{FP} term appears at BOL, corresponding to the initial impurity vector from the CHALMEX process. In other words, only those fuels that are defined with minor actinides and/or impurities show non-zero Σ_{MA} and Σ_{FP} at the beginning of life.

At EOL, the total macroscopic cross sections exhibit the expected burnup trends. For all cases, the uranium contribution Σ_U decreases due to fuel depletion, while Σ_{Pu} increases compared to BOL in the reference case, in line with the breeding nature of the fast spectrum, which converts part of ^{238}U into fissile plutonium isotopes whereas it decreases in the MOX-based fuels as the depletion of the initially loaded plutonium outweighs the net production over the irradiation history considered. The minor-actinide term Σ_{MA} clearly grows in all configurations, since MAs

are produced primarily through neutron captures in Pu. The fission-product term Σ_{FP} also increases strongly between BOL and EOL for every fuel; in the reference fuel it represents only fission products generated during irradiation, whereas in the impurity fuel it combines the initial impurity inventory and the additional fission products created during burnup. The growth of Σ_{MA} and Σ_{FP} with burnup quantifies the appearance of new absorber isotopes in the system and explains the loss of reactivity discussed in the previous sections. In the impurities case, Σ_{Pu} is slightly lower than in the corresponding TRU-80/20 fuel (some Pu has been replaced by impurities), yet the total Σ_{FP} at EOL is very similar to the other MOX-based fuels. This is consistent with the picture that the combination "fission products + impurities" behaves as a single absorber family whose overall strength is mainly governed by the achieved burnup.

4.5.2 Grouped-averaged capture macroscopic cross sections

The group-averaged macroscopic capture cross sections for the different fuel configurations are reported in Tables 4.13 and 4.14 at beginning of life (BOL) and end of life (EOL), respectively.

Table 4.13: Group-averaged macroscopic capture cross section at BOL (BU ≈ 0 MWd/kgHM).

Case	Σ_U	Σ_{Pu}	Σ_{MA}	Σ_{FP}
		[1/cm]		
REFERENCE CASE	5.9192e-04	1.9907e-04	6.3794e-06	0.0000e+00
MOX FUEL-80_20	4.5649e-04	3.6959e-04	0.0000e+00	0.0000e+00
MOX/TRU-80_20	4.5649e-04	3.6959e-04	8.8310e-06	0.0000e+00
FUEL WITH IMPURITIES	4.5845e-04	3.3125e-04	8.8978e-06	1.6162e-07

Table 4.14: Group-averaged macroscopic capture cross section at EOL (BU ≈ 65 MWd/kgHM).

Case	Σ_U	Σ_{Pu}	Σ_{MA}	Σ_{FP}
		[1/cm]		
REFERENCE CASE	5.4128e-04	2.2090e-04	7.3568e-06	1.5437e-05
MOX FUEL-80_20	4.2256e-04	3.8744e-04	6.4016e-06	1.3108e-05
MOX/TRU-80_20	4.2280e-04	3.8883e-04	1.2146e-05	1.3027e-05
FUEL WITH IMPURITIES	4.2227e-04	3.5195e-04	1.1405e-05	1.3447e-05

Looking specifically at the capture macroscopic cross sections, the situation at BOL is again dominated by uranium and plutonium for the reference and MOX-80/20 fuels. In the MOX/TRU-80/20 fuel there is already a small capture contribution from the loaded minor actinides, and in the impurities fuel an additional capture term appears due to the initial impurity vector. As burnup progresses, Table 4.4 shows that a significant capture contribution from fission products emerges in all fuel types, with Σ_{FP} reaching values of the order of 1.3–$1.5 \times 10^{-5}\,\mathrm{cm}^{-1}$, comparable to or even larger than the MA capture term. The MA capture components approximately double between BOL and EOL in the TRU and impurities cases, reflecting the build-up of minor actinides, while the U and Pu capture contributions change only modestly.

These trends make it clear that the main new absorbers appearing with burnup are fission products and minor actinides. In the the fuel with impurities, an FP-type capture term is already present at BOL and grows further at EOL. This behaviour provides the microscopic explanation for the negative reactivity effect previously observed in the evolution of k_{eff}: as additional FP and MA absorbers accumulate, the capture probability in the fuel increases and the multiplication factor is progressively reduced.

4.5.3 Grouped-averaged fission macroscopic cross sections

For the fission macroscopic cross sections, the contributions are dominated by uranium and plutonium for all fuel configurations, as reported in Table 4.15 at beginning of life (BOL).

Table 4.15: Group-averaged macroscopic fission cross section at BOL (BU $\approx$ 0 MWd/kgHM).

Case	Σ_U	Σ_{Pu}	Σ_{MA}	Σ_{FP}
		[1/cm]		
REFERENCE CASE	1.3296e-02	6.7836e-03	9.3476e-05	0.0000e+00
MOX FUEL-80_20	1.0224e-02	7.3398e-03	0.0000e+00	0.0000e+00
MOX/TRU-80_20	1.0224e-02	7.3399e-03	1.7915e-04	0.0000e+00
FUEL WITH IMPURITIES	1.0267e-02	6.5915e-03	1.8052e-04	0.0000e+00

At end of life (EOL), the fission macroscopic cross sections reported in Table 4.16 exhibit distinct trends among the different fuel types.

Table 4.16: Group-averaged macroscopic fission cross section at EOL (BU $\approx$ 65 MWd/kgHM).

Case	Σ_U	Σ_{Pu}	Σ_{MA}	Σ_{FP}
		[1/cm]		
REFERENCE CASE	1.2139e-02	6.9815e-03	1.2463e-04	0.0000e+00
MOX FUEL-80_20	9.4609e-03	6.9578e-03	1.0925e-04	0.0000e+00
MOX/TRU-80_20	9.4662e-03	6.9945e-03	2.4089e-04	0.0000e+00
FUEL WITH IMPURITIES	9.4542e-03	6.4704e-03	2.2889e-04	0.0000e+00

For the fission macroscopic cross sections, all fuels are dominated by the uranium and plutonium contributions. In the reference case, the MA fission term $\Sigma_{\mathrm{MA},f}$ is very small but non-zero at BOL because of the initial ^{241}Am. In the TRU-80/20 and impurities fuels, $\Sigma_{\mathrm{MA},f}$ is larger, since the loaded minor actinides have non-negligible fission probabilities in the fast spectrum and thus contribute slightly to the total fission rate.

At EOL, the uranium fission term $\Sigma_{U,f}$ increases in the reference case, consistent with a harder neutron spectrum and an enhanced role of fast fission in ^{238}U. In the other MOX-based fuels, $\Sigma_{U,f}$ shows a slight decrease due to the net depletion of fissile uranium isotopes, while $\Sigma_{\mathrm{MA},f}$ becomes larger in the TRU and impurities cases, indicating that some of the built-up minor actinides are now actively participating in fission. No fission-product contribution appears in the fission cross-section tables because fission products are generally medium-mass nuclei and their neutron-induced fission probability is negligible in the considered energy range; consequently, they primarily act as absorbers through capture (and therefore affect the total) rather than contributing to fission. As a result, the negative reactivity impact associated with impurities and fission products arises mainly from their capture (and total) macroscopic cross sections, rather than from competition with U and Pu in the fission channel.

4.5.4 Macroscopic and microscopic cross sections for total, capture, and fission reaction types

4.5.4.1 Fuel with Impurities: Total Reaction

The plot of the overall macroscopic total cross section shown in Figure 4.7 (left), indicates that the interaction probability in the fuel is governed by uranium and plutonium over the entire energy range from 10^{-1} eV to 10^{7} eV. In the fast region (roughly $E \gtrsim 10^{5}$ eV), the "all species" curve almost coincides with the sum of the U and Pu curves, while the macroscopic contributions from minor actinides and fission products lie about one to two orders of magnitude below. This indicates that, on a macroscopic level, neutron interactions are still dominated by U and Pu isotopes even at end of life, in agreement with the trends already identified in the group-averaged cross-section tables.

The corresponding microscopic total cross-section plot shown in Figure 4.7 (right), however, reveals the opposite hierarchy on a per-nucleus basis: minor actinides and fission products exhibit very large microscopic total cross sections, typically in the range 10^{4}–10^{5} barn, whereas the uranium and plutonium isotopes show significantly smaller microscopic values. Therefore, the combined interpretation of the two plots is that fission products and minor-actinide nuclides, although present at relatively low number densities and thus contributing less on a macroscopic level, behave as strong poisons. Their very large microscopic cross sections make the fuel less efficient, leading to the reduction in k_{eff} discussed earlier. The increase of their contribution towards end of life clearly indicates that they play a key role as additional absorbers in the system.

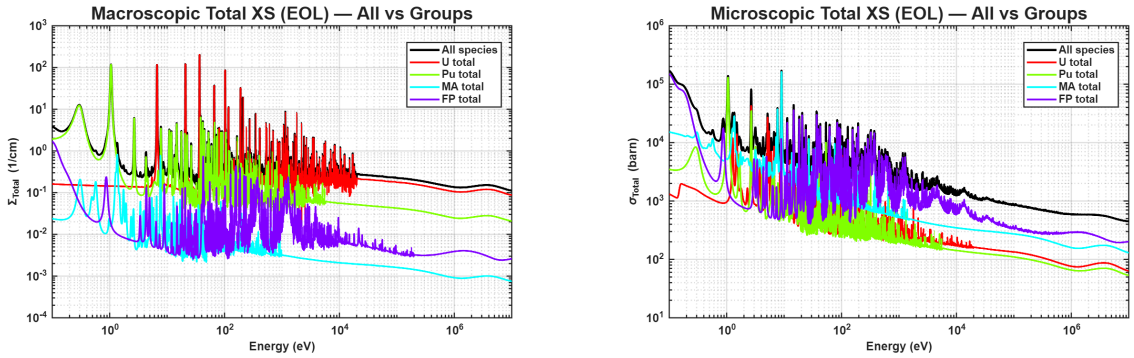

Figure 4.7: Macroscopic (Σ_t) and microscopic (σ_t) total cross sections at EOL, shown for all isotopes and for the grouped contributions of U, Pu, MA, and FP.

The uranium-only plots resolve the contributions of the individual U isotopes. In the macroscopic total cross-section plot shown on the left in Figure 4.8 it is apparent that the dominant contributor is ^{238}U: its curve essentially coincides with the U–total curve and lies about two to three orders of magnitude above those of the fissile isotopes ^{235}U and ^{233}U. Smaller but non-negligible contributions arise from ^{236}U, ^{237}U and ^{234}U at lower levels. Overall, this behaviour indicates that, in a fast spectrum and even after significant burnup, the fuel still contains a large inventory of fertile ^{238}U, which remains the primary material with which neutrons interact, both through scattering and neutron capture [49, 50].

On a microscopic level, as shown on the right in Figure 4.8, focusing on the most relevant uranium isotopes from the epithermal to the fast range, ^{238}U again retains the largest influence. At high energies the microscopic curves for the various uranium isotopes tend to converge, as expected.

These features are consistent with standard uranium cross-section behaviour and confirm that, at EOL, the spectrum seen by the uranium isotopes is predominantly fast, with only a residual contribution from lower-energy neutrons.

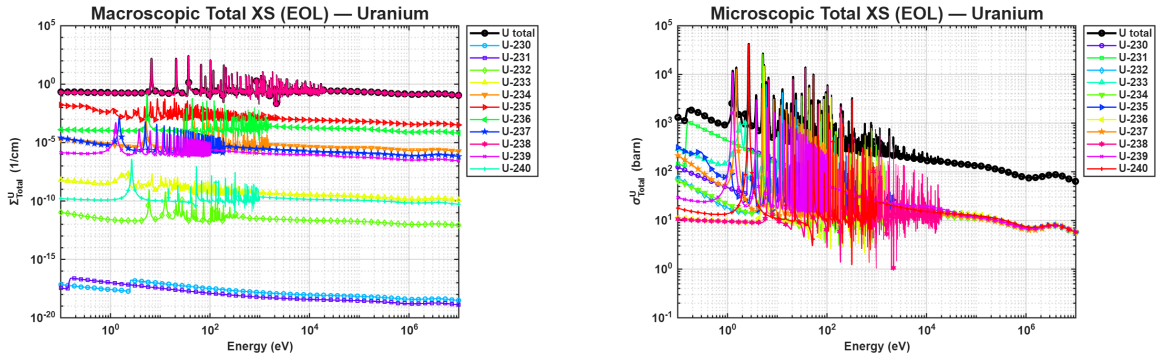

Figure 4.8: Macroscopic (Σ_t) and microscopic (σ_t) total cross sections at EOL for the uranium isotopes (U).

The plutonium macroscopic and microscopic total cross-section plot shown in Figure 4.9 indicates that, among the Pu isotopes, ^{239}Pu, ^{240}Pu and ^{241}Pu are the main contributors at EOL. Their curves lie close to the total Pu curve, whereas higher-mass isotopes such as ^{242}Pu and ^{243}Pu contribute at lower levels, reflecting both their smaller concentrations and, in some cases, less favourable cross sections. The presence of several non-negligible Pu isotopes is consistent with the breeding and conversion processes occurring in a fast reactor, where neutron captures in ^{239}Pu and ^{240}Pu gradually populate the heavier isotopes.

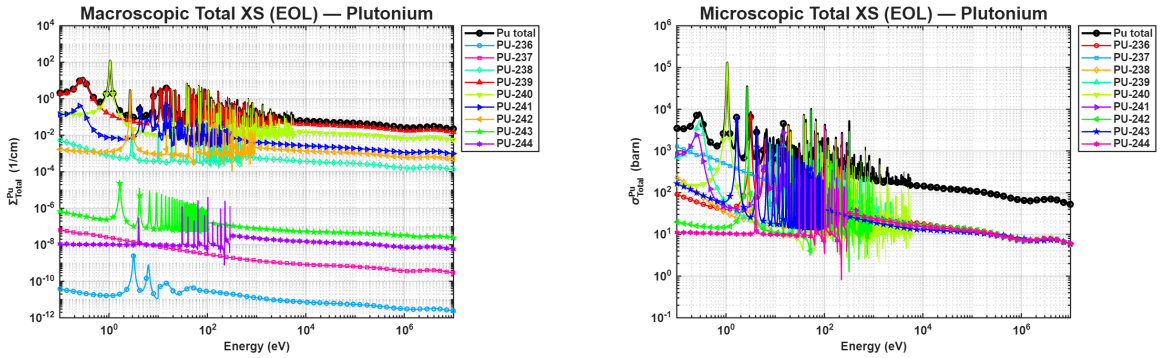

Figure 4.9: Macroscopic (Σ_t) and microscopic (σ_t) total cross sections at EOL for the plutonium isotopes (Pu).

The macroscopic total cross sections of the minor actinides at EOL shown on the left in Figure 4.10, remain one to several orders of magnitude below those of U and Pu. This indicates that their relatively low number densities limit their overall contribution at the material level: even at the end of life, the bulk interaction probability in the fuel is still dominated by uranium and plutonium. Nevertheless, the macroscopic MA total is clearly non-zero and is dominated by a subset of isotopes (mainly several Am and Cm nuclides), which therefore drive the MA contribution to the overall reaction rates.

The corresponding microscopic total cross sections for the minor actinides shown on the right in Figure 4.10 reveal a very different hierarchy on a per-nucleus basis. Many Am, Cm and Np isotopes exhibit extremely large microscopic total cross sections, of the order of 10^2–10^4 barn at low and intermediate energies, and still tens to hundreds of barns in the fast region. This combination of low concentration but very large microscopic cross sections explains why minor actinides behave as strong neutron absorbers: a relatively small MA inventory is sufficient to introduce a noticeable additional interaction probability. Taken together, the macroscopic and microscopic plots clarify that, while minor actinides do not dominate the overall material cross section, they act as efficient poisons and are responsible for a significant part of the reactivity penalty observed in the depletion calculations.

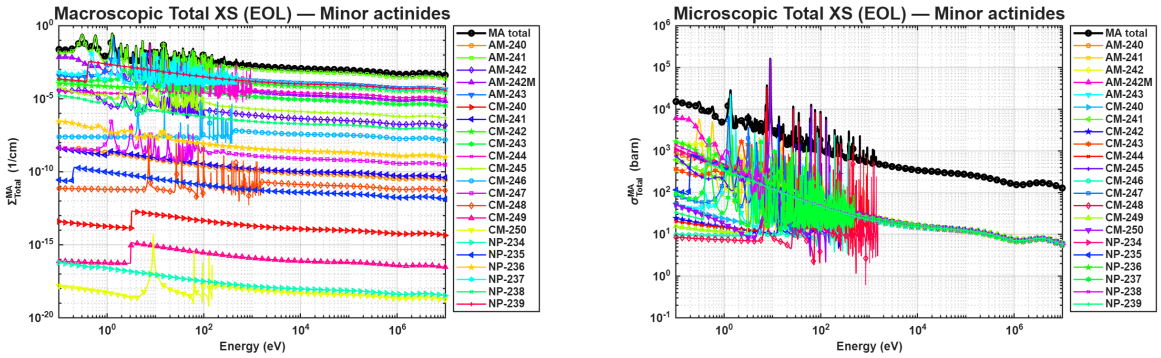

Figure 4.10: Macroscopic (Σ_t) and microscopic (σ_t) total cross sections at EOL for the minor actinide isotopes (MA).

The effect of the impurities can be clearly observed from the behaviour of the fission products in both the macroscopic and microscopic total cross-section plots which are illustrated in Figur 4.11. In macroscopic form, the FP–total curve lies in the range of about 10^{-3}–$10^{-2}\,\mathrm{cm}^{-1}$ over most of the fast-energy domain. As for the minor actinides, this indicates that fission products provide a clearly non-negligible contribution to the total cross section. Only a subset of fission products, mainly lanthanides and rare-earth elements, are actually relevant at this level. In particular, neodymium and samarium have curves that closely follow the FP–total curve, identifying them as the main contributors to the FP macroscopic term, while the remaining isotopes lie at significantly lower levels.

The microscopic total cross-section plot explains why these nuclides are so effective. Many fission products exhibit extremely large microscopic total cross sections, of the order of 10^3–10^5 barn in the thermal and epithermal range, and still several tens of barns in the fast region. Thus, even though their number densities are only moderate, each individual FP nucleus is a very efficient absorber. The combination of a significant macroscopic FP–total level and very large microscopic cross sections clarifies why the build-up of fission products towards end of life introduces a strong additional absorption term and contributes markedly to the observed decrease in k_{eff}.

Lanthanide fission products, in particular samarium and neodymium, are well-known neutron poisons due to their high neutron-capture cross sections and their accumulation in spent fuel. In reactor physics, ^{149}Sm is often identified as the second most important long-lived fission-product poison after ^{135}Xe [51–53], which is fully consistent with the dominant role of samarium and neodymium observed in the present cross-section analysis.

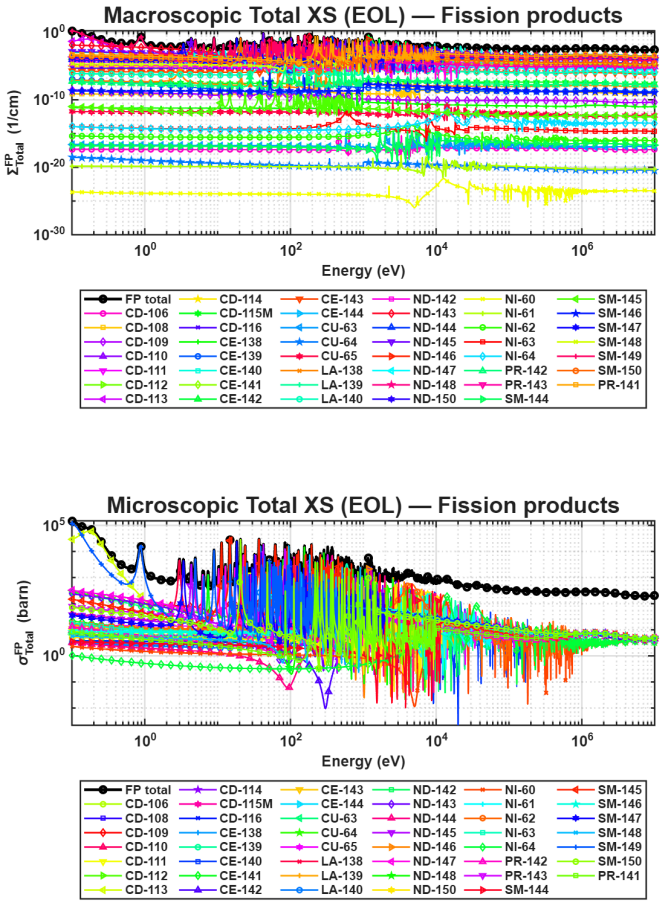

Figure 4.11: Macroscopic (Σ_t) and microscopic (σ_t) total cross sections at EOL for the fission product isotopes (FP).

4.5.4.2 Fuel with impurities: Capture Reaction

The macroscopic and microscopic capture cross sections of uranium, plutonium, minor actinides, and fission products at end of life are illustrated in Figures 4.12–4.16, providing a comprehensive characterisation of the capture reaction across the different nuclide families.

On the macroscopic level, uranium and plutonium isotopes dominate the capture reaction. In particular, U-238 leads distinctly: its macroscopic capture curve essentially overlaps with the total-uranium line and exceeds the contributions of U-235, U-233 and the minor uranium isotopes by 2–3 orders of magnitude across most of the fast-energy spectrum. Smaller but still visible contributions arise from U-235, U-236, U-237 and U-234, especially at the lower end of the fast range. This behaviour reflects the large residual inventory of fertile U-238 at end of life (EOL), which continues to act as a major scattering and absorption medium in fast reactors. This is consistent with established fast-reactor analyses, where U-238 capture and inelastic scattering represent dominant sources of reactivity and uncertainty.

On the microscopic level, a different picture emerges. While uranium isotopes show comparatively modest capture cross sections, many plutonium isotopes display large microscopic capture cross sections. At EOL, the macroscopic capture is carried mainly by Pu-239, Pu-240 and Pu-241, whose curves closely track the total-plutonium line. Heavier isotopes such as Pu-242 and Pu-243 contribute much less, owing to their lower concentrations and, in some cases, less favourable capture cross sections. Microscopic capture cross sections are consistent with physical expectations: fissile isotopes Pu-239 and Pu-241 exhibit high capture cross sections at low energies, decreasing with increasing neutron energy, whereas fertile isotopes Pu-240 and Pu-242 show strong resonance structures and significant capture over broad energy ranges. This dual behaviour explains the central role of plutonium in fast-reactor physics: fissile plutonium isotopes support power production, while fertile and non-fissile plutonium isotopes act as strong absorbers that both promote plutonium build-up and reduce reactivity through neutron capture.

For minor actinides (MAs), the macroscopic contribution is smaller than that of uranium and plutonium, with individual MA macroscopic capture cross sections typically of the order of $10^{-3}\,\mathrm{cm}^{-1}$ or lower. However, when summed, they produce a clearly identifiable MA-total capture curve, and their role is not negligible. The microscopic behaviour of MAs explains this effect: many MA isotopes exhibit very large microscopic capture cross sections, typically in the range 10^{3}–10^{5} barns at low energies, decreasing to tens of barns in the fast spectrum. This is consistent with evaluated nuclear data and with the established understanding that several MAs, notably Am-241 and Cm-244, are exceptionally strong absorbers. Physically, MAs are produced predominantly through neutron capture in plutonium isotopes. Once formed, they compete strongly for neutrons and act as efficient poisons, contributing significantly to reactivity loss even though their macroscopic capture cross section.

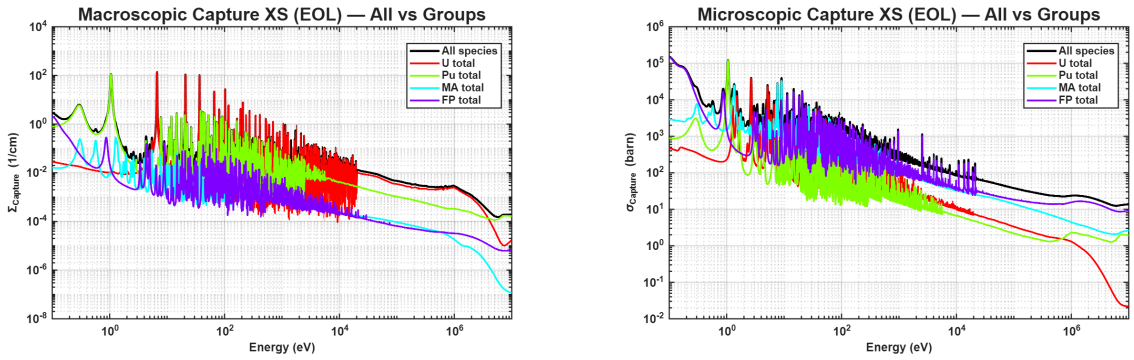

Figure 4.12: Macroscopic (Σ_c) and microscopic (σ_c) capture cross sections at EOL, shown for all isotopes and for the grouped contributions of U, Pu, MA, and FP.

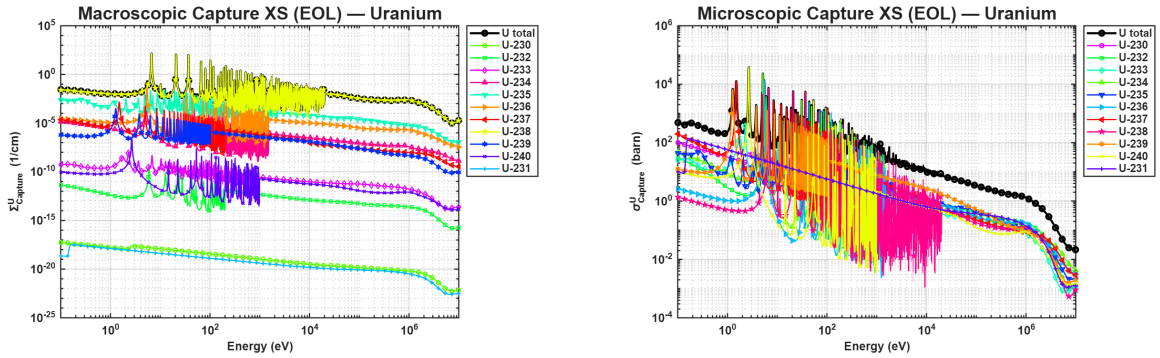

Figure 4.13: Macroscopic (Σ_c) and microscopic (σ_c) capture cross sections at EOL for the uranium isotopes (U).

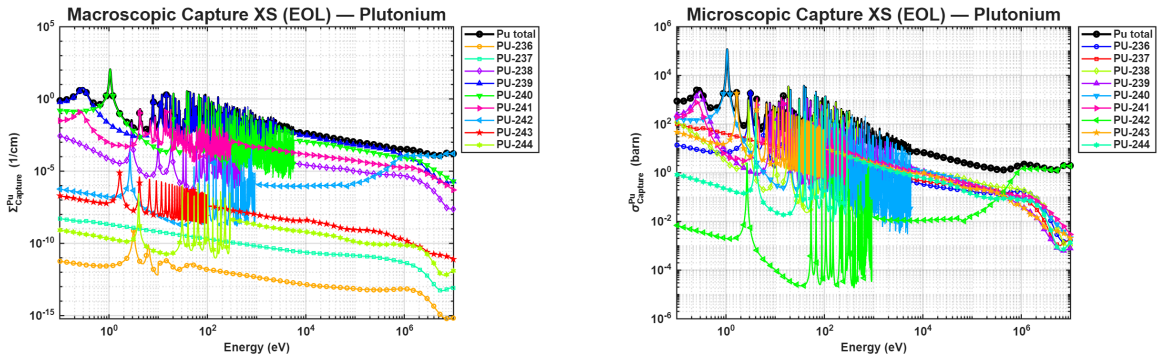

Figure 4.14: Macroscopic (Σ_c) and microscopic (σ_c) capture cross sections at EOL for the plutonium isotopes (Pu).

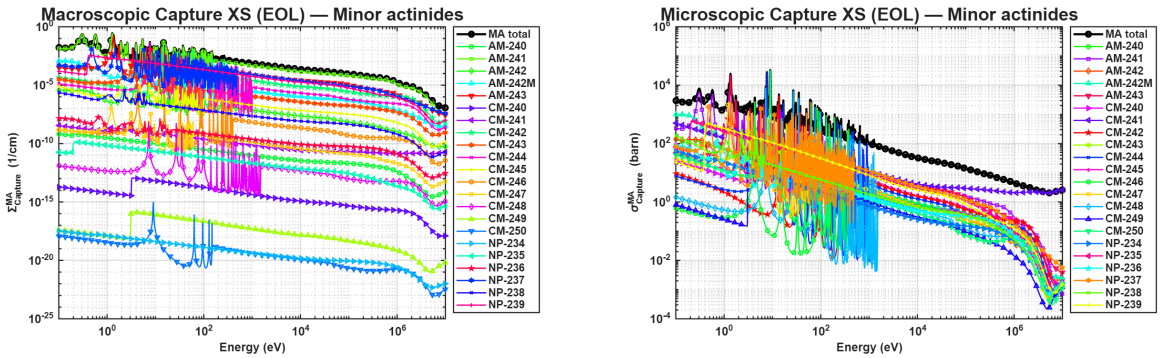

Figure 4.15: Macroscopic (Σ_c) and microscopic (σ_c) capture cross sections at EOL for the minor actinide isotopes (MA).

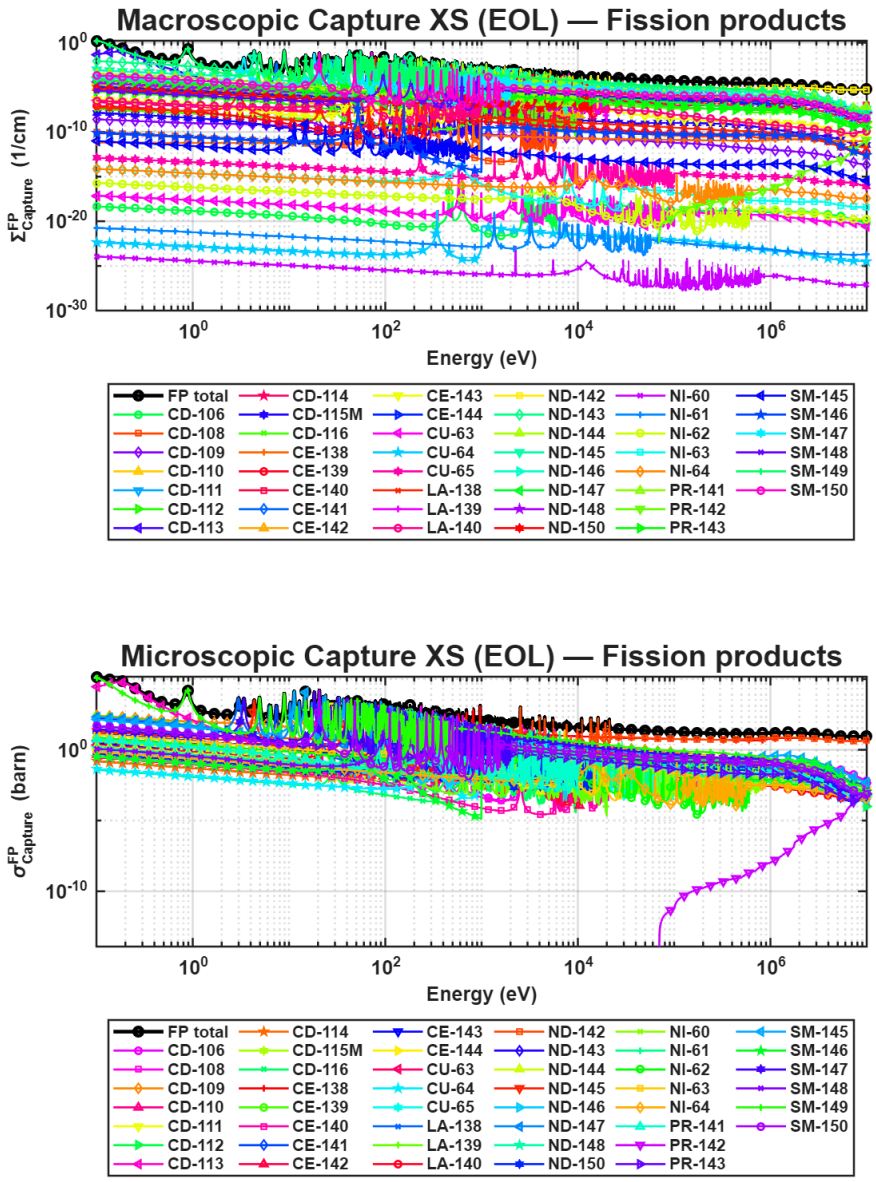

Figure 4.16: Macroscopic (Σ_c) and microscopic (σ_c) capture cross sections at EOL for the fission product isotopes (FP).

4.5.4.3 Fuel with impurities: Fission Reaction

The macroscopic fission cross-section plot shown on the left in Figures 4.17 at EOL shows that the total fission rate is dominated by plutonium over most of the fast-energy range. The Pu-total curve lies significantly above the U-total and MA-total contributions from a few eV up to about 1 MeV. Uranium contributes mainly through U-235 at low energy and through the onset of threshold fission in U-238 at higher energies, which explains the rise of the U-total curve above about 1 MeV. Minor actinides remain one to two orders of magnitude lower in macroscopic fission cross section, but their curve is still clearly visible and therefore contribute non-negligibly to the overall fission balance.

The corresponding microscopic fission plot displayed on the right in Figures 4.17 indicates why plutonium dominates the macroscopic behaviour. The microscopic fission cross sections of Pu isotopes are high at low energy and remain sizeable throughout the fast spectrum, so that even moderate plutonium number densities translate into large macroscopic fission cross sections. The U-total microscopic curve lies below Pu-total over most of the spectrum; only at the highest energies does the U contribution become comparable, associated with U-238 threshold fission. Minor actinides show comparatively smaller microscopic fission cross sections, which, combined with their low number densities, explains their limited macroscopic impact.

The uranium-only macroscopic fission plot shown on the left in Figures 4.18, confirms that, at EOL, the total uranium fission rate is small compared with plutonium. Among uranium isotopes, U-235 and U-238 provide the main contributions. U-235 dominates the uranium macroscopic fission rate at low and intermediate energies, while U-238 becomes important only above its fission threshold, where its macroscopic curve rises. Other isotopes such as U-233, U-234, U-236 and U-237 remain at least one order of magnitude lower in Σ_{f}.

In the microscopic uranium plot shown on the right in Figures 4.18 , the fissile isotope U-235 exhibits the highest microscopic fission cross section over most of the energy range, especially at low energies, followed by U-233 and, to a lesser extent, U-234 and U-236. U-238 shows much smaller σ_{f} at low energy and only becomes relevant at high energy, where its threshold fission cross section increases. The combination of these microscopic trends with the relatively low EOL fissile uranium inventory explains the small overall uranium contribution to fission in the fast spectrum considered.

For plutonium, the macroscopic fission plot shown on the left in Figures 4.19 indicates that, Pu-239 and Pu-241 are the principal contributors to the Pu-total curve. Their macroscopic fission cross sections lie well above those of the other Pu isotopes across most of the spectrum. Pu-240, Pu-242 and the heavier isotopes contribute at lower levels but still shape the Pu-total behaviour at specific energies. This reflects the breeding and depletion history of plutonium during burnup, where captures in Pu-239 and Pu-240 gradually populate higher-mass isotopes.

The microscopic plutonium plot shown on the right of Figures 4.19, highlights the strong fissile character of Pu-239 and Pu-241. These isotopes exhibit large microscopic fission cross sections at low energies, which gradually decrease with increasing energy but remain substantial throughout the fast range. Fertile or less fissile isotopes such as Pu-240 and Pu-242 have smaller σ_{f} and more pronounced resonance structures. Because Pu-239 and Pu-241 combine both high microscopic cross sections and relatively large number densities at EOL, they dominate the macroscopic plutonium fission rate and, consequently, the overall fission power production.

Finally, the minor-actinide macroscopic fission plot shown on the left of Figures 4.20 indicates, that the MA-total curve is well below the plutonium and uranium macroscopic fission curves,

typically in the range 10^{-7}–$10^{-5}\,\mathrm{cm}^{-1}$ over most of the fast spectrum. Individual MA isotopes (mainly americium and curium) contribute at different energy ranges, but none of them reaches the level of the main Pu fissile isotopes. This indicates that minor actinides play only a secondary role in power production at EOL.

The microscopic minor-actinide plot on the right of Figures 4.20 reveals that, MA isotopes possess modest microscopic fission cross sections in the fast spectrum, generally between 10^{-3} and a few barns, depending on the isotope and energy. Combined with their relatively low number densities, this leads to the small macroscopic MA fission contribution observed. Thus, in this configuration, minor actinides behave primarily as absorbers (as seen in the capture analysis) rather than as major contributors to the fission source.

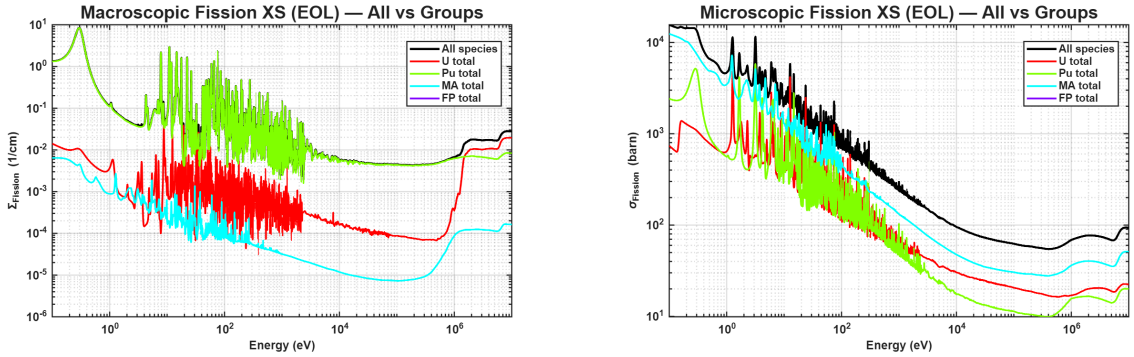

Figure 4.17: Macroscopic (Σ_f) and microscopic (σ_f) fission cross sections at EOL, shown for all isotopes and for the grouped contributions of U, Pu, MA, and FP.

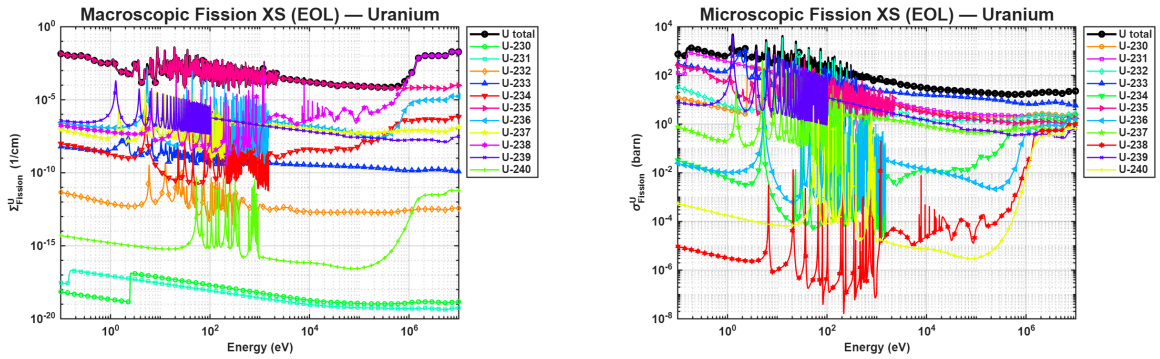

Figure 4.18: Macroscopic (Σ_f) and microscopic (σ_f) fission cross sections at EOL for the uranium isotopes (U).

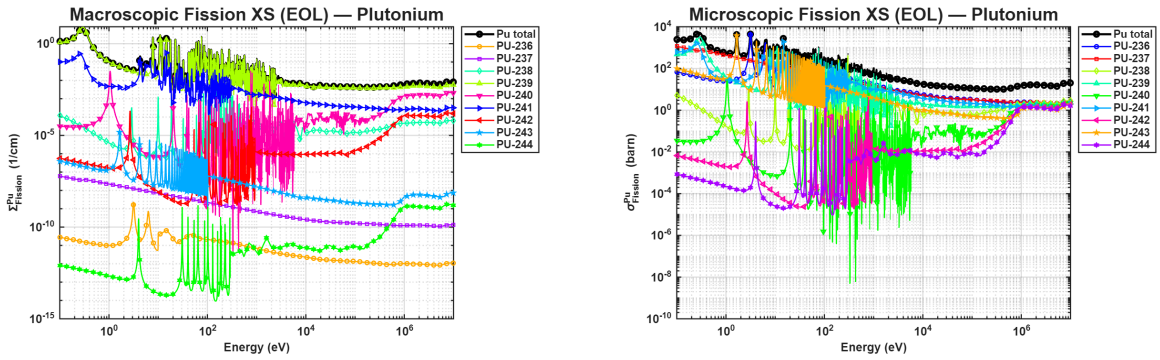

Figure 4.19: Macroscopic (Σ_f) and microscopic (σ_f) fission cross sections at EOL for the plutonium isotopes (Pu).

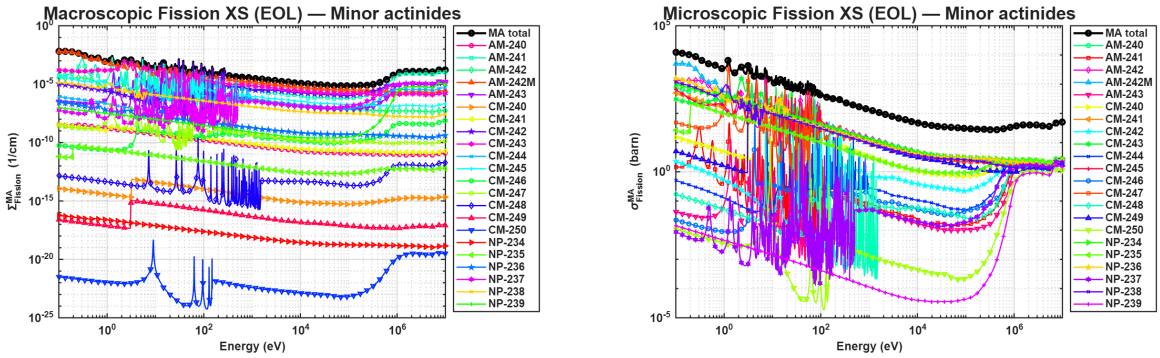

Figure 4.20: Macroscopic (Σ_f) and microscopic (σ_f) fission cross sections at EOL for the minor actinide isotopes (MA).

4.5.4.4 Reference case: Total Reaction

Figures 4.21–4.25 present the macroscopic and microscopic total reaction cross sections at end of life for the reference fuel, decomposed into the main actinide and fission-product families, enabling a direct comparison with the fuel-with-impurities configuration.

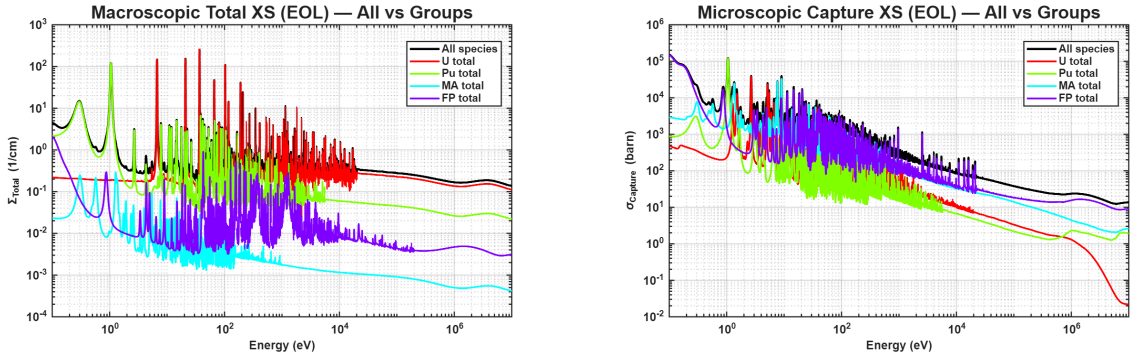

Figure 4.21: Macroscopic (Σ_t) and microscopic (σ_t) total cross sections at EOL, shown for all isotopes and for the grouped contributions of U, Pu, MA, and FP.

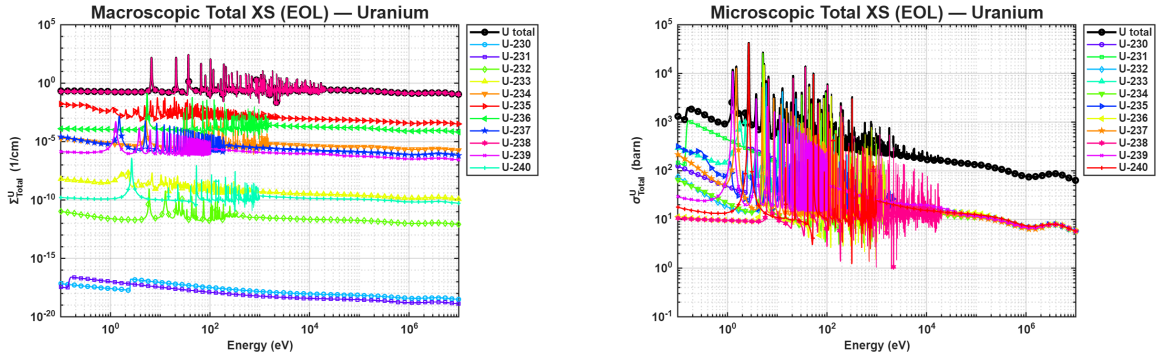

Figure 4.22: Macroscopic (Σ_t) and microscopic (σ_t) total cross sections at EOL for the uranium isotopes (U).

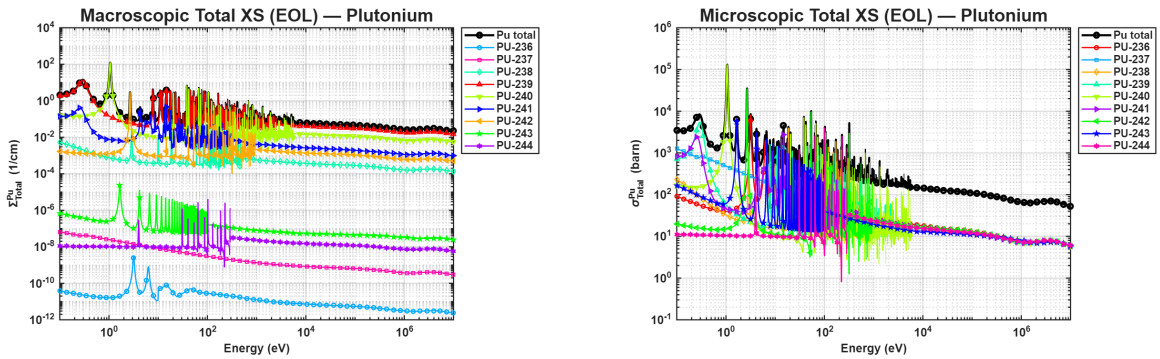

Figure 4.23: Macroscopic (Σ_t) and microscopic (σ_t) total cross sections at EOL for the plutonium isotopes (Pu).

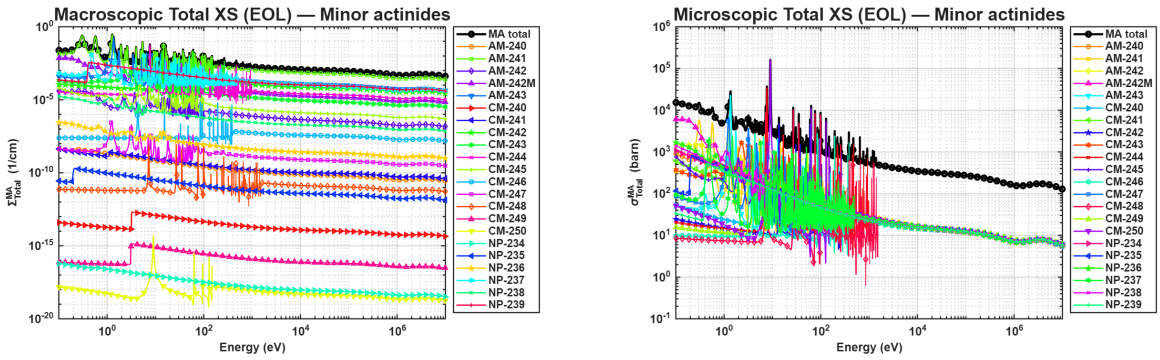

Figure 4.24: Macroscopic (Σ_t) and microscopic (σ_t) total cross sections at EOL for the minor actinide isotopes (MA).

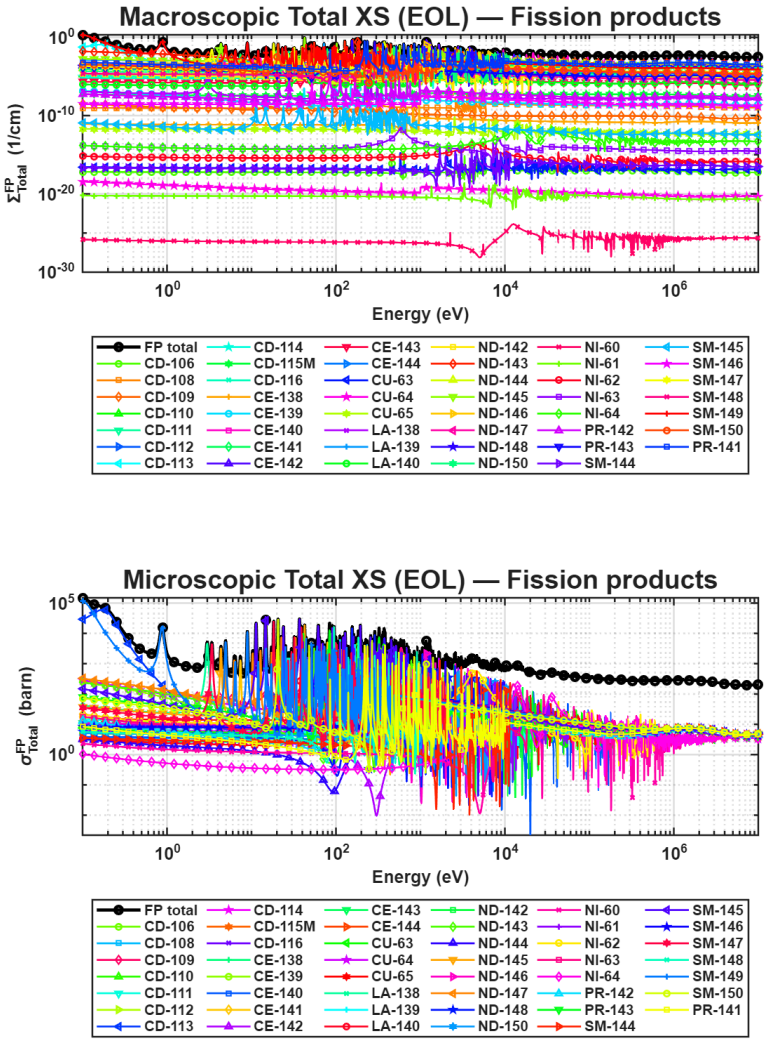

Figure 4.25: Macroscopic (Σ_c) and microscopic (σ_c) total cross sections at EOL for the fission product isotopes (FP).

In the reference case, the qualitative shape of the total cross-section curves is very similar to the fuel-with-impurities case, but the relative weight of each nuclide family is clearly different. The macroscopic 'all species" curve, shown on the left in Figures 4.21, is now even more tightly dominated by uranium and plutonium over the whole fast-energy range: the MA-total and FP-total curves lie roughly one additional order of magnitude below U and Pu compared to the impurities configuration. This reflects the fact that, in the reference fuel, the inventory of minor actinides and fission products consists only of what is bred during irradiation (plus a small initial amount of ^{241}Am), with no extra impurity vector added at BOL. On the microscopic plots, minor actinides and many fission products still exhibit very large total cross sections (10^3–10^5 barn), as in the previous case, but their macroscopic impact is reduced simply because their number densities are lower. Uranium remains dominated by ^{238}U, while the MA-total curve is lower and only a subset of Am/Cm/Np isotopes contributes significantly. Overall, the reference SPX-like fuel is therefore less poisoned than the impurity-loaded fuel: neutron interactions are controlled even more strongly by U and Pu, and the additional absorption from MAs and FPs is weaker, consistent with the higher k_{eff} observed for the reference case at the same burnup. The macroscopic total cross-section plot shows that, even at end of life, fission products contribute very little to the overall interaction probability compared to uranium and plutonium. In the reference fuel, their effect on the neutron balance at the macroscopic level therefore remains limited. However, the microscopic plot reveals that many fission-product isotopes have large total cross sections, meaning they are strong absorbers on a per-nucleus basis. Because their concentrations are relatively low and arise only from burnup (without an initial inventory, unlike the impurities case), this large microscopic strength does not translate into a dominant macroscopic effect. Fission products thus behave as strong microscopic absorbers but weak macroscopic contributors, affecting reactivity mainly through their gradual accumulation with burnup.

4.5.4.5 Reference case: Capture Reaction

For the SPX reference fuel, the capture behaviour at end of life is qualitatively similar to the fuel-with-impurities case, as illustrated in Figures 4.26–4.30, but the strength of the poisoning terms is noticeably smaller. In the macroscopic capture plot for all groups , the total capture cross section is still dominated by uranium and plutonium over the whole fast-energy range. The macroscopic contributions from minor actinides and fission products lie about one to two orders of magnitude below the U and Pu curves. In particular, the FP–total curve is systematically lower than in the fuel-with-impurities configuration, because in the reference case no fission-product/impurity vector is present at beginning of life and all fission products are generated during irradiation.

The microscopic capture plot (Figures 4.26 right) confirms that minor actinides and fission products retain very large microscopic cross sections, especially at low energies, as in the impurities case. However, in the SPX base fuel their number densities are smaller, so their macroscopic capture terms are reduced. The uranium- and plutonium-resolved plots, shown in Figures 4.27-4.28, indicate that essentially the same hierarchy as before (with U-238 and Pu-239/Pu-240 as the main contributors), but their summed capture accounts for a larger fraction of the total capture in the reference case because they compete with fewer strong absorbers.

Overall, compared to the fuel containing impurities, the SPX reference fuel exhibits weaker macroscopic capture by minor actinides and fission products at end of life (Figures 4.29-4.30). The neutron spectrum and actinide behaviour remain similar, but the absence of an initial impurity vector means fewer pre-existing poisons. This results in a smaller additional absorption term and is consistent with the slightly higher reactivity evolution observed for the reference configuration.

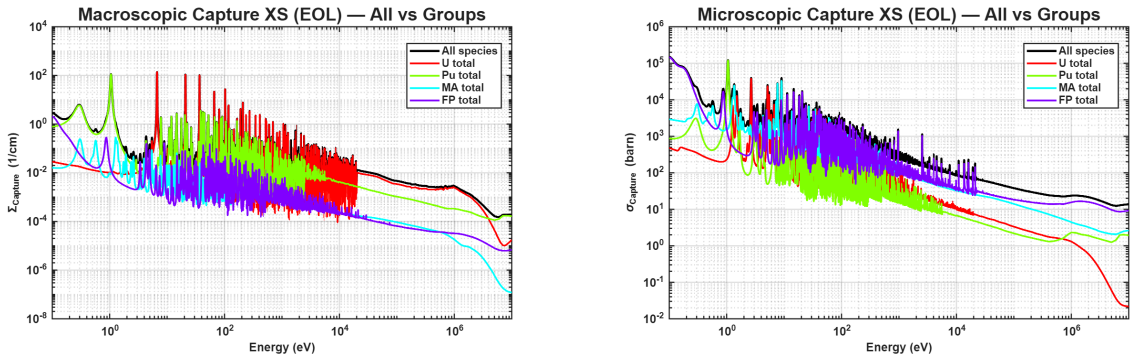

Figure 4.26: Macroscopic (Σ_c) and microscopic (σ_c) capture cross sections at EOL, shown for all isotopes and for the grouped contributions of U, Pu, MA, and FP.

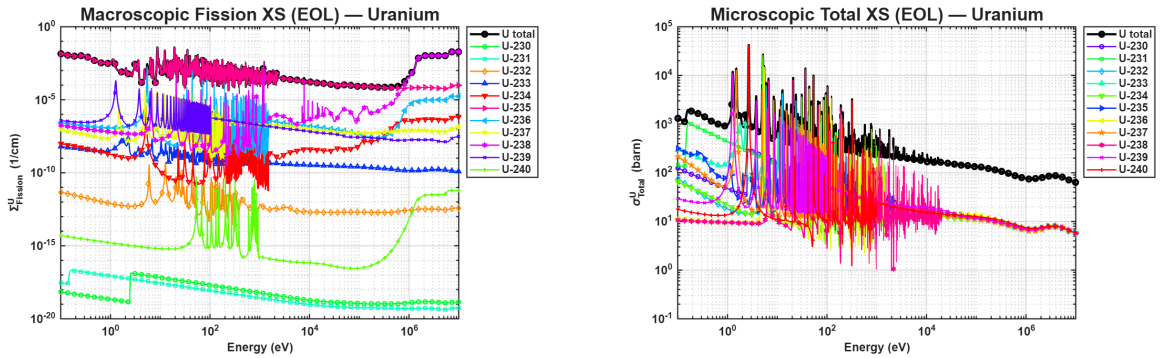

Figure 4.27: Macroscopic (Σ_c) and microscopic (σ_c) total cross sections at EOL for the uranium isotopes (U).

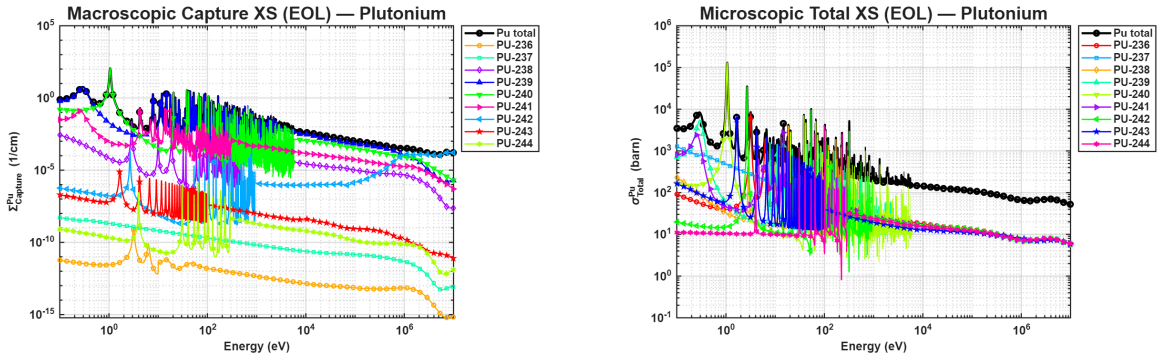

Figure 4.28: Macroscopic (Σ_c) and microscopic (σ_c) capture cross sections at EOL for the plutonium isotopes (Pu).

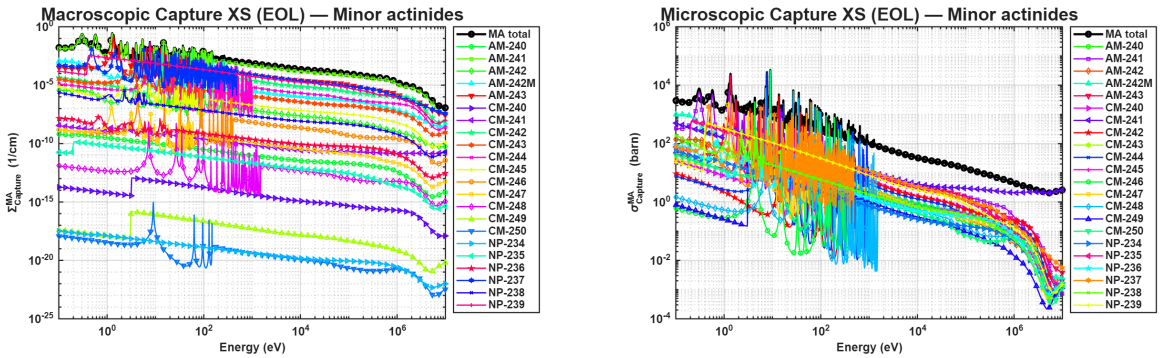

Figure 4.29: Macroscopic (Σ_c) and microscopic (σ_c) capture cross sections at EOL for the minor actinide isotopes (MA).

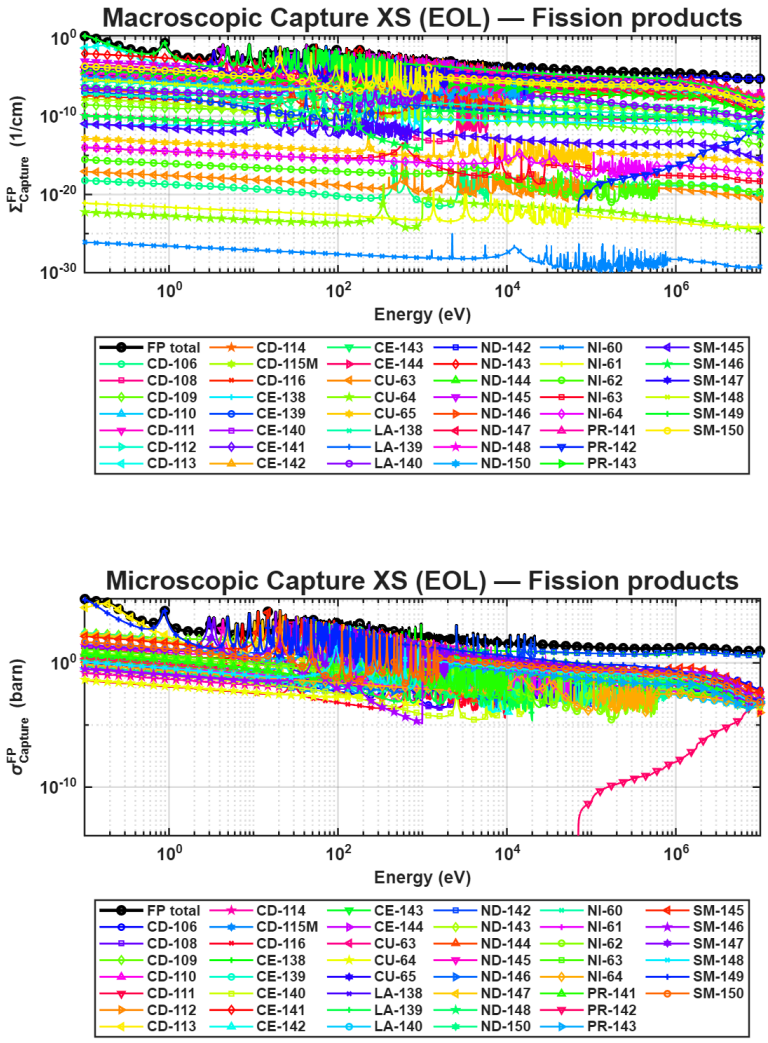

Figure 4.30: Macroscopic (Σ_c) and microscopic (σ_c) capture cross sections at EOL for the fission product isotopes (FP).

4.5.5 Reference case: Fission Reaction

From the macroscopic fission cross-section plots at EOL shown in Figure 4.31, the overall behaviour of the reference SPX fuel is very similar to the case with impurities: the total fission cross section is almost entirely governed by uranium and plutonium over the fast-energy range. The curves $\Sigma^{\mathrm{U}}_{\mathrm{fission}}$ and $\Sigma^{\mathrm{Pu}}_{\mathrm{fission}}$ practically reproduce the "all species" curve, while the MA contribution remains about two to three orders of magnitude lower and fission products do not contribute to this reaction channel. Compared to the impurities case, the reference fuel shows a slightly higher macroscopic Pu-fission level, because in the impurities case a small fraction of plutonium was replaced by non-fissionable impurities.

The uranium-resolved macroscopic and microscopic fission cross sections shown in Figure 4.32 confirm that at EOL the dominant fissioning isotope on the U side is still ^{235}U, with a visible fast-fission tail of ^{238}U. The shapes and magnitudes of the ^{235}U and ^{238}U curves are very close to those obtained for the fuel with impurities, indicating that the impurity loading does not significantly distort the fission spectrum seen by uranium isotopes.

The corresponding plutonium-resolved plots in Figure 4.33 show that ^{239}Pu and ^{241}Pu are the main contributors to $\Sigma^{\mathrm{Pu}}_{\mathrm{fission}}$, with ^{240}Pu and higher isotopes providing a smaller but non-negligible fast-fission contribution. In the reference case these Pu-fission curves are slightly higher in magnitude, again reflecting the absence of substitution by inert impurities.

Finally, the minor-actinide macroscopic and microscopic fission cross sections presented in Figure 4.34 illustrate that, in the reference case, MA fission remains lower than in the fuel containing impurities, because only the MAs produced by irradiation (and the small initial ^{241}Am inventory) are present. Nevertheless, the microscopic MA-fission cross sections remain sizeable in the fast range, so that once MAs are formed they can still contribute a small fraction of the power.

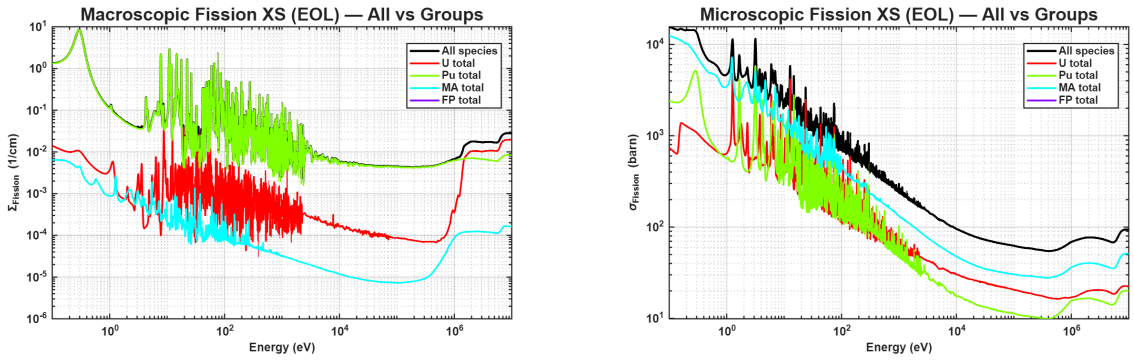

Figure 4.31: Macroscopic (Σ_f) and microscopic (σ_f) fission sections at EOL, shown for all isotopes and for the grouped contributions of U, Pu, MA, and FP.

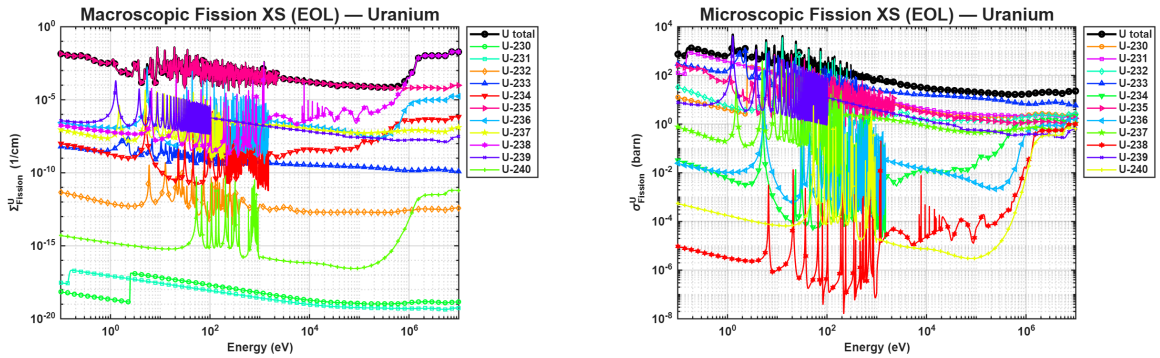

Figure 4.32: Macroscopic (Σ_f) and microscopic (σ_f) fission cross sections at EOL for the uranium isotopes (U).

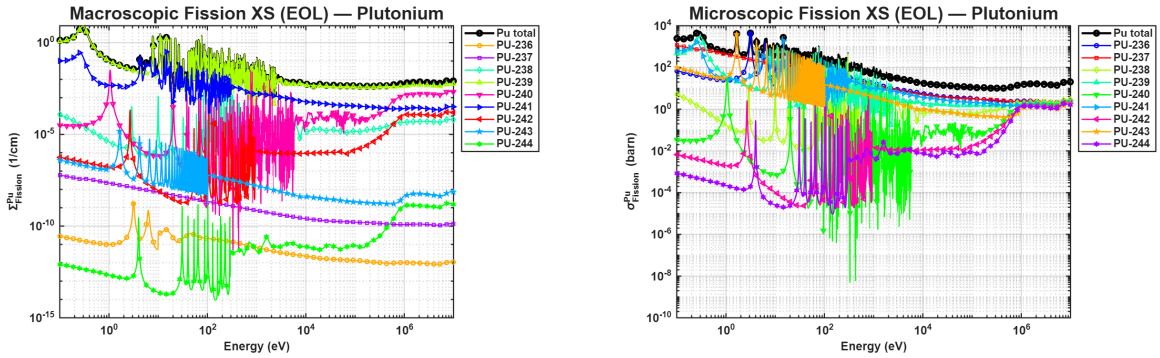

Figure 4.33: Macroscopic (Σ_f) and microscopic (σ_f) fission cross sections at EOL for the plutonium isotopes (Pu).

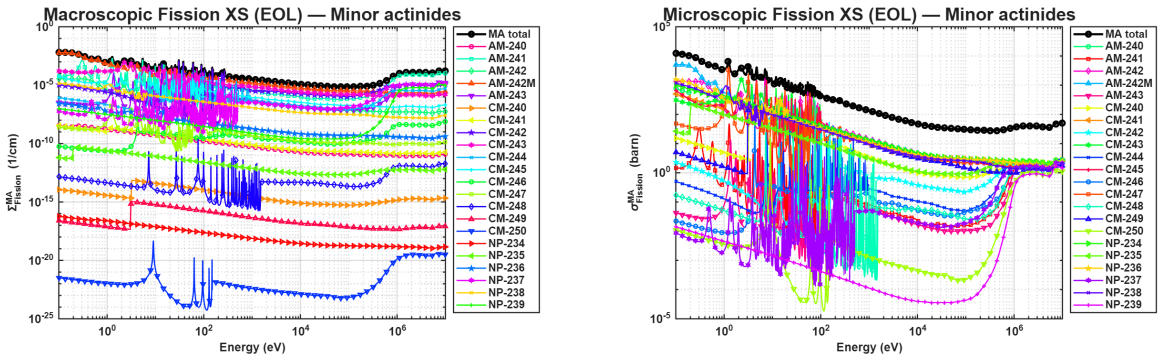

Figure 4.34: Macroscopic (Σ_f) and microscopic (σ_f) fission cross sections at EOL for the minor actinide isotopes (MA).

4.6 Reactivity Feedback Coefficients (Branch Calculations)

In order to assess the soundness of the modelling assumptions and the feasibility of reactor operation in the selected configuration, a comprehensive set of branch calculations was performed. Branch calculations consist in systematically perturbing key operational parameters around a reference state in order to quantify the reactor reactivity response under nominal and perturbed operating conditions. In the present work, branch calculations are employed as a primary verification tool to evaluate the behaviour of the main reactivity feedback mechanisms relevant to fast-spectrum systems. Specifically, fuel temperature, coolant temperature (and the associated density variation), and coolant voiding are independently perturbed in order to isolate and quantify their respective contributions to reactivity feedback. All reactivity variations presented in this section are evaluated relative to a reference operating state at each burnup step, while maintaining fixed geometry and material composition. This methodology ensures that the observed reactivity changes can be directly attributed to the parameter being perturbed and allows meaningful comparisons across burnup, feedback mechanisms, and fuel configurations.

4.6.1 Fuel Temperature Feedback — Reference SPX Case

In order to verify the expected inherent feedback behaviour of the reference SPX core and to assess the consistency of the modelling assumptions, fuel-temperature branch calculations were performed for the reference (impurity-free) configuration. The same methodology adopted for the impurity-loaded case was applied in order to ensure a consistent comparison.

Fuel temperature was perturbed around a reference value of

$$T_{\text{ref}} = 1500 \text{ K}, \tag{4.1}$$

while geometry, material composition at the given burnup, and coolant conditions were kept fixed. Two finite-difference Doppler reactivity coefficients were evaluated: a lower-temperature branch (1200–1500 K) and a higher-temperature branch (1800–1500 K).

4.6.1.1 Reactivity as a Function of Burnup and Fuel Temperature

Figure 4.35 (left) shows the evolution of reactivity as a function of burnup for fuel temperatures of 1200 K, 1500 K, and 1800 K in the reference SPX configuration.

For all temperature states, reactivity decreases monotonically with burnup, reflecting fissile depletion and the progressive accumulation of neutron absorbers. At each burnup step, higher fuel temperature corresponds to lower reactivity, confirming the presence of a negative fuel-temperature reactivity feedback.

The reactivity curves corresponding to different fuel temperatures remain nearly parallel over the entire irradiation cycle. This indicates that the reactivity difference induced by fuel temperature variations is approximately burnup-independent and that the magnitude of the Doppler feedback remains stable throughout irradiation.

4.6.1.2 Burnup Dependence of the Doppler Reactivity Coefficient

The burnup-dependent Doppler reactivity coefficients for the reference SPX case are reported in Table 4.17 and illustrated in Figure 4.35 (right).

For the 1200–1500 K branch, the Doppler coefficient remains consistently negative over the entire burnup range, with magnitude on the order of 10^{-1}–10^{0} pcm/K. This behaviour is consistent

with literature expectations for fast-spectrum systems, where the Doppler effect is weaker than in thermal reactors but still provides a stabilising negative feedback.

The 1800–1500 K branch also yields predominantly negative coefficients; however, the magnitude of the feedback decreases with burnup. At high burnup, the coefficient approaches values comparable to the one-sigma Monte Carlo statistical uncertainty, and at end-of-life it becomes statistically indistinguishable from zero within 1σ.

This trend indicates a progressive weakening of the Doppler feedback at elevated fuel temperatures as burnup increases. Such behaviour can be attributed to the intrinsically small Doppler effect in fast spectra, combined with changes in isotopic composition and the finite-difference nature of the coefficient evaluation across a large temperature interval.

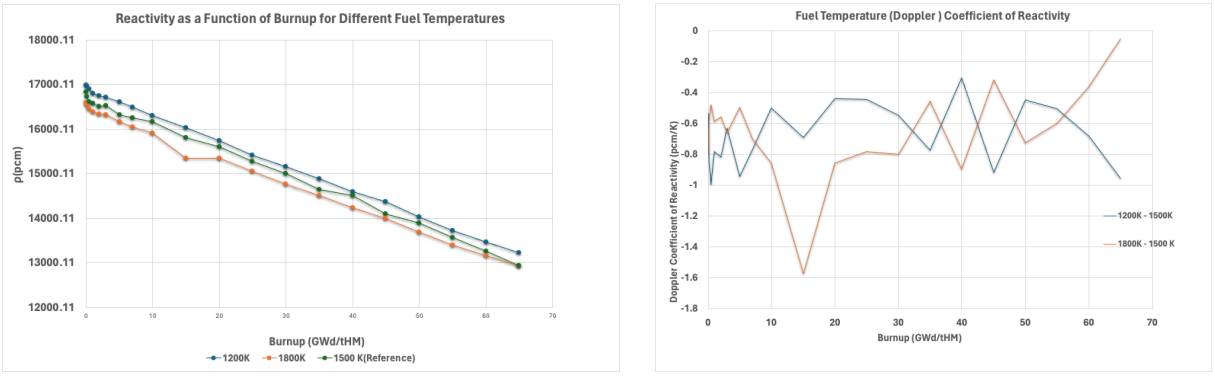

Figure 4.35: Reactivity variation ρ from temperature branch calculations and Doppler broadening for fuel of the reference SPX benchmark.

Table 4.17: Burnup-dependent Doppler reactivity coefficient evaluated between 1200–1500 K and 1800–1500 K, with one-sigma statistical uncertainty propagated from Monte Carlo calculations.

BU (MWd/kgHM)	$\alpha_{D,1200-1500}$ **(pcm/K)**	$\sigma_{\alpha,1200-1500}$ **(pcm/K)**	$\alpha_{D,1800-1500}$ **(pcm/K)**	$\sigma_{\alpha,1800-1500}$ **(pcm/K)**
0.00	-0.5362	0.2496	-0.7954	0.2502
0.10	-0.8227	0.1206	-0.5907	0.1252
0.50	-0.9978	0.1729	-0.4806	0.1757
1.00	-0.7843	0.2700	-0.5859	0.2624
2.00	-0.8178	0.2378	-0.5564	0.2353
3.00	-0.6304	1.6263	-0.6613	1.6284
5.00	-0.9444	1.4240	-0.4957	1.4241
7.00	-0.7716	0.2694	-0.7007	0.2694
10.00	-0.5005	0.1741	-0.8555	0.1706
15.00	-0.6928	0.1449	-1.5750	0.1324
20.00	-0.4410	0.1517	-0.8550	0.1790
25.00	-0.4443	0.3040	-0.7820	0.3046
30.00	-0.5480	0.1564	-0.8018	0.1347
35.00	-0.7725	0.2076	-0.4572	0.2097
40.00	-0.3042	0.2372	-0.8946	0.2262
45.00	-0.9172	0.2550	-0.3202	0.2508
50.00	-0.4491	0.1503	-0.7284	0.1474
55.00	-0.5046	0.1807	-0.5988	0.1829
60.00	-0.6830	0.2238	-0.3616	0.1922
65.00	-0.9568	0.1804	-0.0531	0.1727

4.6.1.3 Discussion

Overall, the reference SPX configuration exhibits the expected stabilising fuel-temperature reactivity feedback across the irradiation cycle. Although the Doppler effect is weak in absolute magnitude, its sign remains negative and its behaviour is consistent with established fast-reactor physics. The reduction of the high-temperature Doppler coefficient at large burnup highlights the limited sensitivity of the fast-spectrum system to fuel temperature perturbations at elevated temperatures, rather than indicating a loss of inherent safety feedback.

4.6.2 Fuel Temperature Feedback — Fuel with impurities

Having established the expected fuel-temperature feedback behaviour for the reference SPX configuration, the same analysis is now applied to the impurity-loaded fuel in order to assess the impact of impurities on Doppler reactivity feedback.

4.6.2.1 Reactivity as a Function of Burnup and Fuel Temperature

Figure 4.36 (left) shows the evolution of reactivity as a function of burnup for three fuel temperatures (1200 K, 1500 K, and 1800 K) in the impurity-loaded fuel configuration.

For all temperature states, reactivity decreases monotonically with burnup, as expected due to fissile depletion and the progressive accumulation of neutron-absorbing isotopes, including higher actinides and fission products. The reactivity curves corresponding to different fuel temperatures remain nearly parallel throughout the irradiation cycle, indicating that the reactivity difference induced by fuel temperature variations is approximately burnup-independent.

The relative ordering of the curves is preserved over the entire burnup range, with higher fuel temperatures consistently associated with lower reactivity. This behaviour confirms the presence of a negative fuel-temperature reactivity feedback, which constitutes a fundamental safety characteristic of nuclear fuel. The near-parallelism of the curves further suggests that, in this fast-spectrum system, the Doppler effect is weak in magnitude but structurally stable, and that its effectiveness is not significantly altered by burnup. The introduction of impurities results primarily in a shift of the absolute reactivity level, without modifying the overall trend.

4.6.2.2 Burnup Dependence of the Doppler Reactivity Coefficient

The corresponding burnup-dependent Doppler reactivity coefficients are shown in Figure 4.36 (right) and reported numerically in Table 4.18.

For the 1200–1500 K branch, the Doppler coefficient remains consistently negative across the entire burnup range, with magnitudes on the order of a few pcm/K. Although small—as expected for a fast-spectrum system—this behaviour is consistent with the stabilising Doppler broadening mechanism typically reported in the literature for fast reactors, where the net fuel-temperature feedback is weaker than in thermal systems but remains negative.

In contrast, the 1800–1500 K branch exhibits a markedly different behaviour: except at beginning-of-life, the computed coefficients are predominantly positive, indicating that the reactivity at 1800 K is higher than that at the 1500 K reference for most burnup points. This sign reversal is not consistent with the conventional expectation of increasingly negative reactivity with increasing fuel temperature.

Given the finite-difference nature of the coefficient evaluation and the intrinsically small magnitude of the Doppler effect in fast-spectrum systems, this behaviour may reflect limitations of the present branch calculation setup—such as, treatment of impurity cross sections at elevated temperatures.

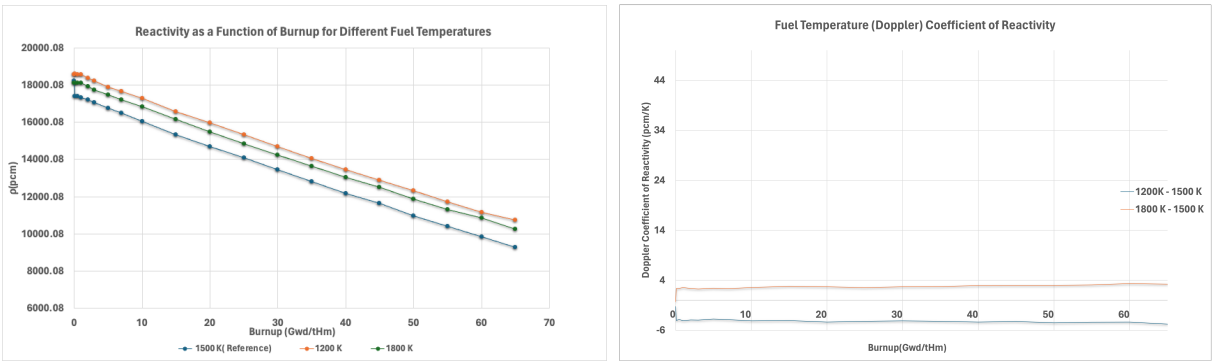

Figure 4.36: Reactivity variation ρ as a function of fuel temperature and the Doppler broadening effect for impurity-loaded fuel.

Table 4.18: Burnup-dependent Doppler reactivity coefficient evaluated between 1200–1500 K and 1800–1500 K, expressed in pcm/K, with one-sigma statistical uncertainty propagated from Monte Carlo calculations.

BU (MWd/kgHM)	$\alpha_{D,1200-1500}$ **(pcm/K)**	$\sigma_{\alpha,1200-1500}$ **(pcm/K)**	$\alpha_{D,1800-1500}$ **(pcm/K)**	$\sigma_{\alpha,1800-1500}$ **(pcm/K)**
0.00	-1.2387	0.0824	-0.2701	0.1243
0.10	-4.0198	0.1045	2.3335	0.0864
0.50	-3.8365	0.0711	2.3850	0.0802
1.00	-4.0935	0.1184	2.5660	0.0846
2.00	-3.9299	0.0803	2.3535	0.1252
3.00	-3.9721	0.1137	2.2568	0.0751
5.00	-3.7575	0.0658	2.3886	0.1541
7.00	-3.8882	0.1510	2.3204	0.1236
10.00	-4.1148	0.1190	2.5439	0.1099
15.00	-4.0625	0.0919	2.7893	0.1122
20.00	-4.3510	0.1296	2.7181	0.0822
25.00	-4.2092	0.0745	2.5366	0.1008
30.00	-4.1060	0.0977	2.6965	0.1525
35.00	-4.1981	0.1581	2.7211	0.0825
40.00	-4.3482	0.0722	2.9586	0.0833
45.00	-4.2488	0.0683	2.9611	0.0794
50.00	-4.5181	0.0693	2.9851	0.1206
55.00	-4.3984	0.1398	3.0752	0.1020
60.00	-4.3537	0.0963	3.3348	0.1239
65.00	-4.7749	0.1026	3.2153	0.0322

4.6.2.3 Discussion

Several of the positive coefficients observed for the 1800–1500 K branch are significantly larger than the propagated one-sigma Monte Carlo statistical uncertainties reported in Table 4.18. This indicates that the observed sign reversal is not solely attributable to statistical noise, but likely reflects a physical effect. Further verification of the branch calculation framework, including higher-statistics calculations and consistency checks of material temperature treatment and burnup state selection, should be carefully verified before drawing definitive conclusions.

4.6.3 Coolant Temperature Feedback — Reference SPX Case

Fuel depletion calculations were complemented by coolant temperature branch calculations to evaluate the sensitivity of the reference SPX core to moderate variations in coolant temperature and the associated changes in sodium coolant density. In contrast to thermal reactor systems, where the coolant also acts as a moderator, the sodium coolant in the fast-spectrum SPX configuration plays a secondary neutronic role and primarily affects neutron scattering, absorption, and the local neutron energy spectrum rather than moderation. Coolant temperature was perturbed around the reference value of 743.15 K while keeping geometry and fuel composition at the given burnup fixed. Figure 4.37 (left) shows the evolution of reactivity as a function of burnup for three coolant temperature states (705.15 K, 743.15 K, and 780.15 K). For all cases, reactivity decreases almost linearly with burnup, reflecting the dominant effects of fissile depletion and the accumulation of neutron-absorbing fission products. The reactivity curves remain nearly parallel and closely spaced over the entire irradiation cycle, indicating that moderate sodium temperature and density variations introduce only a minor perturbation to the neutron balance when compared to the overall reactivity loss driven by fuel depletion. This behavior confirms that, in the present fast-spectrum system, sodium-related feedbacks remain weak relative to fuel-depletion effects. The corresponding sodium temperature reactivity coefficients are reported in Table 4.19 and illustrated in Figure 4.37 (right). The coefficients are of small magnitude, typically on the order of a few pcm/K, and exhibit non-monotonic variations with burnup, including localized sign changes. Positive values of the sodium temperature coefficient indicate that an increase in coolant temperature—corresponding to a reduction in sodium density—leads to a slight increase in reactivity. In a fast-spectrum infinite lattice, this behavior arises from reduced parasitic absorption in the sodium coolant combined with moderate spectrum hardening, which together can increase the neutron population available for fission. Negative values of the sodium temperature coefficient arise when the spectral changes associated with reduced sodium density become unfavorable to reactivity. Although sodium density reduction decreases absorption in the coolant itself, the accompanying spectrum hardening may shift neutrons into energy regions where fissile fission cross sections are lower and absorption in fuel, fertile isotopes, or fission products is enhanced. Under these conditions, the resulting reduction in the fission-to-capture ratio outweighs the positive contribution from reduced sodium absorption, leading to a net decrease in reactivity. Small oscillations and occasional sign changes observed at low and intermediate burnup occur when the magnitude of the coefficient becomes comparable to the propagated one-sigma Monte Carlo statistical uncertainty and reflect the finite-difference nature of the coefficient evaluation rather than a dominant physical feedback mechanism. Overall, the reference SPX configuration exhibits a weak, bounded, and burnup-dependent sodium temperature feedback that remains secondary to fuel-temperature- and fuel-depletion-driven reactivity effects throughout the irradiation cycle.

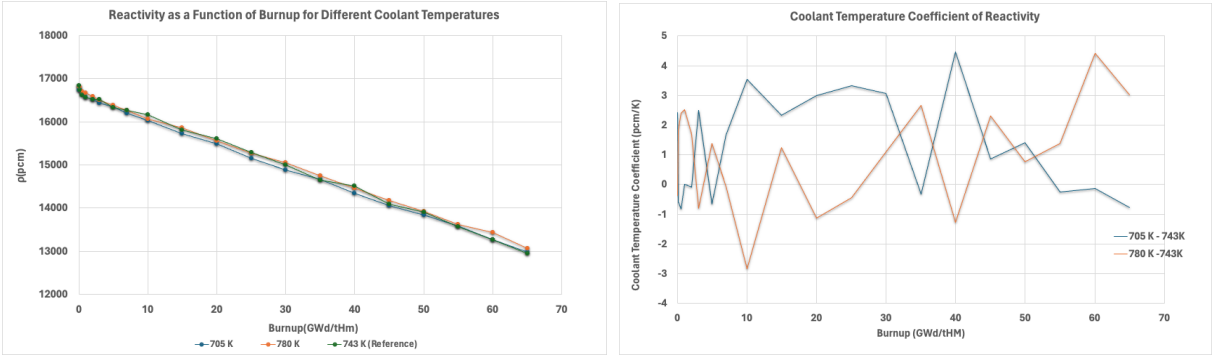

Figure 4.37: Reactivity variation ρ from coolant branch calculations and coolant coefficient for fuel of the reference SPX benchmark.

Table 4.19: Burnup-dependent coolant temperature reactivity coefficient evaluated between 705.15–743.15 K and 780.15–743.15 K, with one-sigma statistical uncertainty propagated from Monte Carlo calculations.

BU (MWd/kgHM)	$\alpha_{C,705-743}$ **(pcm/K)**	$\sigma_{\alpha,705-743}$ **(pcm/K)**	$\alpha_{C,780-743}$ **(pcm/K)**	$\sigma_{\alpha,780-743}$ **(pcm/K)**
0.00	2.4375	0.2455	-0.3690	0.2457
0.10	-0.5731	0.1223	1.8291	0.1156
0.50	-0.8156	0.1626	2.4081	0.1708
1.00	0.0000	0.2550	2.5215	0.2656
2.00	-0.0743	0.2426	1.6902	0.2374
3.00	2.4929	1.6278	-0.7994	1.6278
5.00	-0.6533	1.4245	1.3809	1.4239
7.00	1.6655	0.2774	-0.0561	0.2949
10.00	3.5294	0.1946	-2.8339	0.1798
15.00	2.3269	0.1451	1.2466	0.1355
20.00	2.9863	0.1585	-1.1213	0.1614
25.00	3.3350	0.3018	-0.4403	0.3045
30.00	3.0674	0.1122	1.0976	0.1217
35.00	-0.3108	0.2219	2.6581	0.2108
40.00	4.4529	0.1898	-1.2677	0.1888
45.00	0.8663	0.2443	2.3004	0.2560
50.00	1.4045	0.1409	0.7708	0.1423
55.00	-0.2390	0.1906	1.3736	0.1764
60.00	-0.1404	0.1991	4.4251	0.1947
65.00	-0.7677	0.1805	3.0276	0.1920

4.6.4 Coolant Temperature Feedback — Fuel with impurities

Following the assessment of coolant temperature feedback for the reference SPX configuration, the same coolant temperature branch methodology was applied to the impurity-loaded fuel in order to evaluate the impact of impurities on coolant-related reactivity behaviour. Coolant temperature was perturbed around the reference value of 743.15 K, with additional branch states at 705.15 K and 780.15 K, while geometry and fuel composition at the given burnup were kept fixed. Figure 4.38 (left) shows the evolution of reactivity as a function of burnup for the three coolant temperature states in the impurity-loaded configuration. As in the reference case, reactivity decreases almost linearly with burnup for all coolant temperatures, reflecting the dominant contribution of fissile depletion and the accumulation of neutron-absorbing fission products. The reactivity curves corresponding to 705.15 K, 743.15 K, and 780.15 K remain closely spaced and nearly parallel over the entire irradiation cycle, confirming that coolant temperature and sodium density variations introduce only a minor perturbation to the overall neutron balance when compared to fuel-depletion-driven reactivity effects. The corresponding coolant temperature reactivity coefficients are reported in Table 4.20 and illustrated in Figure 4.38 (right). As in the reference SPX configuration, the coefficients are predominantly positive and of small magnitude, typically on the order of a few pcm/K, indicating that an increase in coolant temperature—corresponding to a reduction in sodium density—tends to produce a slight increase in reactivity. However, the coefficients exhibit a pronounced asymmetry when evaluated below and above the reference temperature, with systematically larger values obtained between 705.15–743.15 K than between 780.15–743.15 K. This behaviour indicates a nonlinear reactivity response to coolant temperature, rather than a simple linear dependence. In contrast to the reference configuration, the impurity-loaded case does not exhibit increased variability in the coolant temperature coefficient. The evolution with burnup remains comparatively smooth and bounded, without pronounced oscillations. The presence of impurities therefore does not introduce spectral instability in the coolant-density feedback response, but instead results in a steady and moderate reactivity sensitivity to sodium density variations. The impurity-loaded configuration exhibits a predominantly positive coolant temperature (density) coefficient, with a pronounced peak at beginning-of-life. This elevated BOL value reflects the strong compositional sensitivity of the fresh fuel combined with the finite-difference evaluation of the coefficient, rather than the establishment of a dominant coolant-driven feedback mechanism. Following the initial burnup step, the magnitude decreases and remains moderate and bounded throughout the irradiation cycle. Although the coefficient does not display progressive growth or strong nonlinear behaviour with burnup, its predominantly positive sign is less favourable from an inherent-safety perspective and indicates a limited intrinsic stabilising contribution from sodium density feedback.

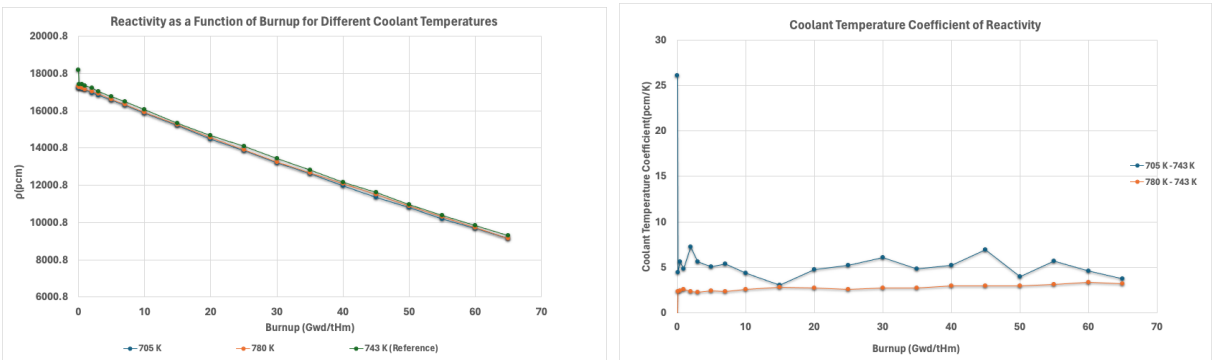

Figure 4.38: Reactivity variation ρ as a function of coolant density, illustrating the coolant reactivity effect for impurity-loaded fuel.

Table 4.20: Burnup-dependent coolant temperature reactivity coefficient evaluated between 705–743 K (low) and 780–743 K (high), expressed in pcm/K, with one-sigma statistical uncertainty propagated from Monte Carlo calculations. Uncertainties σ_α were converted to pcm/K using 1 pcm $= 10^{-5}\Delta k/k$.

BU (MWd/kgHM)	$\boldsymbol{\alpha_{C,705-743}}$ **(pcm/K)**	$\boldsymbol{\sigma_{\alpha,705-743}}$ **(pcm/K)**	$\boldsymbol{\alpha_{C,780-743}}$ **(pcm/K)**	$\boldsymbol{\sigma_{\alpha,780-743}}$ **(pcm/K)**
0.00	26.0874	0.1069	-0.2701	0.0994
0.10	4.4476	0.1008	2.3335	0.1030
0.50	5.6173	0.0843	2.3850	0.1260
1.00	4.8401	0.0829	2.5660	0.0938
2.00	7.2799	0.0959	2.3535	0.1120
3.00	5.6293	0.1328	2.2568	0.1561
5.00	5.0564	0.1390	2.3886	0.1264
7.00	5.3480	0.1529	2.3204	0.1672
10.00	4.3679	0.1107	2.5439	0.1565
15.00	3.0243	0.0804	2.7893	0.0870
20.00	4.7854	0.1200	2.7181	0.1240
25.00	5.2486	0.0650	2.5366	0.0837
30.00	6.0892	0.0867	2.6965	0.1119
35.00	4.8551	0.1541	2.7211	0.1726
40.00	5.1969	0.1182	2.9586	0.1093
45.00	6.9136	0.0716	2.9611	0.1028
50.00	3.9390	0.0741	2.9851	0.0698
55.00	5.6443	0.1223	3.0752	0.1422
60.00	4.6243	0.1130	3.3348	0.1266
65.00	3.7136	0.0878	3.2153	0.1150

4.6.5 Void Reactivity Coefficient

Figure 4.39 shows the burnup dependence of the void reactivity coefficient for the SPX configuration, comparing the reference fuel and the impurity-loaded fuel. In both cases, the void coefficient is positive over the entire irradiation cycle, indicating that the removal of sodium coolant leads to a net increase in reactivity. This behavior is consistent with fast-spectrum systems, where the coolant does not act as a moderator and its removal reduces parasitic neutron absorption while inducing spectrum hardening. For the reference fuel, the void reactivity coefficient remains moderate in magnitude and exhibits limited variation with burnup. Small non-monotonic fluctuations are observed, which reflect gradual changes in the isotopic composition of the fuel as well as the finite-difference and Monte Carlo nature of the coefficient evaluation. Overall, the void worth remains bounded and does not display a strong systematic dependence on burnup. In contrast, the impurity-loaded fuel exhibits a significantly larger void reactivity coefficient that increases monotonically with burnup. The presence of additional absorbing nuclides in the fuel increases the sensitivity of the neutron balance to spectral changes induced by coolant removal. As burnup progresses, the combined effect of impurities and fission product accumulation enhances the favorable impact of spectrum hardening, leading to a progressively larger positive void worth. This trend reflects an increased coupling between coolant removal and local spectral effects rather than the emergence of a new feedback mechanism. It is important to note that these results are obtained within an infinite lattice framework and therefore represent local neutronic effects only. Within this modeling context, the void reactivity coefficient provides a comparative measure of spectral sensitivity and confirms that impurity loading amplifies the reactivity response to coolant voiding without altering its qualitative behavior.

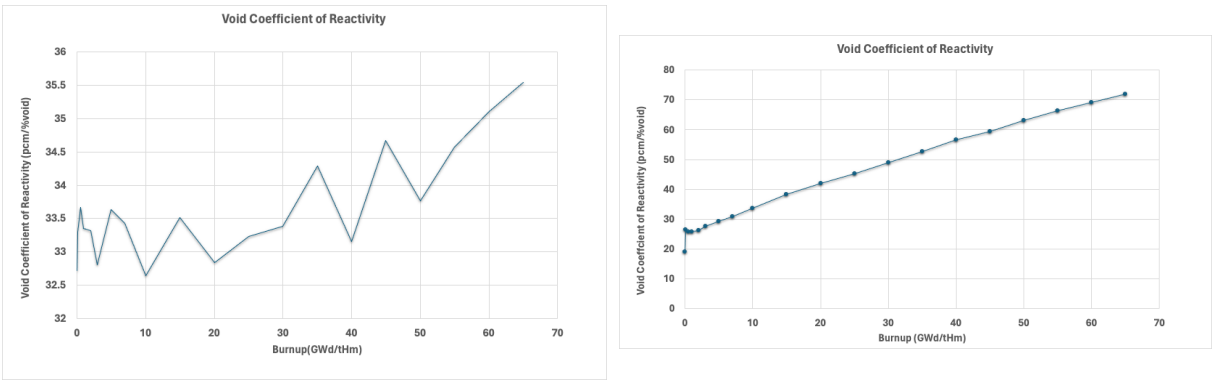

Figure 4.39: Void reactivity coefficient for the SPX configuration: reference fuel (left) and impurity-loaded fuel (right).

Table 4.21: Burnup-dependent void reactivity coefficient for the reference SPX fuel,expressed in pcm/%void, with one-sigma statistical uncertainty propagated from Monte Carlo calculations.

BU (MWd/kgHM)	$\boldsymbol{\alpha_v}$ **(pcm/%void)**	$\boldsymbol{\sigma_{\alpha_v}}$ **(pcm/%void)**
0.00	32.7204	0.2493
0.10	33.2919	0.1290
0.50	33.6657	0.1854
1.00	33.3573	0.2614
2.00	33.3196	0.2455
3.00	32.8042	1.6276
5.00	33.6303	1.4249
7.00	33.4333	0.2742
10.00	32.6418	0.1763
15.00	33.5139	0.1513
20.00	32.8348	0.1541
25.00	33.2353	0.3058
30.00	33.3856	0.1163
35.00	34.2940	0.2359
40.00	33.1559	0.2004
45.00	34.6765	0.2472
50.00	33.7694	0.1502
55.00	34.5784	0.1788
60.00	35.1039	0.1956
65.00	35.5408	0.1863

Table 4.22: Burnup-dependent void reactivity coefficient for the impurity-loaded fuel, expressed in pcm/%void, with one-sigma statistical uncertainty propagated from Monte Carlo calculations.

BU (MWd/kgHM)	$\boldsymbol{\alpha_v}$ **(pcm/%void)**	$\boldsymbol{\sigma_{\alpha_v}}$ **(pcm/%void)**
0.00	18.9517	0.0921
0.10	26.5035	0.1081
0.50	25.7175	0.1113
1.00	25.7567	0.0969
2.00	26.3249	0.1078
3.00	27.5484	0.1282
5.00	29.3045	0.0821
7.00	30.9583	0.1516
10.00	33.6834	0.1208
15.00	38.3322	0.1096
20.00	42.0305	0.1147
25.00	45.2819	0.0871
30.00	48.9454	0.0838
35.00	52.7041	0.1754
40.00	56.6251	0.0983
45.00	59.3052	0.0809
50.00	63.1634	0.0882
55.00	66.3459	0.1158
60.00	69.1774	0.0784
65.00	72.0312	0.1136

4.7 Overall Comparison Between Reference and Impurity-Loaded Cases

Taken together, the results for the reference SPX configuration confirm that the lattice model reproduces the expected neutronic behaviour of a sodium-cooled fast reactor. The infinite-medium multiplication factor decreases smoothly with burnup, reflecting the progressive depletion of fissile material and the accumulation of absorbers. Most importantly, the Doppler reactivity coefficient remains negative over the entire burnup range. This confirms the presence of a stable intrinsic fuel-temperature feedback mechanism, which is a fundamental safety requirement for fast-spectrum systems. Minor irregularities in the burnup-dependent curve are attributable to Monte Carlo statistical uncertainties rather than to any underlying physical instability, as indicated by the associated one-sigma error bars. The overall trend is consistent with the expected resonance broadening effect and demonstrates physically sound behaviour of the reference SPX fuel.

In contrast, the impurity-loaded fuel exhibits a markedly different Doppler response. Although the general depletion trend of k_∞ remains comparable to the reference case, the Doppler reactivity coefficient becomes positive. Such behaviour is physically undesirable and contradicts the fundamental safety principle that fuel temperature increases must produce a negative reactivity insertion. A positive Doppler coefficient implies that an increase in fuel temperature would increase reactivity, thereby reducing the inherent stability of the system. This indicates that the introduction of impurities significantly alters the resonance absorption balance of the fuel.

Regarding coolant temperature feedback, the reference SPX configuration exhibits weak reactivity sensitivity to coolant density variations, which is typical of fast-spectrum systems where the moderation effects are limited. In the impurity-loaded case, the coolant temperature coefficient shifts towards small but consistently positive values. Although the change is small, the presence of impurities slightly modifies the neutron energy spectrum. This alters the balance between neutron capture and fission reactions and leads to a different coolant temperature feedback.

The void reactivity coefficient remains positive in both configurations, consistent with the behaviour of sodium-cooled fast reactors. In the present infinite-lattice model, this positive effect arises primarily from spectrum hardening and the reduction of parasitic absorption in sodium, which together enhance the fast fission probability. For the reference case, the void coefficient is positive but relatively stable with burnup. In the impurity-loaded fuel, however, its magnitude increases significantly while maintaining a positive sign. Although the burnup dependence remains smooth, the amplification of the positive void effect indicates an enhanced spectral hardening contribution, which may further challenge inherent safety margins.

Overall, the reference SPX fuel demonstrates physically consistent and safety-aligned feedback behaviour. The impurity-loaded configuration preserves some qualitative trends (e.g. depletion-driven reactivity reduction and positive void response) but introduces a fundamentally altered Doppler feedback, a positive coolant temperature response and a strengthened positive void effect. These findings highlight that the neutronic impact of reprocessing-induced impurities extends beyond reactivity shifts and directly affects intrinsic reactor safety parameters. The reference case therefore provides an essential and physically validated baseline against which the safety implications of impurity introduction must be critically evaluated.

Chapter 5

Conclusions and Outlook

5.1 Conclusion

This work originated from the broader challenge of managing the back end of the nuclear fuel cycle and the need to move toward a closed fuel cycle capable of reducing long-term radiotoxicity and decay heat while promoting resource utilization and waste minimization. Within this context, the CHALMEX process was considered as a promising reprocessing route. Its use of a less hazardous solvent system, its simplified flowsheet compared to conventional PUREX-based technologies, the absence of pure plutonium separation, and its compatibility with a single-stream recycling strategy make it particularly attractive. In addition, its development within Chalmers University provided a unique opportunity to establish a direct bridge between experimental chemistry and reactor-level neutronic assessment.

A central aspect of this study was the realistic inclusion of impurities. Since no reprocessing technology can achieve 100% separation efficiency, the presence of residual fission products and minor actinides must be treated as an inherent feature rather than an exception. This work therefore represents a first step in connecting the CHALMEX chemical separation process to its potential deployment in a fast-spectrum reactor environment through detailed neutronic simulations.

From a purely neutronic and operational perspective, the analysis shows that the fuel containing the CHALMEX-derived impurity vector maintains criticality within the specific SPX-like fast reactor configuration considered. The multiplication factor remains supercritical over the burnup range, and the overall reactivity evolution follows trends consistent with fast-spectrum behaviour. The modelling assumptions, scenario selection, and systematic comparison between reference, TRU-loaded, and impurity-bearing fuels provide a coherent framework for assessing feasibility.

However, one critical result must be clearly stated: the calculated Doppler coefficient of reactivity is positive in the analysed configuration. A positive Doppler coefficient is not acceptable from a safety standpoint, as it implies that an increase in fuel temperature would increase reactivity rather than reduce it. Such behaviour is incompatible with inherent safety principles and would prevent practical deployment in its current form. Although the general neutronic performance is promising, this specific feedback characteristic represents a fundamental limitation that must be understood and corrected before any realistic application.

Due to time constraints, a full investigation of the origin of this positive Doppler coefficient was not completed. A more detailed study would be required to determine whether the result arises from statistical uncertainty, modelling assumptions, isotopic composition, spectrum effects, or methodological implementation in the branch calculations.

Overall, the study demonstrates that the CHALMEX-based fuel concept can achieve neutronic criticality in a fast-spectrum environment; however, its current reactivity feedback behaviour, in particular the positive Doppler coefficient, represents a fundamental safety limitation that must be resolved before any realistic application.

5.2 Limitations

Several limitations affected the scope and robustness of the present study:

1. **Statistical Uncertainty in Reactivity Coefficients**

   The branch calculations used to evaluate reactivity feedback coefficients exhibit non-negligible Monte Carlo statistical uncertainties. Since reactivity feedback coefficients are derived from finite differences between independent k_{eff} values, the associated uncertainty propagates and can significantly affect the calculated slope. Some fluctuations observed in the burnup-dependent feedback curves may therefore be partially dominated by statistical noise rather than purely physical behaviour.

2. **Computational and Time Constraints**

   Branch calculations in Serpent 2 are both computationally expensive and time intensive, especially for fast-spectrum systems with detailed isotopic compositions. Each scenario required approximately 48–63 hours of simulation time on the available computational resources. These time and computational constraints restricted the possibility of increasing particle histories sufficiently to fully suppress statistical noise or to perform repeated high-statistics verification runs.

3. **Methodological Constraints in Fast-Spectrum Branch Modelling**

   Moreover, the implementation of branch calculations in fast-spectrum reactors is less extensively documented in the literature compared to thermal systems. Input selections such as energy treatment, temperature handling, material definitions, and cross-section interpolation require careful validation. In this work, relevant Serpent physics options—including Doppler Broadening Rejection Correction (`set dbrc`) and unresolved resonance probability table sampling (`set ures`)—were activated using recommended default settings. These treatments are essential for accurate resonance and elastic scattering modelling, especially for heavy isotopes such as ^{238}U, ^{239}Pu, and ^{240}Pu present in the SPX reference fuel.

   To ensure consistency across configurations, these settings were not further modified. Given that Doppler feedback in fast-spectrum systems is intrinsically weaker than in thermal reactors, the numerical implementation—including temperature increments and finite-difference formulation—can significantly influence both the magnitude and sign of the computed coefficient. Additional benchmarking and sensitivity studies would therefore strengthen confidence in the feedback results.

4. **Neutronic-Only Analysis**

   The study was limited to neutronic evaluation within a fixed SPX-like geometry. No thermal-hydraulic coupling, structural material feedback, mechanical behaviour, or full-core transient analysis was performed. Therefore, the conclusions apply only to isolated neutronic performance.

5. **Scrubbing and Separation-State Analysis**

   A systematic investigation of different scrubbing efficiencies within the CHALMEX process, although initiated, was not fully completed. Preliminary infinite-lattice depletion studies indicated that variations in scrubbing beyond the baseline configuration did not lead to substantial changes in the evolution of k_∞, particularly for configurations involving an additional scrubbing step. However, these configurations were not examined in detail within the full fast-reactor model considered in this work.

5.3 Future Work

The present study opens several directions for further investigation:

- **High-Statistics Branch Calculations**

  Reactivity coefficients should be recomputed with significantly increased neutron histories to reduce statistical uncertainty and confirm the sign and magnitude of the Doppler coefficient.

- **Systematic Study of Reactivity Feedback Behaviour**

  A dedicated analysis should investigate the physical origin of the altered feedback coefficients observed in the impurity-loaded configuration. This should include spectrum analysis, isotopic sensitivity studies, and decomposition of Doppler, coolant temperature, and void contributions, together with comparison against reference fast-reactor benchmarks.

- **Extended Scrubbing Scenario Analysis**

  A detailed parametric study of different impurity vectors resulting from varying CHALMEX scrubbing efficiencies should be performed. This would clarify the trade-off between separation performance and reactor behaviour.

- **Coupled Neutronic–Thermal Hydraulic Modelling**

  Incorporating thermal-hydraulic feedback and structural material effects would provide a more realistic safety assessment and allow evaluation of full-core feedback mechanisms.

- **Full-Core and Transient Analysis**

  Extending the study from an inner-zone configuration to a full-core model would allow more accurate evaluation of global reactivity effects.

- **Process-Level Improvements**

  From a chemical-engineering perspective, further development of the CHALMEX solvent system toward improved environmental compatibility ("greener" solvent design) remains an open research area. While CHALMEX avoids pure plutonium separation and reduces process complexity, the solvent system still requires evaluation in terms of toxicity, degradation products, lifecycle impact, and scalability.

Bibliography

[1] John F. Kennedy. Inaugural address. Speech delivered in Washington, D.C., 20 January 1961, 1961.

[2] Alan D. Pasternak. Global energy futures and human development: A framework for analysis. Technical Report UCRL-ID-140773, Lawrence Livermore National Laboratory, Livermore, CA, USA, 2000. URL https://www.geni.org/globalenergy/issues/global/qualityoflife/HDI-and-electricity-consumption.pdf.

[3] José Goldemberg. Energy needs in developing countries and sustainability. *Science*, 269 (5227):1058–1059, 1995. doi: 10.1126/science.269.5227.1058.

[4] Charles de Saillan. Disposal of spent nuclear fuel in the united states and europe: A persistent environmental problem. *Harvard Environmental Law Review*, 34(2):461–519, 2010. URL https://journals.law.harvard.edu/elr/wp-content/uploads/sites/79/2019/07/34.2-de-Saillan.pdf.

[5] U.S. Department of Energy. The history of nuclear energy. Technical report, Office of Nuclear Energy, Science and Technology, 2000. URL https://www.energy.gov/ne/articles/history-nuclear-energy.

[6] International Atomic Energy Agency. 50 years of nuclear energy. IAEA General Conference document GC(48)/INF/4, 2004. URL https://www.iaea.org/sites/default/files/gc/gc48inf-4-att3_en.pdf.

[7] Patrick Moore. Going nuclear: A green makes the case. *The Washington Post*, April 2006. URL https://www.washingtonpost.com/wp-dyn/content/article/2006/04/14/AR2006041401209.html. Outlook section, p. B01.

[8] Frank B. Friedman. Environmental problems relating to uranium mining and milling. *Natural Resources Lawyer*, 11(2):277–303, 1978. URL https://www.jstor.org/stable/40912262.

[9] M. V. Ramana. Technical and social problems of nuclear waste. *Wiley Interdisciplinary Reviews: Energy and Environment*, 7(3):e289, 2018. doi: 10.1002/wene.289. URL https://doi.org/10.1002/wene.289. Received: 1 October 2017; Revised: 6 January 2018; Accepted: 8 January 2018.

[10] Robin Taylor, William Bodel, Laurence Stamford, and Gregg Butler. A review of environmental and economic implications of closing the nuclear fuel cycle—part one: Wastes and environmental impacts. *Energies*, 15(4):1433, 2022. doi: 10.3390/en15041433.

[11] Christophe Poinssot et al. Advanced nuclear fuel cycles—main challenges and strategic choices. *Energies*, 15(4):1433, 2022. doi: 10.3390/en15041433.

[12] Alistair F Holdsworth, Harry Eccles, Clint A Sharrad, and Kathryn George. Spent nuclear fuel—waste or resource? the potential of strategic materials recovery during recycle for

sustainability and advanced waste management. *Waste*, 1(1):249–263, 2023. doi: 10.3390/waste1010016.

[13] Robin Taylor, William Bodel, and Gregg Butler. A review of environmental and economic implications of closing the nuclear fuel cycle—part two: Economic impacts. *Energies*, 15(7): 2472, 2022. doi: 10.3390/en15072472.

[14] Robin J. Taylor, editor. *Reprocessing and Recycling of Spent Nuclear Fuel*. Woodhead Publishing, Cambridge, 2015. ISBN 978-1-78242-212-9.

[15] Katarzyna Kiegiel, Tomasz Smoliński, and Irena Herdzik-Koniecko. Advanced nuclear reactors—challenges related to the reprocessing of spent nuclear fuel. *Energies*, 18(15):4080, 2025. doi: 10.3390/en18154080.

[16] M. Bäckman, Emma Aneheim, Christian Ekberg, Elin Löfström-Engdahl, Teodora Retegan, Gunnar Skarnemark, Janne Wallenius, Mats Jonsson, and Peter Wikberg. Partitioning and transmutation: Current developments – 2013. a report from the swedish reference group for p&t research. Technical Report TR-13-29, Svensk Kärnbränslehantering AB (SKB), Stockholm, Sweden, 2013. URL https://skb.se/publikation/2489506/TR-13-29.pdf.

[17] OECD Nuclear Energy Agency. *Homogeneous versus Heterogeneous Recycling of Transuranics in Fast Nuclear Reactors*. Nuclear Science. OECD Publishing, Paris, 2012. doi: 10.1787/9789264991774-en. URL https://doi.org/10.1787/9789264991774-en.

[18] Giuseppe Modolo, Andreas Wilden, Andreas Geist, Daniel Magnusson, and Rikard Malmbeck. A review of the demonstration of innovative solvent extraction processes for the recovery of trivalent minor actinides from purex raffinate. *Radiochimica Acta*, 100(8–9):715–725, 2012. doi: 10.1524/ract.2012.1962. URL https://www.degruyter.com/document/doi/10.1524/ract.2012.1962/html.

[19] Robin J. Taylor, Gemma Mathers, and Anthony Banford. The development of future options for aqueous recycling of spent nuclear fuels. *Progress in Nuclear Energy*, 164:104837, 2023. doi: 10.1016/j.pnucene.2023.104837.

[20] OECD Nuclear Energy Agency (NEA). State-of-the-art report on innovative fuels for advanced nuclear systems, 2014. URL https://www.oecd-nea.org/upload/docs/application/pdf/2019-12/6895-report-innovative-fuels.pdf.

[21] Nuclear Energy Agency (NEA). Unlocking the hidden value of nuclear fuel: The societal benefits of diverse material recycling, 2025. URL https://www.oecd-nea.org/upload/docs/application/pdf/2025-01/7674_-_unlocking_hidden_value_of_nuclear_fuel.pdf.

[22] Jaakko Leppänen. Serpent – a continuous-energy monte carlo reactor physics burnup calculation code. Technical report, VTT Technical Research Centre of Finland, Espoo, Finland, June 2015.

[23] J. E. Birkett, M. J. Carrott, O. D. Fox, A. D. Halls, M. F. Ruiz-Lopez, C. Madic, and R. J. Taylor. Recent developments in the purex process for nuclear fuel reprocessing: Complexant based stripping for uranium/plutonium separation. *Chimia*, 59(12):898–904, 2005. doi: 10.2533/000942905777675327.

[24] G. Modolo, A. Wilden, A. Geist, D. Magnusson, and R. Malmbeck. A review of the demonstration of innovative solvent extraction processes for the recovery of trivalent minor actinides from purex raffinate. *Radiochimica Acta*, 100(8-9):715–725, 2012. doi: 10.1524/ract.2012.1962.

[25] Rikard Malmbeck, Daniel Magnusson, Stéphane Bourg, Michael Carrott, Andreas Geist, Xavier Hérès, Manuel Miguirditchian, Giuseppe Modolo, Udo Müllich, Christian Sorel, Robin

Taylor, and Andreas Wilden. Homogenous recycling of transuranium elements from irradiated fast reactor fuel by the euro-ganex solvent extraction process. *Radiochimica Acta*, 108(7): 525–541, 2020. doi: 10.1515/ract-2020-0035.

[26] Thea Lyseid Authen, Andreas Wilden, Dimitri Schneider, Fabian Kreft, Giuseppe Modolo, Mark R. StJ. Foreman, and Christian Ekberg. Batch flowsheet test for a ganex-type process: the chalmex fs-13 process. *Solvent Extraction and Ion Exchange*, 41(2):190–199, 2023. doi: 10.1080/07366299.2023.2174308.

[27] Christian Ekberg, Andreas Wilden, Giuseppe Modolo, and Mark R. StJ. Foreman. Advances in ganex process development for transuranic recycling. *Journal of Radioanalytical and Nuclear Chemistry*, 329:1507–1520, 2021. doi: 10.1007/s10967-021-07803-9.

[28] Giuseppe Modolo, Andreas Geist, and Mickael Miguirditchian. Development of the ganex process for actinide recycling. *Chemical Reviews*, 114(2):588–618, 2014. doi: 10.1021/cr400022y.

[29] D. D. Sood and S. K. Patil. The role of sol–gel process in the fabrication of nuclear fuels: An overview. *Journal of Sol-Gel Science and Technology*, 59:404–416, 2011. doi: 10.1007/s10971-010-2273-y.

[30] Marcus Hedberg. *Nitride Fuel Production by the Internal Sol–Gel Process*. Licentiate thesis, Chalmers University of Technology, Gothenburg, Sweden, 2014.

[31] Joël Guidez and Gérard Prêle. *Superphénix: Technical and Scientific Achievements*. CEA and EDF, Gif-sur-Yvette, France, 2017. Translation by Bernard Vray (BVFC).

[32] Alexander Ponomarev Stepnykh et al. Spx benchmark part i: Results of static neutronics. *Journal of Nuclear Engineering and Radiation Science*, 6(3):031405, 2020. doi: 10.1115/1.4046744.

[33] O. Litaize, A. Ponomarev, M. Tiphine, et al. A static neutronic benchmark for the superphénix fast reactor core. *Energies*, 13(21):5598, 2020. doi: 10.3390/en13215598.

[34] VTT Technical Research Centre of Finland. Tutorial — serpent wiki. https://serpent.vtt.fi/mediawiki/index.php/Tutorial, 2024. Accessed: 2026-02-09.

[35] R. Henry. Neutronics modelling of superphénix benchmark with serpent and parcs. In *Proceedings of the International Conference NENE 2018*, 2018.

[36] A. Ponomarev. Application of serpent 2 for sodium fast reactor neutronics and safety analysis. In *8th Serpent User Group Meeting*, Espoo, Finland, 2018.

[37] J.J. Duderstadt and L.J. Hamilton. *Nuclear Reactor Analysis*. John Wiley & Sons, 1976.

[38] L. Thilagam, K. A. Venkatesan, T. G. Srinivasan, and P. R. Vasudeva Rao. Solvent extraction processes in nuclear fuel reprocessing. *Energy Procedia*, 7:606–611, 2007. doi: 10.1016/j.proche.2013.03.078.

[39] Luca Fiorito, Matteo Zanetti, Federico Grimaldi, and Gert van den Eynde. Uncertainty quantification for the doppler reactivity feedback coefficient of myrrha. *Nuclear Science and Engineering*, 196:1–17, 2024. doi: 10.1080/00295639.2024.2353987.

[40] J. Leppänen, M. Pusa, T. Viitanen, V. Valtavirta, and T. Kaltiaisenaho. The serpent monte carlo code: Status, development and applications in 2013. *Annals of Nuclear Energy*, 82: 142–150, 2015.

[41] F. P. C. Lima, S. de O. Vellozo, and M. J. Velozo. Accurate reactivity void coefficient

calculation for the fast spectrum reactor FBR-IME. In *Proceedings of the International Nuclear Atlantic Conference (INAC 2017)*, Belo Horizonte, MG, Brazil, 2017.

[42] N. Soppera, M. Bossant, and E. Dupont. Janis 4: An improved version of the nea java-based nuclear data information system. *Nuclear Data Sheets*, 120:294–296, 2014. doi: 10.1016/j.nds.2014.07.071.

[43] P. Wydler and Y. Kadi. A physical assessment of the effectiveness of different actinide transmutation systems. In *Proceedings of the 3rd OECD/NEA Information Exchange Meeting on Actinide and Fission Product Partitioning and Transmutation*, pages 298–312, Cadarache, France, 1995. OECD Nuclear Energy Agency. Includes fission-to-capture ratios for minor actinides in various neutron spectra.

[44] Bin Liu, Jinsheng Han, Fang Liu, Jie Sheng, and Zhihao Li. Minor actinide transmutation in the lead-cooled fast reactor. *Progress in Nuclear Energy*, 119:103148, 2020. doi: 10.1016/j.pnucene.2019.103148. Shows how loaded minor actinides are partly fissioned or transmuted into new fissile nuclides in a fast spectrum.

[45] Liaoyuan He, Liang Chen, Shaopeng Xia, and Yang Zou. Minor actinides transmutation and ^{233}u breeding in a closed th–u cycle based on molten chloride salt fast reactor. *Energies*, 15 (24):9472, 2022. doi: 10.3390/en15249472. Discusses initial reactivity penalty of MAs and their progressive transmutation/fission in a fast spectrum.

[46] Andrea Alfonsi and Gilles Youinou. Impact of fission products impurity on the plutonium content in pwr mox fuels. Technical Report INL/EXT-12-26114, Idaho National Laboratory, 2012.

[47] G. D. Del Cul, L. D. Trowbridge, J. P. Renier, R. J. Ellis, K. A. Williams, B. B. Spencer, and E. D. Collins. Analysis of the reuse of uranium recovered from the reprocessing of commercial lwr spent fuel. Technical Report ORNL/TM-2007/207, Oak Ridge National Laboratory, 2009.

[48] OECD Nuclear Energy Agency. State-of-the-art report on innovative fuels for advanced nuclear systems. Technical Report NEA No. 6895, OECD NEA, 2014.

[49] Elmer E. Lewis. *Fundamentals of Nuclear Reactor Physics*. Academic Press, 2008.

[50] Henryk Anglart. Introduction to nuclear reactor technology. Technical report, KTH Royal Institute of Technology, 2011. Includes spent-fuel composition showing that ^{238}U remains the dominant uranium isotope after burnup.

[51] Wikipedia contributors. Fission product. https://en.wikipedia.org/wiki/Fission_product, 2025. Accessed: 2025-11-26.

[52] N. Lucas. *Development of bismuth thin film and bulk electrodes for electrochemical extraction and online monitoring of lanthanides in molten salts*. PhD thesis, University of Manchester, 2022.

[53] L. Martin et al. Selective separation of trivalent actinides from lanthanides by aqueous processing. Technical report, US Department of Energy, 2011.